REMTECH

BOUNDARY LAYER SIMULATOR
IMPROVEMENT

Final Report

March 1989

Prepared by:

Sarat C. Praharaj
Craig Schmitz
Joseph L. Nouri

REMTECH, Inc.
Huntsville, AL 35805

Contract:

NAS8-36551

For:

National Aeronautics and Space Administration
George C. Marshall Space Flight Center
Marshall Space Flight Center, AL 35812

REMTECH

FOREWORD

This final report presents work conducted for the Marshall Space Flight Center (MSFC), National Aeronautics and Space Administration in response to the requirements of Contract NAS8-36551. The work presented here was performed by REMTECH, Inc., Huntsville, AL, and is titled "Boundary Layer Simulator Improvement."

The project manager for this project was Dr. Sarat C. Praharaj. The project was very much aided by the helpful technical support of the NASA contract monitor, Mr. Klaus Gross, and by Mr. Alfred Krebsbach, both of the Performance Analysis Branch of the Propulsion Systems Division.

Contents

REMTECH

List of Figures

List of Tables

REMTECH

Section 1

INTRODUCTION

BLIMPJ [1] has been identified by the propulsion community as the rigorous boundary layer program in connection with the existing JANNAF reference programs such as ODE, ODK and TDK-BLM, all in Ref. [2]. The improvements made to BLIMPJ and described in this report have potential applications in the design of the future Orbit Transfer Vehicle (OTV) engines. These engines will utilize a high chamber pressure expander cycle operation mode which primarily depends on the heat energy transmitted from the combustion products through the thrust chamber wall. The larger the regenerative heat transfer, the higher the chamber pressure, which, in turn, permits larger area ratio nozzles and thus, better performance. The heat transfer to the nozzle wall is affected by such variables as wall roughness, relaminarization and the presence of particles in the boundary layer flow. The motor performance loss calculation for these nozzles with thick boundary layers is inaccurate using the conventional JANNAF procedure. Thus, engineering procedures are required to model these effects adequately.

The first phase of this work was completed in December 1984 [3], after which a presentation summarizing the results was made at the JANNAF combustion meeting in 1985 [4]. Simplified analytical formulations were identified in Ref. [3] to include the effects of wall surface roughness, relaminarization, condensed phase and thick boundary layer in the current JANNAF thrust chamber boundary layer skin friction and heat transfer calculation procedure. These effects will exist in the operation of the projected high area ratio OTV engines. During Phase I, it was recommended that the turbulence models existing in BLIMPJ be updated in order to account for wall roughness and relaminarization, whereas engineering approximations were given to include condensed phase effects in the boundary layer. While conducting these studies, several assumptions were made with regard to wall boundary conditions and their effects on the turbulence models. In addition, a semi-automatic procedure was devised for calculating the thrust decrement in thick boundary layers having normal pressure gradients and transverse curvature effects. The objectives of this work concentrated on extending the applications of the previous modules, and relaxing the analytical limitations to permit more realistic wall and flow conditions. Some of these required modifications of the turbulence models have already been coded in BLIMPJ [3]. An additional objective of this effort was to conduct experimental feasibility studies to find out how to

obtain quality test data with advanced instrumentation for concept verification purposes.

This report is divided into seven distinct sections. Following the introductory section, Section 2 validates the turbulence model to include the effects of wall roughness and devises a way of treating multiple smooth-rough surfaces. Section 3 deals with prediction of relaminarization regions and combined effects of wall cooling and surface roughness on relaminarization. A turbulence model to represent the effects of constant condensed phase loading is given in Section 4. Section 5 describes a procedure for thrust decrement calculation in thick boundary layers by coupling TDK and BLIMPJ and provides a way for thrust loss optimization. Sections 6 and 7 identify potential experimental studies in rocket nozzles and the required instrumentation to provide accurate measurements in support of the presented new analytical models. The modifications made to the turbulence models and additions of engineering models in BLIMPJ are summarized in the Appendix.

Section 2

WALL ROUGHNESS

2.1 Background

The importance of wall surface roughness in increasing the resistance to fluid flows has been recognized for years. One of the principal parameters influencing the skin friction and the surface heat transfer to a rough wall is the roughness height, k. The early correlations which used this parameter to modify the turbulence model due to the presence of roughness or those which used this parameter in the engineering approaches missed the effects of roughness shape, pattern and density. However, one of the recent correlations which modeled the surface roughness by accounting for the roughness shapes was developed by Dirling [5], who applied it to the prediction of nosetip shape changes. In modeling the effects of roughness on skin friction, the boundary layer velocity profile was correlated with surface roughness of sand. Empirical correlations have been developed for other types of roughness elements to obtain the equivalent sand roughness. Dirling's concept is based on locally similar boundary layer consideration.

In the previous work of Praharaj et al. [3], simplified correlations appropriate for rocket nozzle applications were coded in the BLIMPJ computer code. A total of three roughness options, including two engineering options and one exact option, were coded. The first two options perform "point" calculations, whereas the third option simulates the effects of a rough wall on the boundary layer and accounts for "history" effects in the boundary layer. The concept of equivalent sand roughness was used in all the above options. Since a very small data base exists for rocket nozzle applications, some of these options were checked for external flow situations. All three options were utilized for the projected generic OTV nozzle to check their consistency.

2.2 Roughness Turbulence Model Validation

A literature survey was conducted to validate the roughness formulation. One of the few references on nozzle test data including surface roughness was due to Reshotko et al. [6] conducted at NASA LeRC with hot air ($T_o = 970°R$) in a 60° - 15° half-angle conical nozzle (Fig. 2.1). In contrast, much more data on roughness

effects are available for pipe flow in the literature. The LeRC test considered a matrix of test conditions involving various chamber pressures varying from 30 to 300 psia, yielding an order of magnitude range in Reynolds Number and three levels of RMS roughness heights: R_K=120 μ, 175 μ, and 325 μ (all in inches).

TDK was first run using the geometry and test conditions given in Fig. 2.2 to compute the distribution of wall pressure to compare with measured pressures. The comparison given in Fig. 2.3 shows excellent agreement throughout the nozzle except at the throat/15 deg divergence cone juncture, where the pressure slope is noticeably discontinuous. Also note that the second derivative of the wall geometry is discontinuous here. BLIMPJ was then run for $P_c = 300$ psia using the above wall pressures and measured wall temperatures. It was immediately discovered that the value of Re_θ was much higher than those in the relaminarization regime. Thus, it was not necessary to turn on the relaminarization flag. A significant problem arose in the accuracy of computed heat transfer with the use of wall temperatures higher than approximately $T_w = 660°R$. These inaccuracies are attributed to the deficiencies in the numerics employed in BLIMPJ. However, as $\Delta T \, (= T_o - T_W)$ becomes high, as is the case with most rocket engines, these inaccuracies vanish. Thus, in the current application, whenever T_W was higher than 660°R, it was equated to 660°R. This modification has been found not to significantly affect the computed values of heat transfer coefficient (h) for air so long as the wall temperatures are not too far different from the measured values. h was computed in accordance with the procedure adopted in Ref. [6] as follows:

$$h = \frac{\dot{q}}{H_{aW} - H_W} \tag{2.1}$$

where $H_{aW} = H_e + Pr^{1/3}(H_o - H_e)$ for turbulent flow

with $Pr = 0.71$

The roughness turbulence option was exercised for both smooth and all rough wall situations, from which the smooth wall and $R_K = 120 \mu$, 170 μ and 325 μ wall data are plotted in Figs. 2.4 through 2.7, respectively. It is seen from Fig. 2.4 that the data are turbulent over the whole nozzle. The rough wall computations yielded higher heating than the smooth wall over most of the nozzle, as seen in Figs. 2.5 through 2.7. The comparison with BLIMPJ is only reasonable around the nozzle throat. It is our current opinion that these discrepancies may be partially attributed to the heat-transfer measurement accuracy (within 10 percent) and the accuracy (± 10 percent) of the roughness height measurements. Also, it is not clear from the data in Ref.[6] whether or not the authors quote the "equivalent

4

sand roughness" values for R_K. Depending on the size, shape and density of the roughness elements, the R_K values have been shown in Ref.[3] to vary a great deal.

2.3 Treatment of Multiple Sections with Smooth/ Rough Wall Surfaces

Variable roughness on the nozzle wall could be a result of differential heating load on various sections of the wall or due to the use of ablating surfaces in sections of the nozzle wall. It could also occur if the particles in the flow deposit on the nozzle wall. The three options coded in BLIMPJ to calculate the effects of roughness will behave differently if the roughness parameter is turned on or off. The two engineering options which perform "point" calculations will show discontinuity in skin friction and wall heating calculations at the point where either roughness of the wall is introduced into the calculations or roughness of the wall becomes negligible. In contrast, the method of Cebeci and Chang [7] used in the third option modifies the length scale in the inner region of the boundary layer due to the presence of roughness and is believed to smooth the effects of transitions between rough and smooth sections.

Modifications to the BLIMPJ computer code were made adding a variable surface roughness option. This new option permits the user to input a table of equivalent sand roughness heights versus normalized nozzle axial coordinates. This table is input as part of the namelist inputs and consists of an option flag and two arrays dimensioned to 20. With this option, a roughness profile can be defined over the complete length of a nozzle.

The OTV nozzle check case was used to examine the results obtained when the variable roughness option is used with the Cebeci-Smith roughness option in BLIMPJ. Figure 2.8 shows the heat flux distribution in the OTV nozzle with two regions of roughness. Figure 2.9 shows an expanded view of the first region of roughness and Fig. 2.10 shows an expanded view of the second region of roughness. It can be observed from Fig. 2.9 that the "history" effects of introducing wall roughness at a certain location persist downstream of the roughness and blend into the smooth wall value after a certain distance. This sample case with two regions of roughness required four values of equivalent sand roughness to define the roughness profile in the nozzle. With 20 values available, a wide variety of roughness profiles can be defined. Figures 2.11 and 2.12 show the heat flux distribution in the throat region where variable roughness was introduced. From these figures it can be seen that the heat flux does not maintain the slope of the heat flux distribution as it does in the other regions of the nozzle. The cause of this is not clear, except that it falls in a region of increasing heating rate to the left of the throat and decreasing

REMTECH

heating rates to the right of the throat.

In order to check the previously coded roughness options with measured data in internal flow situations, a reasonable literature survey was performed and the relevant data collected. As far as checking the effects of partially rough and partially smooth surfaces on heat transfer and skin friction, some data were discovered in Ref. [8]. The test was on a 40k subscale regeneratively cooled thrust chamber (Fig. 2.13) at MSFC to conduct cycle life tests. During the test it was discovered that the test section was becoming rough and the heat load was going up during testing. Polishing the test section at the end of a run helped bring down the heat load. Measured heat load data are given in Fig. 2.17 where the effects of polishing the surface are clear. The wall pressure distribution (Fig. 2.14) was obtained by running the available version of TDK, where a small discontinuity in pressure is observed at the nozzle throat. Comparisons of the data are made in Figs. 2.15 and 2.16 with BLIMPJ output using roughness values of $R_K = 45$ μin. in the combustion chamber and the throat region, and $R_K = 20$ μin. in the divergent part of the nozzle. The analytical model gave a delta percent heat load between the smooth and variably rough wall runs, which was plotted in Fig. 2.17. The validation of the analytical model is quite good.

6.5"

24.2"

37.6"

60°

15°

4.8"

└─ VELOCITY
B.L. START

┌─ THERMAL
B.L. START

COOLED INLET

17"

└─ VELOCITY
B.L. START

└─ THERMAL B.L.
START

ADIABATIC INLET
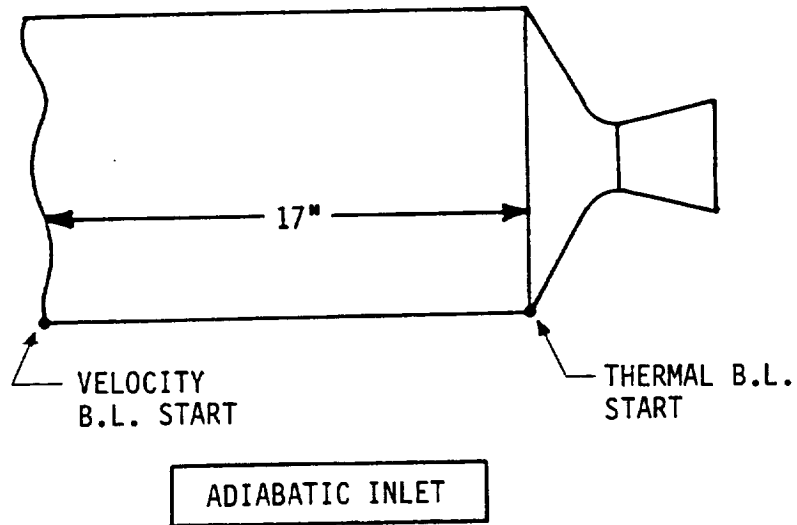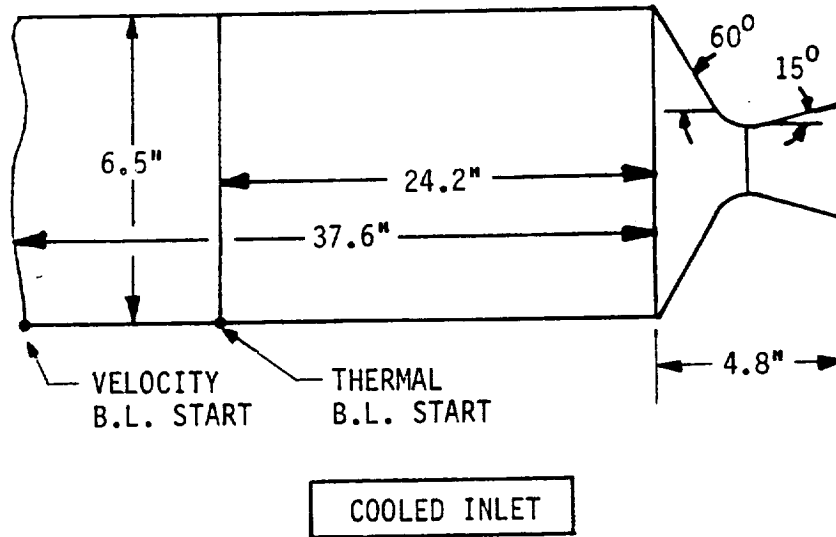
Figure 2.1: 60° - 15° Half-Angle Nozzle Tested at NASA LeRC (Inlets Not Drawn to Scale)

REMTECH
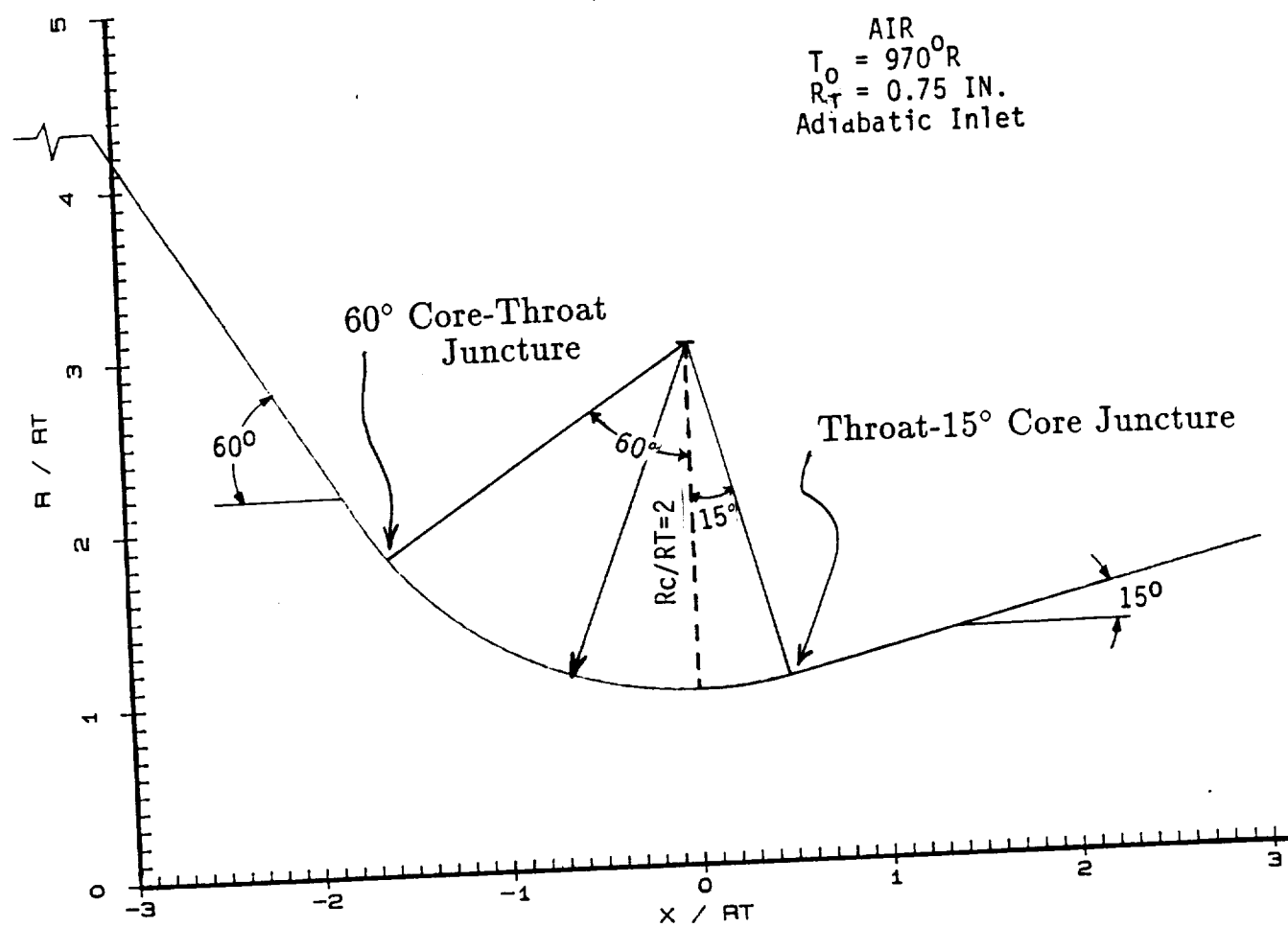
Figure 2.2: Geometry and Test Conditions

REMTECH
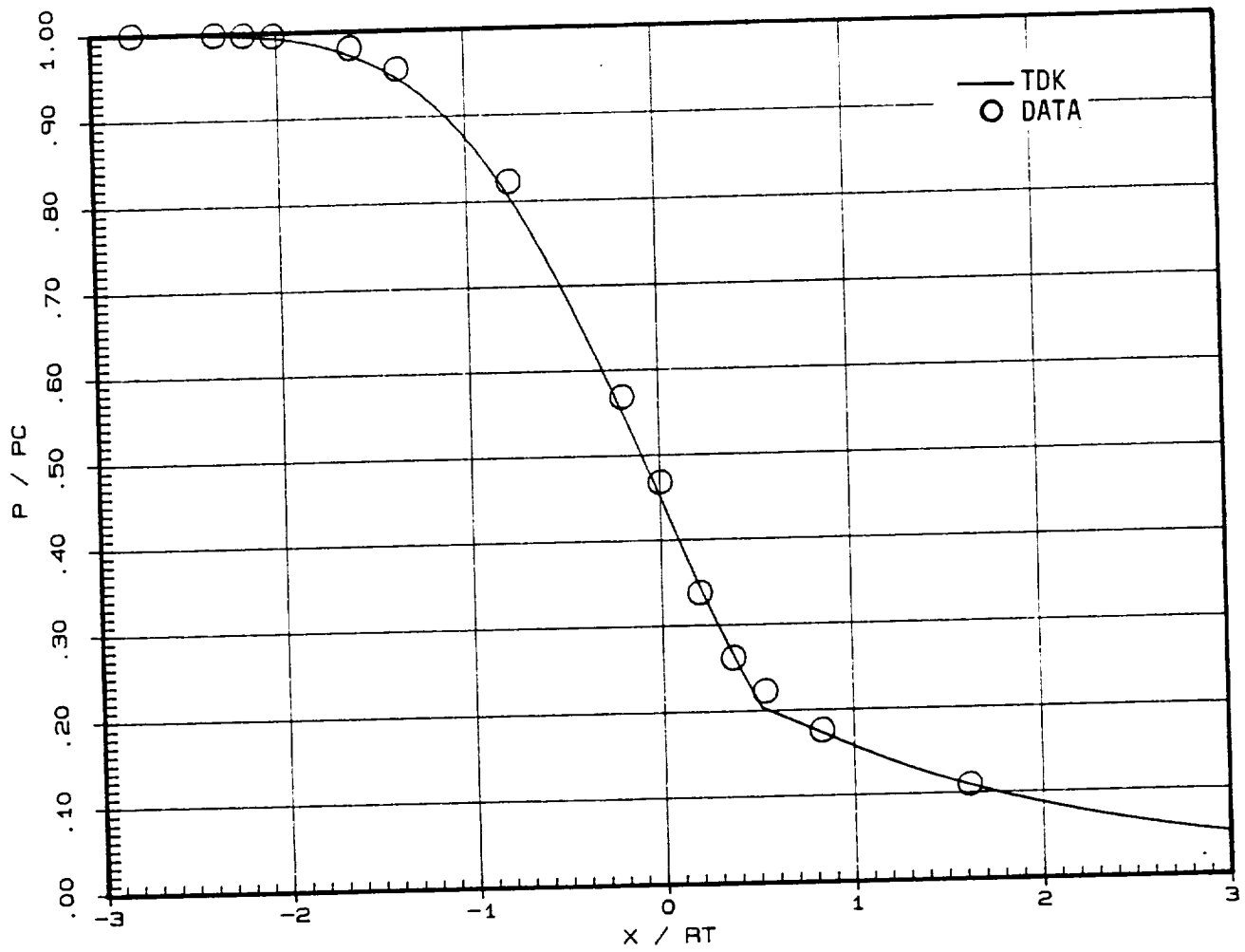
Figure 2.3: Wall Pressure Comparison

60 DEG. NOZZLE, P_c = 300 PSIA
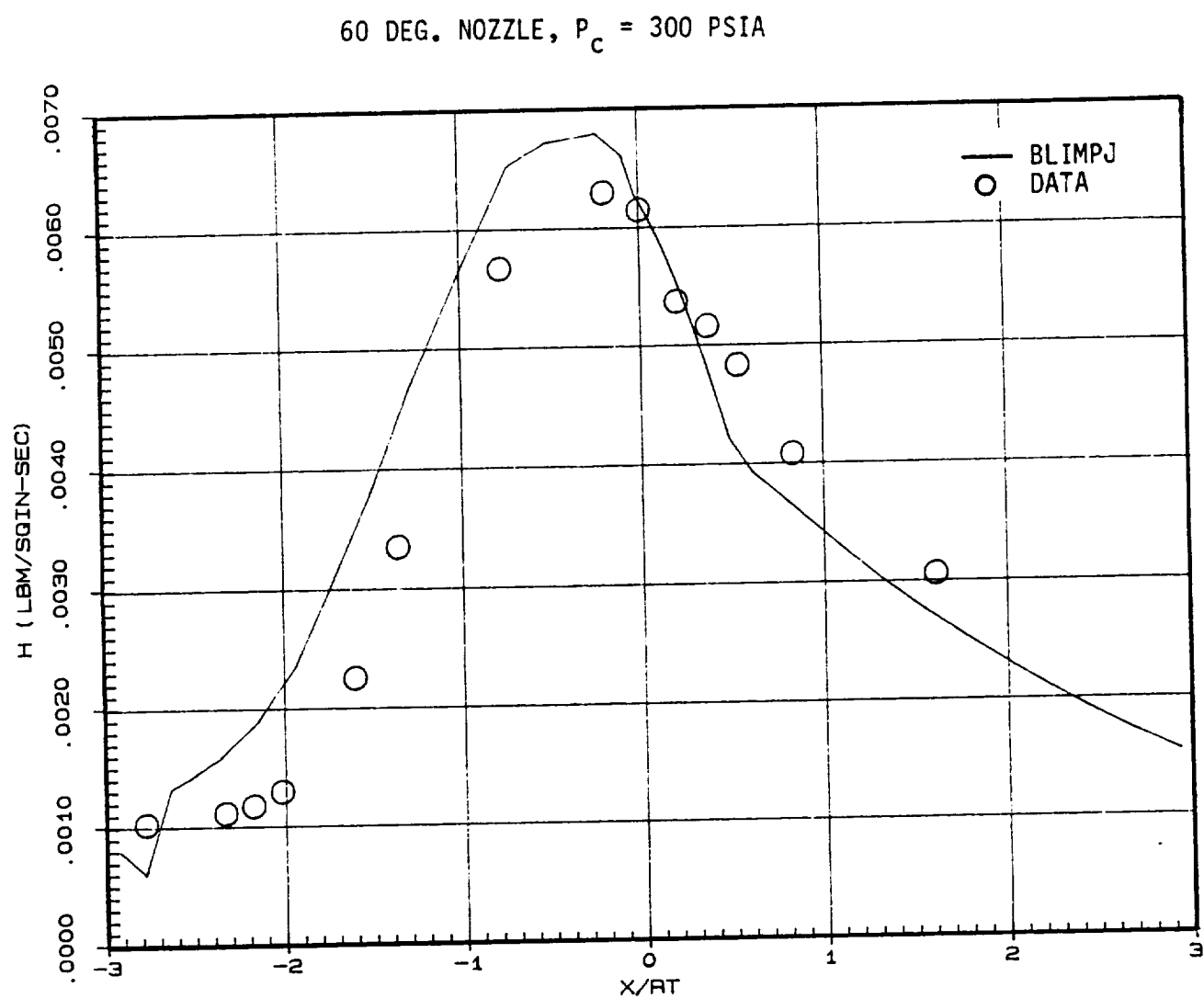
Figure 2.4: Film Coefficient vs. Normalized Axial Distance – Smooth Wall
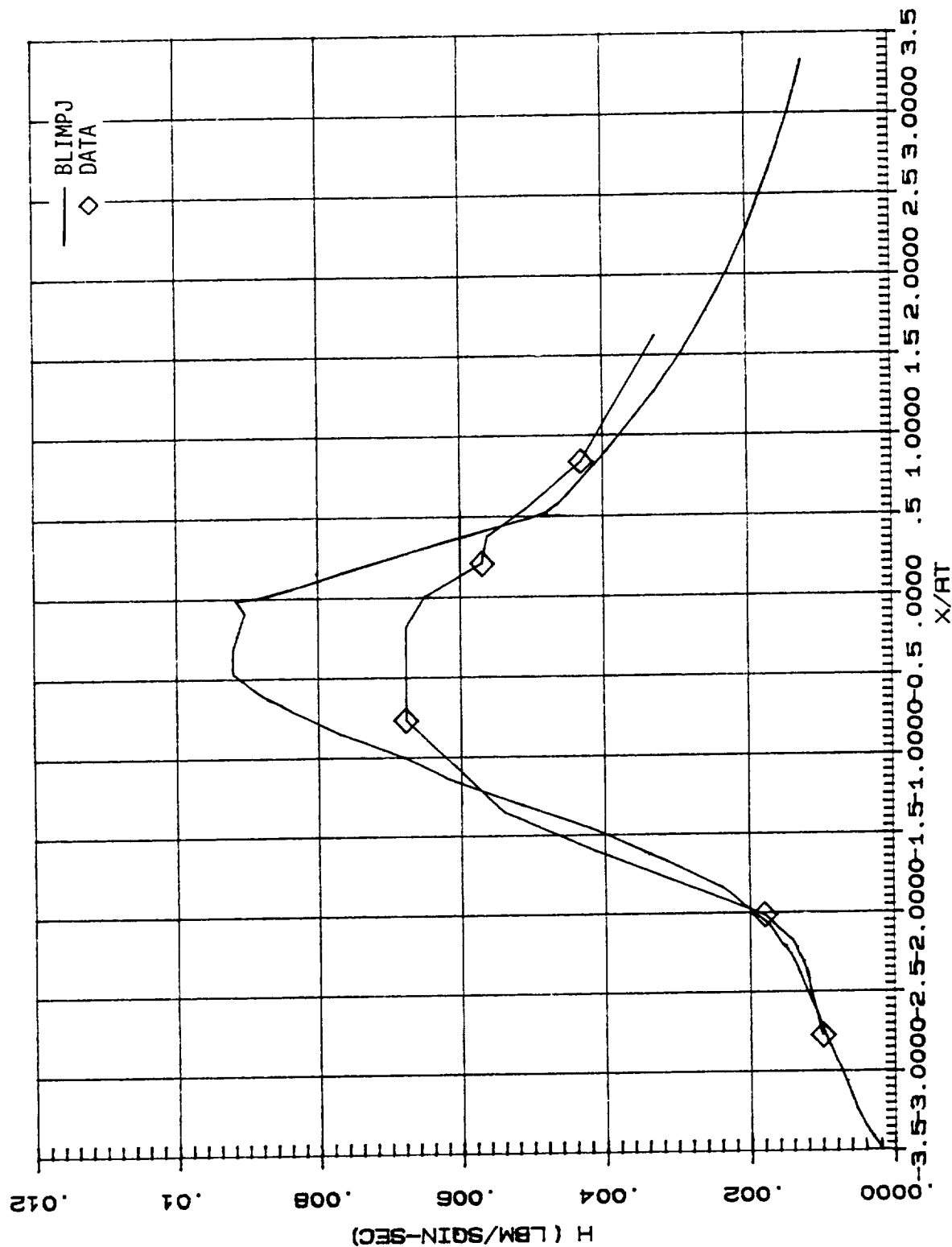
Figure 2.5: Film Coefficient vs. Normalized Axial Distance - Rough Wall (RK = 120 μ In.)
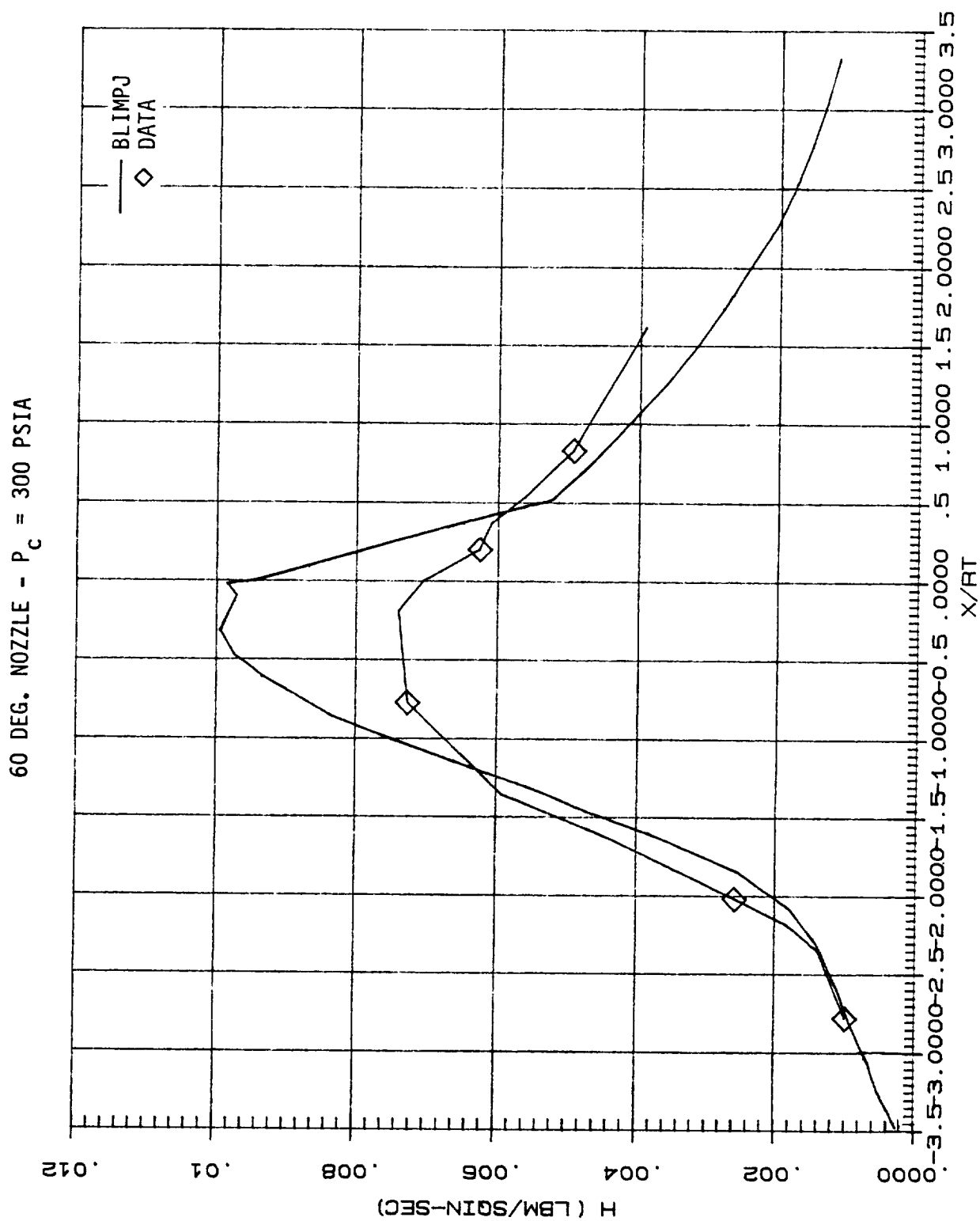
Figure 2.6: Film Coefficient vs. Normalized Axial Distance - Rough Wall (RK = 170 μ in.)

60 DEG. NOZZLE, P_c = 300 PSIA
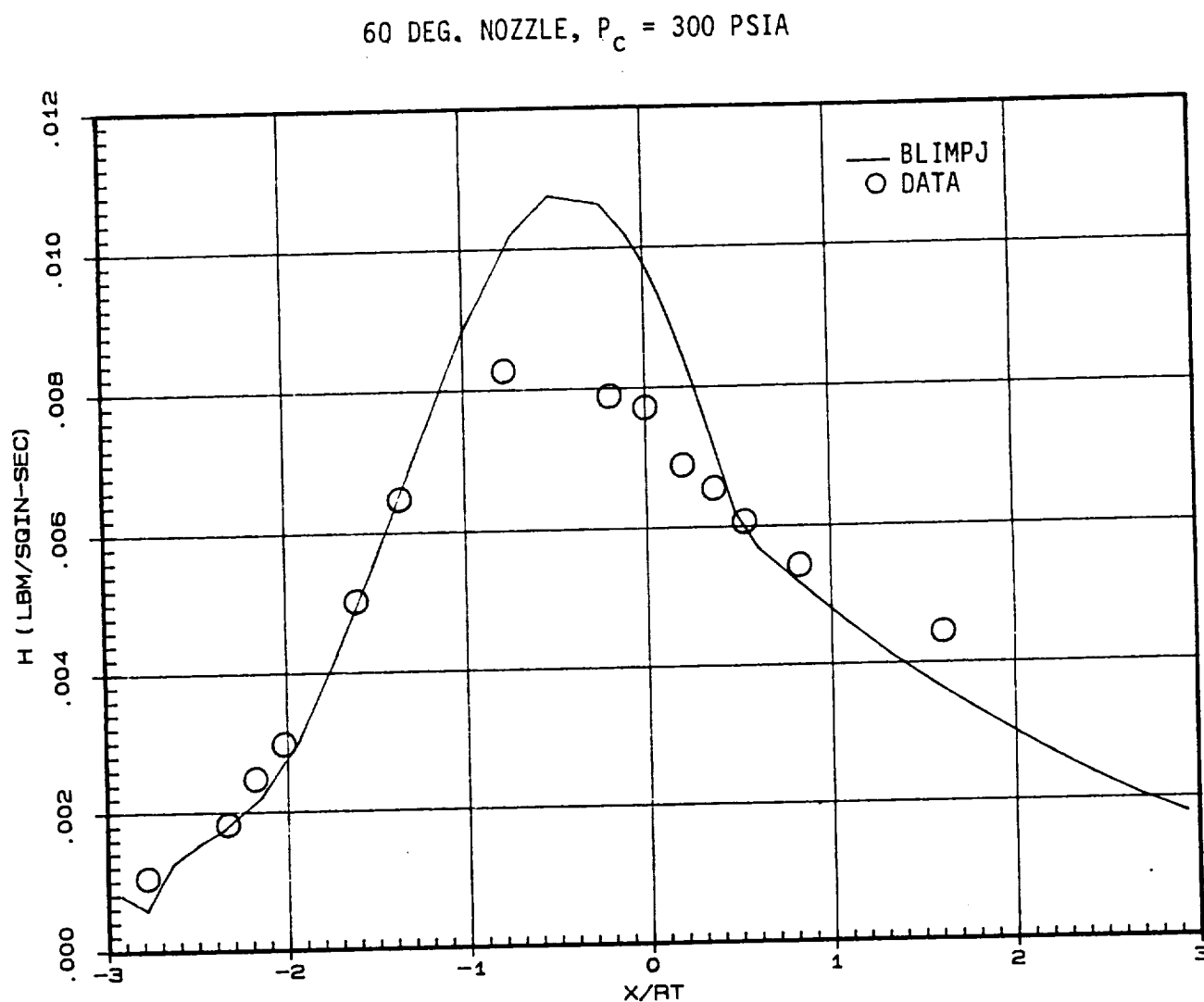
Figure 2.7: Film Coefficient vs. Normalized Axial Distance – Rough Wall (RK = 325 μ in)

REMTECH
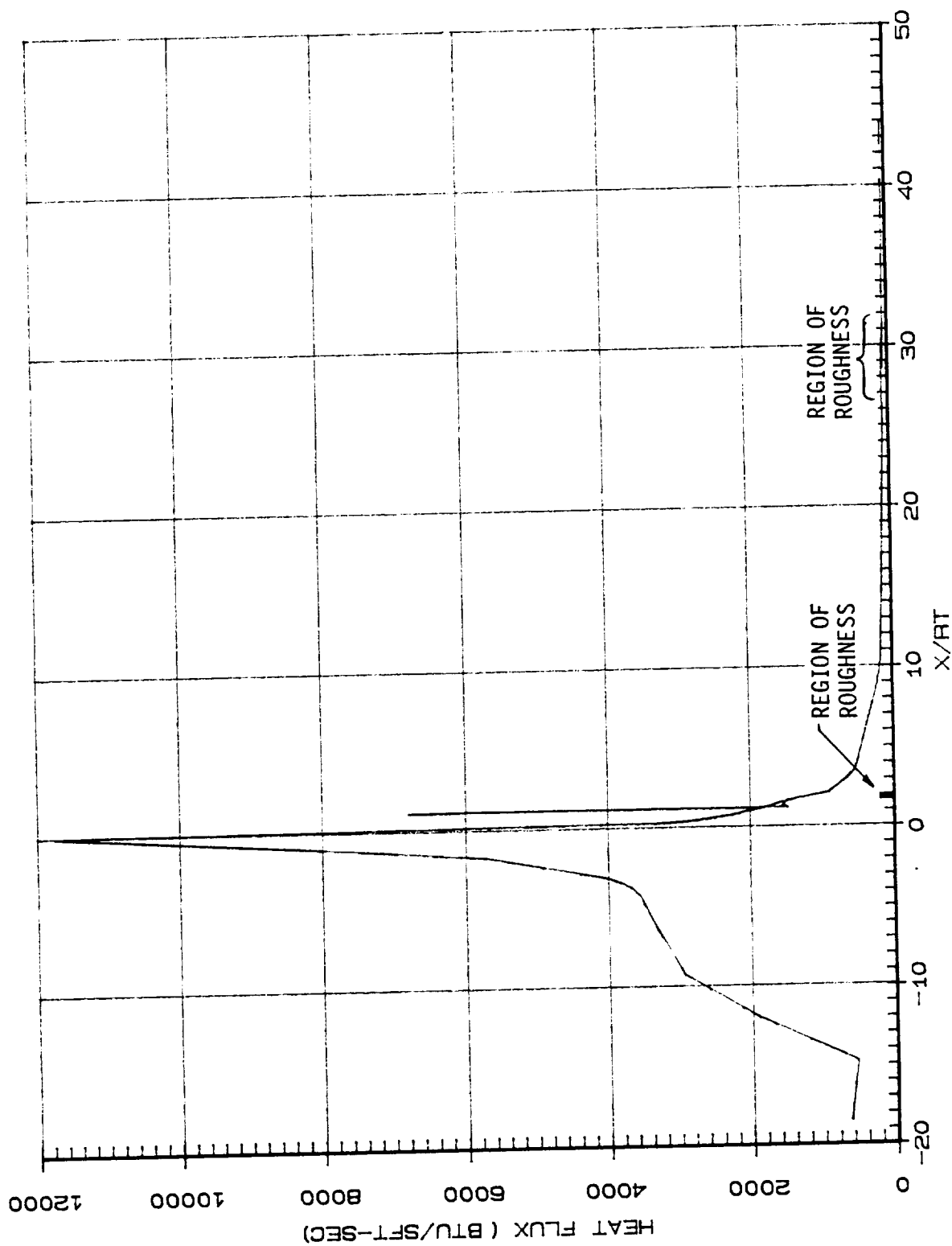
Figure 2.8: Heat Flux Distribution in the OTV Nozzle with Two Regions of Roughness (RK = 0.00125 Ft.)

14

REMTECH
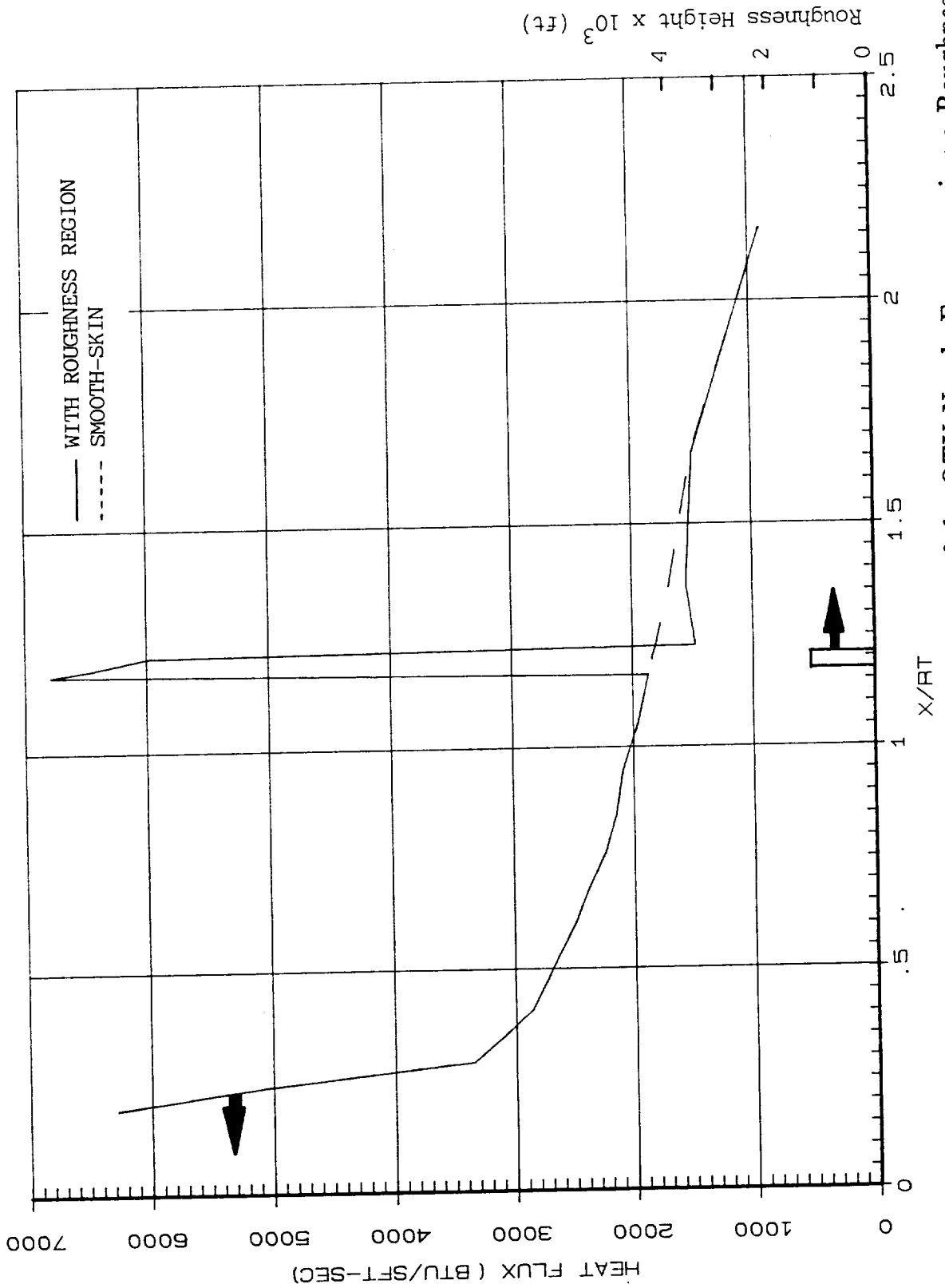
Figure 2.9: Heat Flux Distribution in a Limited Portion of the OTV Nozzle Encompassing a Roughness Region (RK = 0.00125 Ft.)

REMTECH
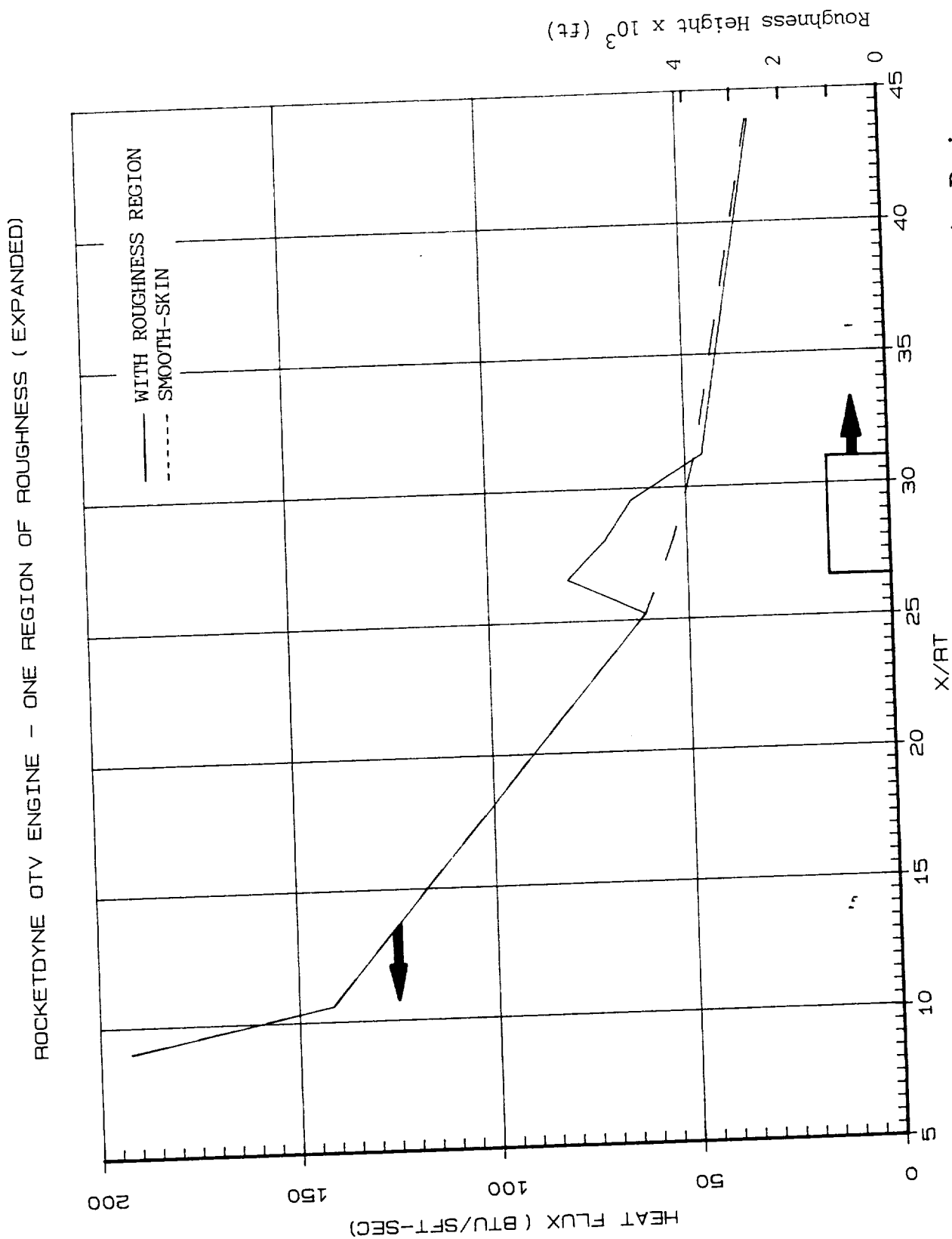
Figure 2.10: Heat Flux Distribution in a Limited Portion of the OTV Nozzle Encompassing Region (RK = 0.00125 Ft.)

Figure 2.11: Heat Flux Distribution in the OTV Nozzle with One Region of Roughness (RK = 0.00125 Ft.) at the Throat

REMTECH
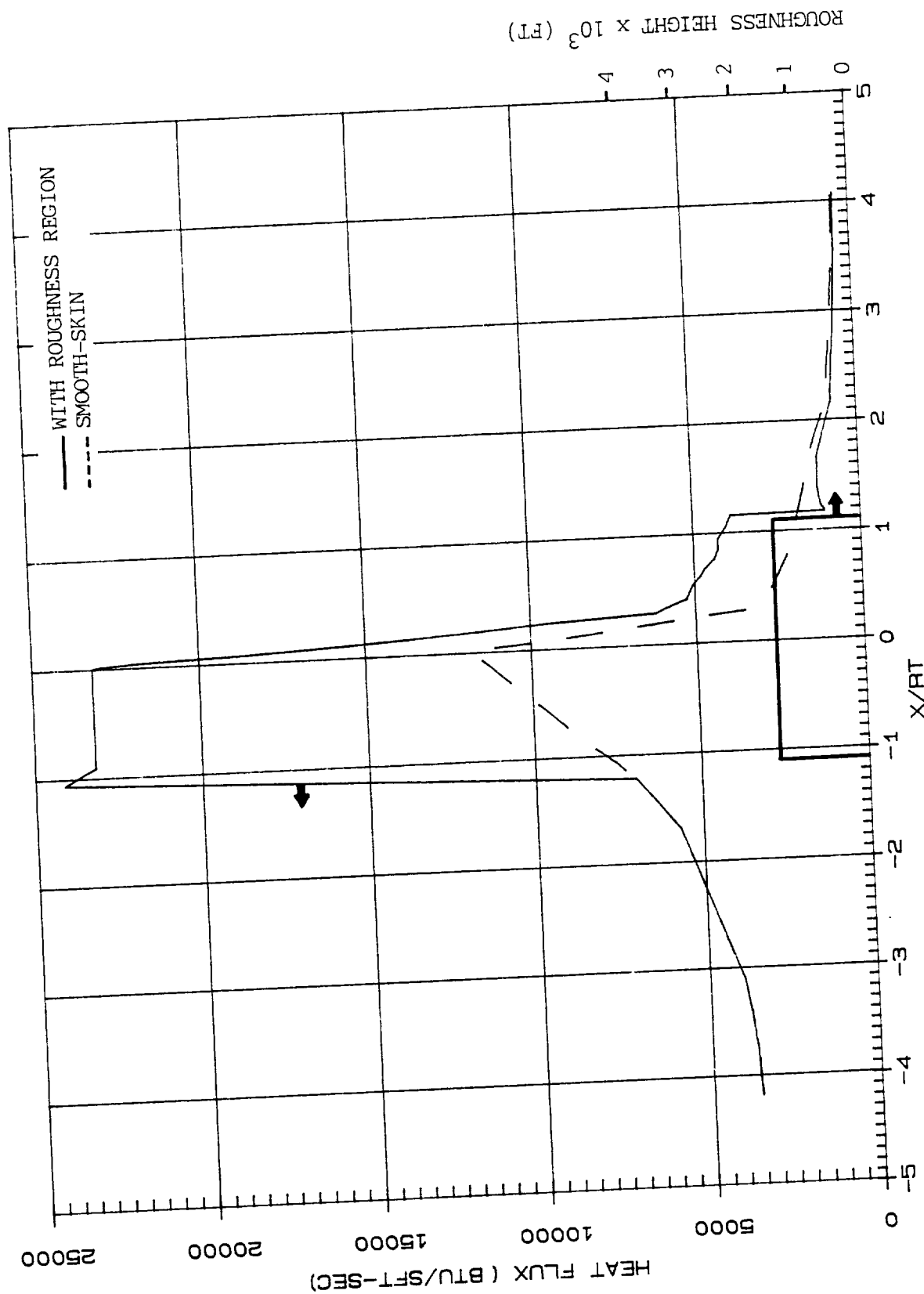
Figure 2.12: Heat Flux Distribution in a Limited Portion of the OTV Nozzle Encompassing a Roughness Region (RK = 0.00125 Ft.) - (Expanded Scale)
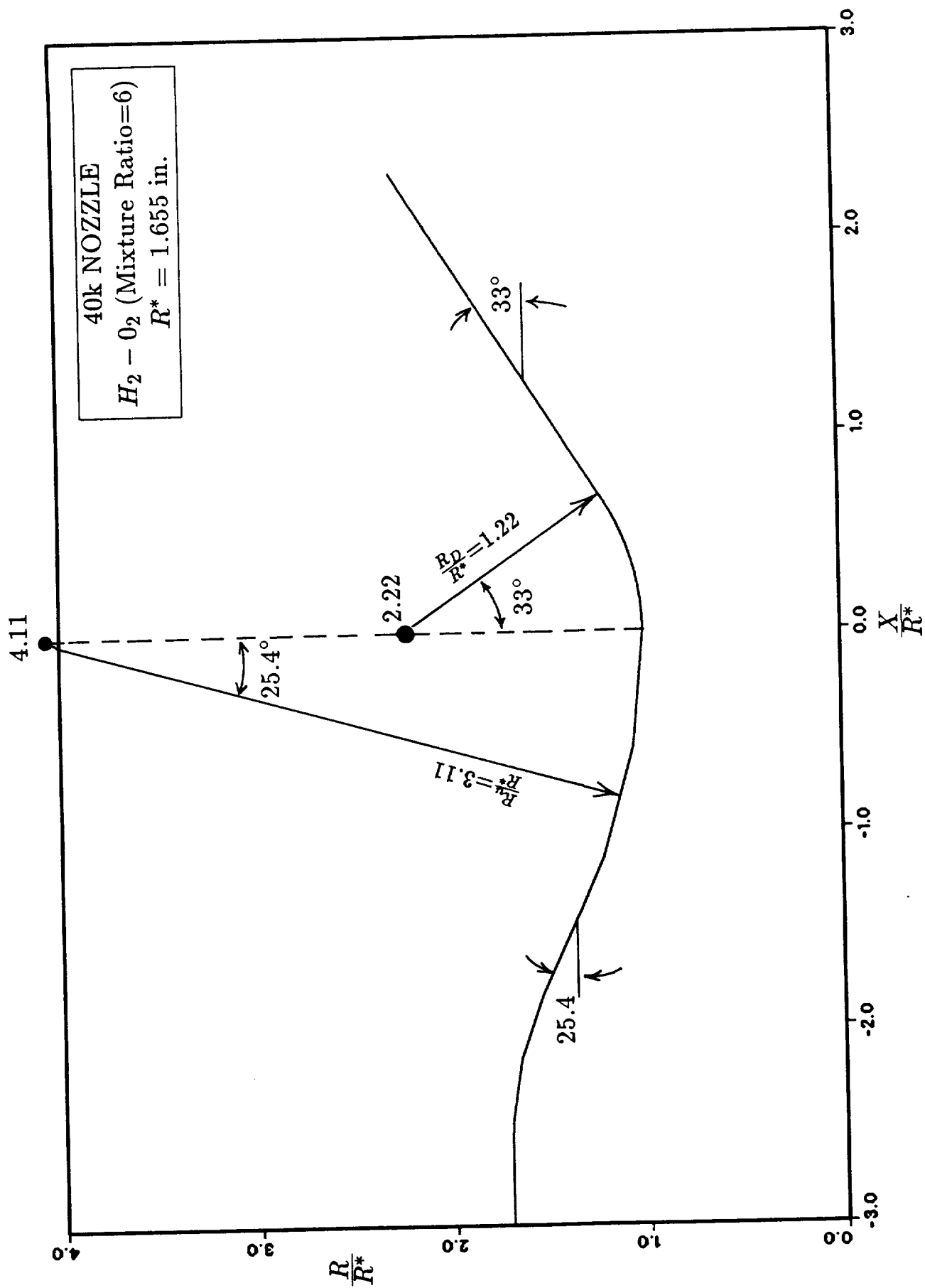
Figure 2.13: Geometry of 40-K Nozzle

40k NOZZLE
$H_2 - O_2$ (Mixture Ratio=6)
$R^* = 1.655$ in.

$33°$

$\frac{R_D}{R^*} = 1.22$

$33°$

2.22

$25.4°$

$\frac{R_u}{R^*} = 3.11$

4.11

25.4
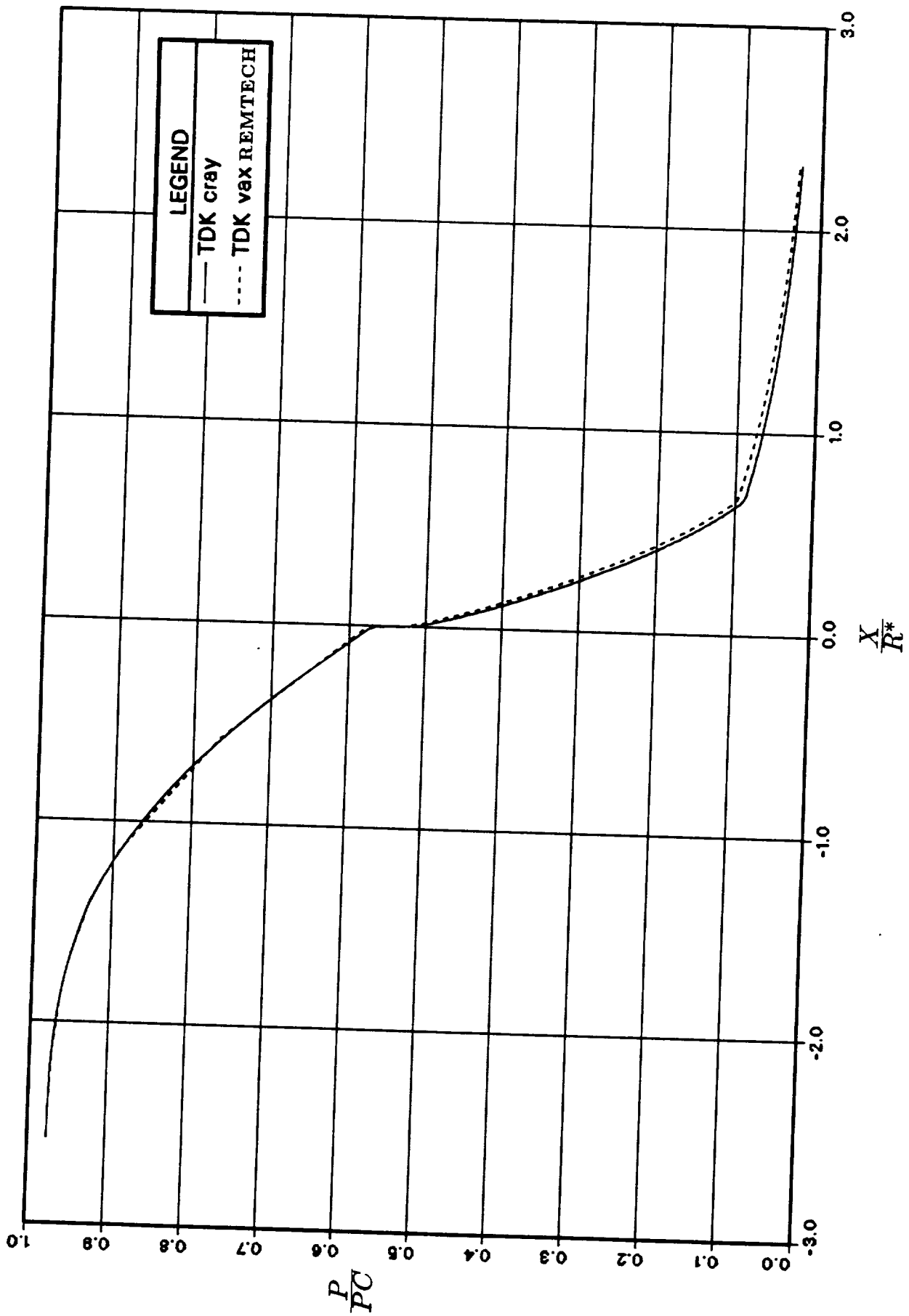
Figure 2.14: Pressure Distribution over the Nozzle Wall

REMTECH
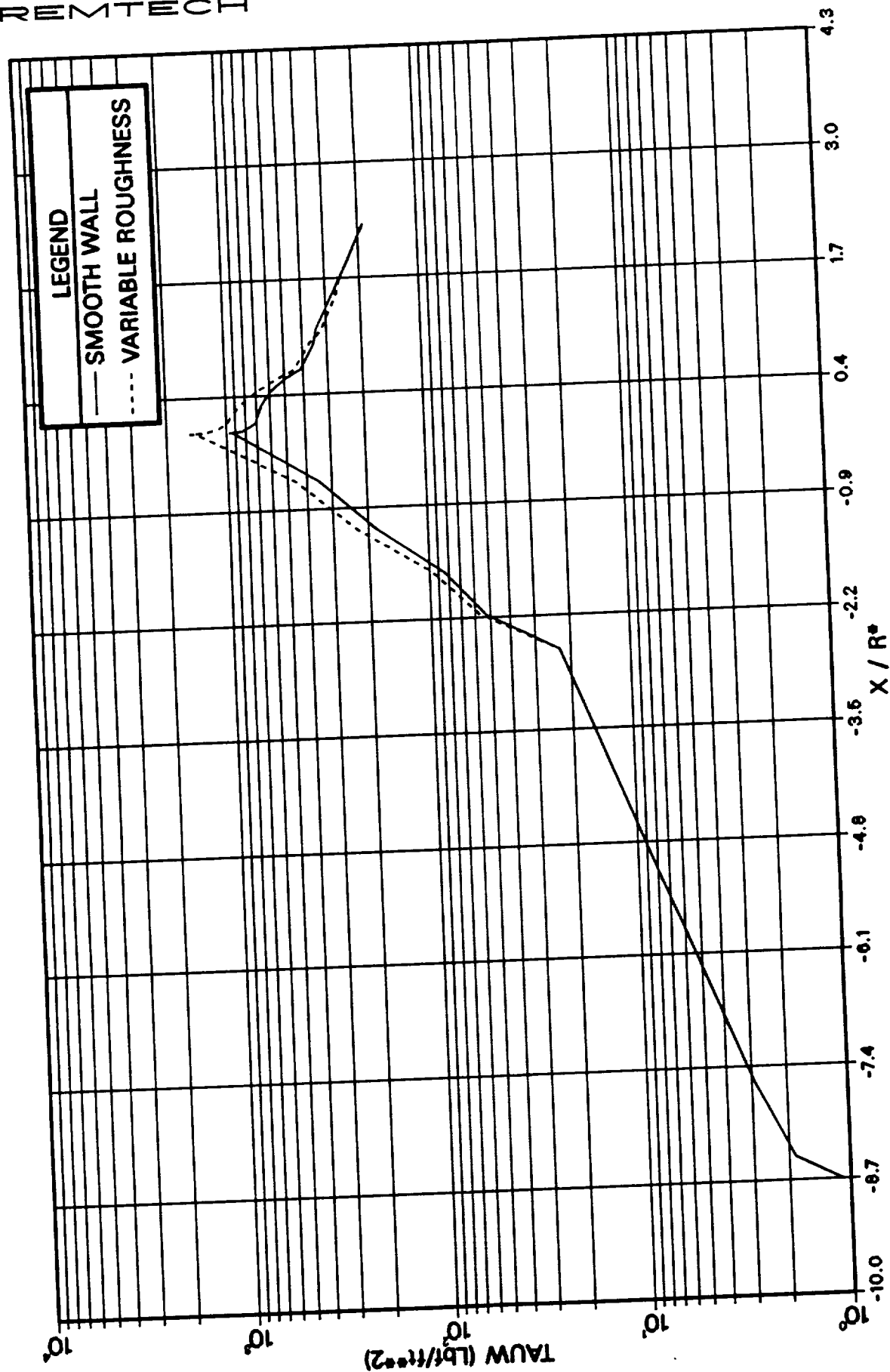
Figure 2.15: Wall Shear Stress Distribution
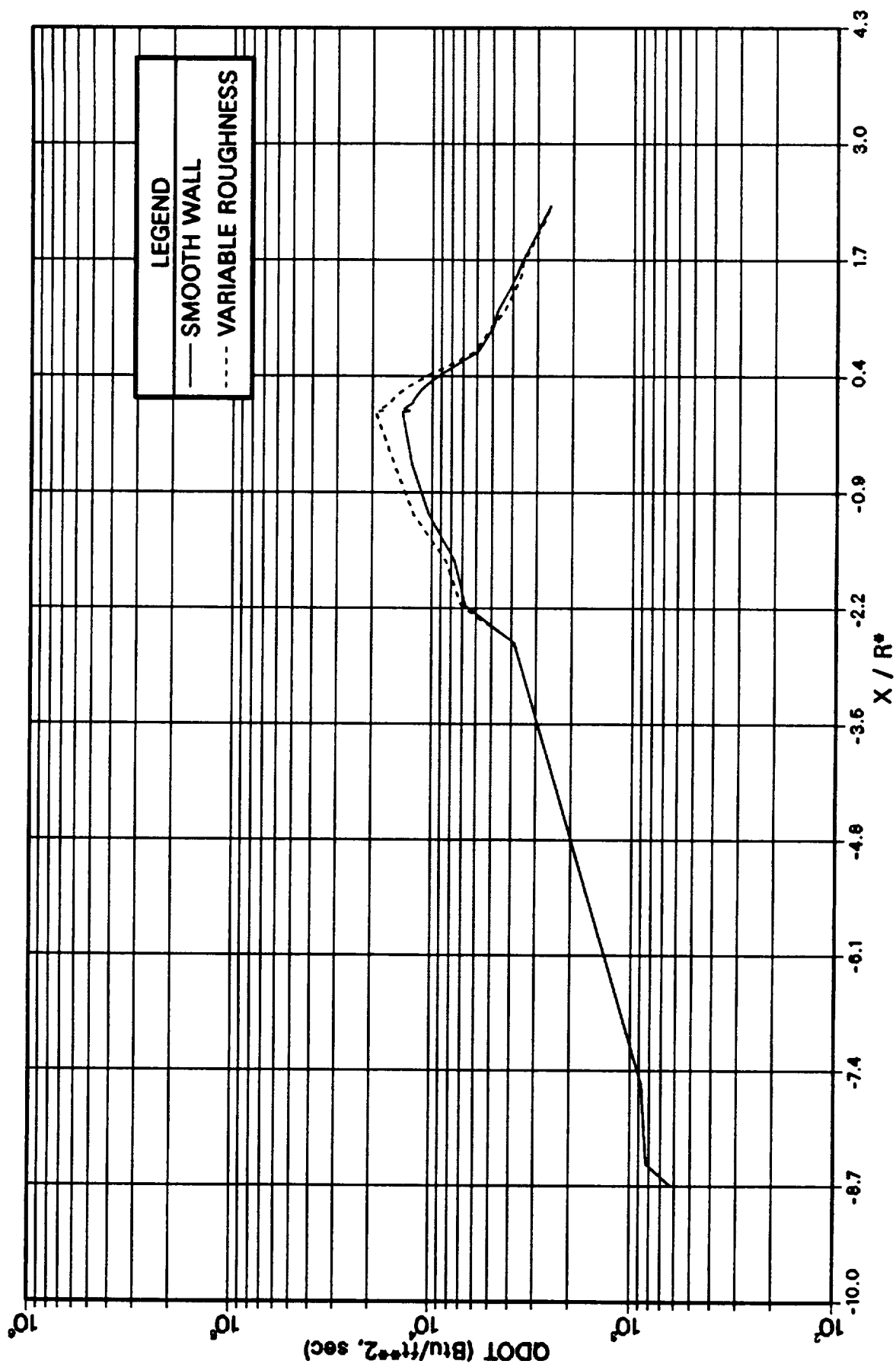
Figure 2.16: Wall Heat Transfer Distribution

REMTECH
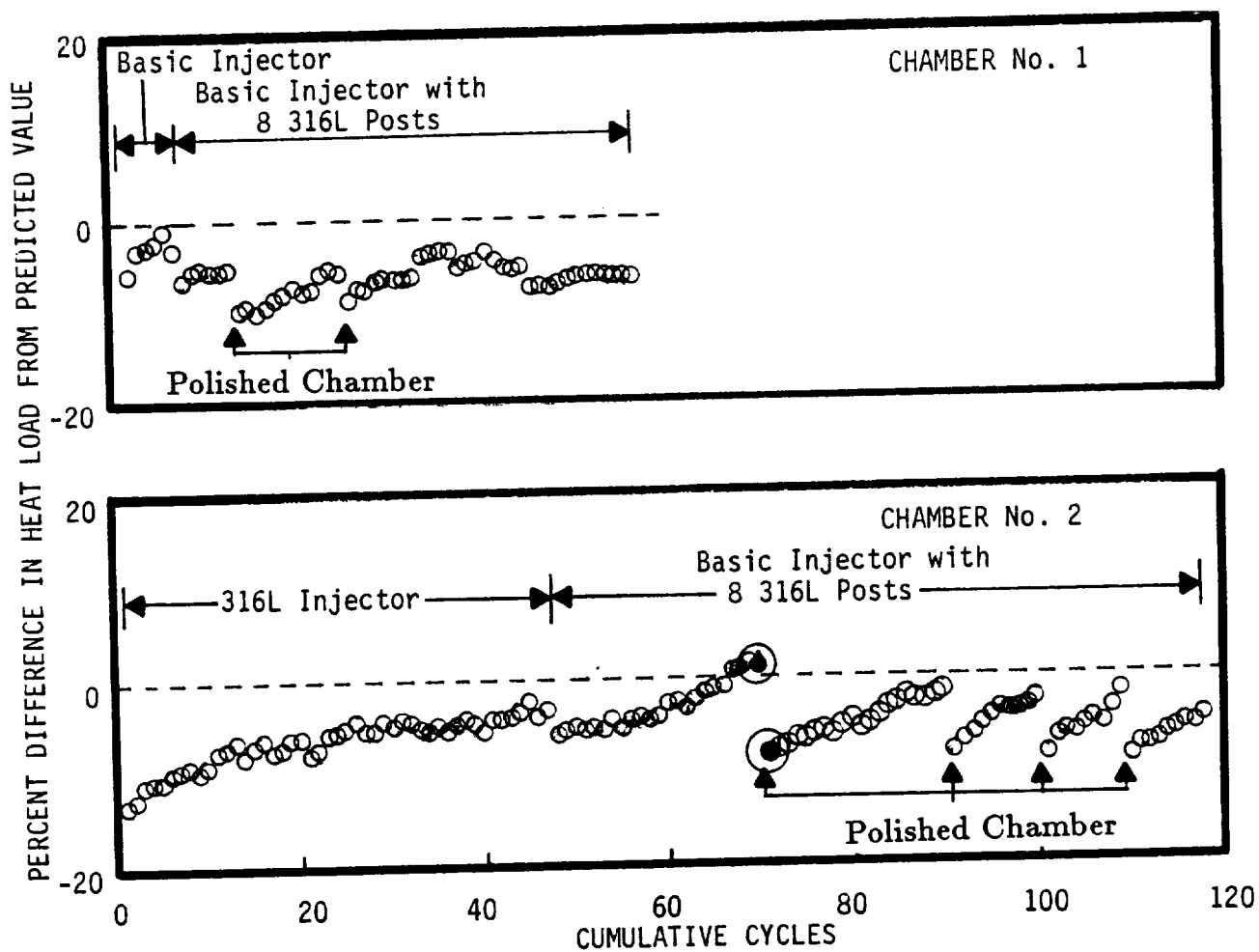
Figure 2.17: Heat Load Summaries for Chambers 1 and 2 and Comparison with BLIMPJ Prediction

23

REMTECH

Section 3

RELAMINARIZATION

3.1 Background

The prediction of relaminarization phenomena remains as one of the strongest tests of validity of the turbulence models existing in the literature. Relaminarization is basically a reversion from turbulence to laminar boundary layer, principally caused by severe flow acceleration effects. The original experimental work by such investigators as Launder [9], Patel et al. [10], Back et al. [11], and Nash-Webber [12] serves as the basis of understanding such a phenomenon. The work of Patel et al. concentrates on the large departures of the inner-law velocity distribution in the presence of severe favorable pressure gradients in the turbulent boundary layers. Launder et al., on the other hand, emphasize the measurements of turbulence and mean velocity profiles, and cover the complete reversal of the transition process. In the measurements by Back and Cuffel [11], and Reshotko et al. [6], a reduction in heat transfer was observed below values typical of a turbulent boundary layer was for regions of the nozzle where the flow acceleration is high. In these earlier works, a threshold value of acceleration parameter $K = \left(\mu_e \, / \, \rho_e U_e^2 \right) \left(dU_e \, / \, dx \right)$ of 2 to 3 $\times$ 10^{-6} was used to trigger laminarization. The shortcoming of such an approach lies in defining a degree of laminarization as the boundary layer makes a transition from turbulent to laminar flow as the flow accelerates in the nozzle. Attempts were made by investigators such as Hodge and Adams [13] who used the $k - \epsilon$ turbulence model in an accelerating flow and achieved reasonable correlation with data. However, the thrust of the current work has been to develop an engineering model to update the existing turbulence models in BLIMPJ. Attempts were made in Ref. [3] to utilize the experimental data of Nash-Webber, which is one of the best-documented experimental investigations of compressible boundary layer. However, the application of the developed criterion [3] was found to be only approximate when validated against measured data. The objective of this effort is to modify this criterion to apply to more general problems.

The modified acceleration parameter due to Nash-Webber is defined as,

$$K_W = \frac{\mu_w}{\rho_w U_e^2} \cdot \frac{dU_e}{dx} \tag{3.1}$$

REMTECH

where W and e denote wall and edge conditions, respectively. This parameter is distinctly different from the previous one in that both wall and edge quantities are considered here. K_W is affected by both acceleration in the inviscid boundary layer edge and wall conditions. The curve-fit recommended in Ref. [3] to define the threshold for the onset of relaminarization is given by,

$$K_W = a\,R^2 + b\,R + c \qquad (3.2)$$

$$\text{where} \quad \begin{aligned} a &= 8.935 \times 10^{-14} \\ b &= 2.239 \times 10^{-10} \\ c &= 1.0248 \times 10^{-6} \end{aligned}$$

and R is Reynolds Number defined by,

$$Re_\theta = \frac{\rho_e\, U_e\, \theta}{\mu_W} \qquad (3.3)$$

The definition of Reynolds number here is somewhat different from its usual one. Nash-Webber cites this form to be most logical for the needs of the problem under consideration. The upper limit of the relaminarization process where the turbulence production is fully suppressed, was put at Kline's suggested value of 3.5×10^{-6}. (Fig. 3.1)

Since this criterion worked only approximately for the Back and Cuffel nozzle data as shown in Ref. [3], the original report of Nash-Webber was closely examined. The following facts and suggestions were revealed:

1. The Nash-Webber correlation was valid for adiabatic wall condition.

2. The transition line should be moved down for cooled walls, i.e., it is easier for turbulent flow to laminarize on cooled walls.

3. It should be moved up for rough walls, i.e., the phenomenon is the opposite of cooled wall flow.

3.2 Effects of Wall Roughness and Strong Regenerative Cooling

3.2.1 Effects of Wall Cooling

It is extremely difficult to locate appropriate data to quantify the effects of wall cooling on relaminarization. One set of data was available in Ref. [6]. The data

available for $P_c = 75$ psia and 30 psia from smooth wall conditions in this work are candidates for establishing the appropriate limits for the transition regime. The experimental data taken on the 60°-15° half-angle conical nozzle were obtained for three levels of chamber pressure: 30, 75, and 300 psia. In the previous section the high pressure condition has been shown to be turbulent over the whole length of the nozzle. The high chamber pressure yields a high enough momentum thickness Reynolds Number that the flow remains turbulent, even though the flow acceleration is quite high. However, as the chamber pressure was reduced by an order of magnitude, the initially turbulent boundary layer does not stay turbulent as the flow accelerates. Figure 3.2 compares the measured heat transfer levels at four roughness levels for each of the chamber pressures, $P_c = 30$, and 75 psia separately. Figure 3.3 compares fully turbulent prediction, fully laminar prediction and measured heat-transfer coefficients distribution over the length of the above nozzle for $P_c = 30$ psia. It is seen that the data line is between the turbulent and laminar distributions. Although the data is originally turbulent, it comes closer to the laminar prediction as the flow accelerates. The relaminarization flag was turned on to observe the effects of acceleration, but the prediction was far from satisfactory, indicating that the limits of laminarization, previously coded, were inadequate.

The report of Nash-Webber was examined to check the above limits. It was discovered that his turbulent-laminar transition limit was based on adiabatic wall condition. However, this report recommended modifications to be made for cooled wall. Therefore, a study was undertaken to quantify these modifications by comparing against measured data. To establish these limits, the measured data were compared against fully turbulent and fully laminar computations. This exercise showed where transition from laminar to turbulent or turbulent to laminar flow took place. The next thing was to obtain the $K_W - Re_\theta$ trajectory of the flow as it accelerates through the nozzle. Now, if the data showed that it remained laminar throughout, no upper limit of laminarization on K_W could be obtained from this set of data. In fact, this was true of the smooth-wall data for $P_c = 30$ psia, as can be seen in Fig. 3.3. Because of high flow acceleration in the nozzle entrance for the LeRC 60° - 15° half-angle conical nozzle (Fig. 2.2), almost all the data, including this set, laminarized at the nozzle inlet and some made transition to turbulent flow depending on Reynolds Number and the corresponding acceleration parameter. It was necessary to examine the $P_c = 75$ psia smooth-wall data (Fig. 3.2), where the data seem to be on the verge of transition right around the throat. This supplied the upper limit, K_{W_u}, which was assumed to be independent of Re_θ. However, this set of data did not go all the way to the turbulent limit, and thus was unable to supply a lower limit, K_{W_l}. This data point is represented by a circular symbol at $K_r = 0$ in Fig. 3.5.

3.2.2   Effects of Surface Roughness and Wall Cooling

Examination of the 60° - 15° half-angle nozzle data showed that the presence of roughness slows relaminarization and as the roughness increases, the transition to turbulent flow occurs earlier on the nozzle wall. It was very quickly discovered that the limits of K_W, established in Section 3.2.1, for the cooled wall situation were invalid for walls containing surface roughness. These limits somehow needed to implicitly depend on surface roughness height.

It is well known in the literature that the effects of roughness and acceleration on wall heat transfer are opposite in nature. Computations were made using the $P_c = 30$ psia case with a given roughness height of 325 μ in RMS. By considering purely turbulent and laminar boundary layers separately and comparing against measured data in Fig. 3.4, it is found that the data is basically turbulent throughout the nozzle. This observation is somewhat different from that made in the above report [6] where this data was considered transitional in the region upstream of the nozzle throat. When the relaminarization flag was turned on, it yielded lower values for heat-transfer coefficients, thus indicating that the coded limits of relaminarization are inadequate.

The work of Coleman, Moffat, and Kays [14] throws some light on this by defining a new parameter called the "Roughness Acceleration Parameter," K_r, in the following way:

$$K_r = \frac{K_s}{U_e} \cdot \frac{dU_e}{dx} \tag{3.4}$$

The measured data from the above test were correlated for various K_r values using the procedure described in the previous subsection. It was possible to find both the transition limits from appropriate sets of this data undergoing transition from laminar to turbulent flow and, finally, reaching the turbulent level. All these data were correlated in Fig. 3.5, where the symbols ⊙ and ☐ represent data from $P_c = 75$ and 30 psia, respectively. The $P_c = 300$ psia did not provide any useful information in this plot since the Reynolds Numbers are much larger in magnitude, resulting in practically no laminar flow along the nozzle. Straight lines were drawn as approximations through the data to analytically represent the correlation. It should be pointed out that the lower curve represents only the constant 'c' in Eq. 3.2 and that the quadratic nature of K_{W_l} was still maintained. In other words, knowing the value of Re_θ and K_{W_l} where the transition to complete turbulent flow takes place, the constant 'c' representing K_{W_l} at $Re_\theta = 0$ is obtained from this equation. These correlations were then coded in BLIMPJ.

3.3 Concept Checkout

To illustrate the use of the correlations developed earlier, BLIMPJ was run for the three following cases for the same nozzle, by turning on the relaminarization flag:

1. $P_c = 30$ psia
   Smooth Wall

2. $P_c = 75$ psia
   $K_s = 325\ \mu$ in RMS

3. $P_c = 75$ psia
   $K_s = 120\ \mu$ in RMS

Figure 3.6 (Case 1) shows that the data is basically laminar throughout the nozzle until the calculation tends to be turbulent at $X/R_T \sim 0.5$. This is only artificial, since the acceleration parameter jumps down because of a pressure slope discontinuity (Fig. 2.3) given by TDK at the throat/nozzle juncture. Figure 3.7, on the other hand, represents Case 2 where the data are seen to be turbulent throughout the nozzle. The next case (Fig. 3.8) is more interesting in that the flow makes a transition from the laminar to the turbulent regime in the presence of wall roughness and finally becomes fully turbulent downstream of the throat. The variation of K_w and Re_θ with x for this case is given in Fig. 3.9, whereas Fig. 3.10 shows a cross-plot of K_W and Re_θ (R_W - Re_θ trajectory of the flow) along with the upper and lower limits of transition. The heat-transfer prediction for this case as given in Fig. 3.8 seems to be only approximate, and fine-tuning of the transition-limit correlation is necessary to improve the BLIMPJ prediction.

Since the transition-limit plot was derived from a limited set of data, the correlation must be used with caution. In order to make the correlation complete, much more data must be examined and the correlation updated. The current work provides only a guide for engineering calculations. One quick glance at the Back-Cuffel data [11] which was examined by the current authors [3] shows that the use of this correlation would, in fact, lower the prediction to a laminar level and would compare much better with their measured data.

3.4 Impact of Free-stream Turbulence

Free-stream turbulence in liquid rocket nozzles is caused by the violent mixing at the injector and by the explosive burning of the fuel-oxidizer mixture in the

REMTECH

combustion chamber. The role of free-stream turbulence in gas-turbine systems has long been recognized and has been measured in certain situations. These studies indicate that the primary effect of an increase in free-stream turbulence is the upstream movement of the onset of transition. The effects of free-stream turbulence on turbulent boundary layer profiles have been found by others to give slightly fuller profiles and higher turbulence levels, resulting in higher momentum thicknesses, smaller form parameters, and increased heat transfer as well as skin friction coefficients. In analyzing the combined influence of free-stream turbulence and pressure gradient, it has been shown for nearly isothermal flows that the sign of the pressure gradient is of dominant importance. Adverse pressure gradients promote the onset of transition, whereas favorable pressure gradients stabilize the boundary layer and thus counteract the effect of free-stream turbulence. In the rocket nozzle situations, where relaminarization is a possibility because of high favorable pressure gradients, free-stream turbulence will delay relaminarization.

More recently, Huffman et al. [15] and Charnay et al. [16] have measured in detail the effects of free-stream turbulence upon both the mean and fluctuating components of velocity within a turbulent boundary layer. These measurements show very clearly the extremely large effect of free-stream turbulence upon the turbulent transport in the outer region of the boundary layer. Huffman et al. observed as much as a sixfold increase in the conventionally defined Prandtl's mixing length in the center region of the boundary layer with about 5 percent free-stream turbulence. Examples of measurements and predictions by McDonald et al. on a flat plate with constant pressure in the streamwise direction are given in Ref. [17], where the effects of free-stream turbulence on skin friction, streamwise velocity, mixing length, turbulent kinetic energy and Reynolds shear stress are clearly seen. The investigation by Hodge and Adams [13] also considered the effects of free-stream turbulence in their Integrated Kinetic Energy of Turbulence (IKET) approach.

An experimental investigation carried out by Rued and Wittig [18] shows the effects of free-stream turbulence both in zero and negative favorable pressure gradients. The Reynolds analogy, $2 \cdot St/C_f$, is shown to be largely independent of the turbulence level. The analogy factor is observed to be constant with a mean value of 1.1, which leads to the conclusion that heat transfer rates increase in the same amount as the skin friction coefficients, at least in the case of zero pressure gradient. It can also be said from the work of Ref. [18], without reproducing their results of measurements here, that favorable pressure gradients tend to laminarize the turbulent flow, whereas free-stream turbulence tends to oppose the above effects.

In the current BLIMPJ framework, a lot of simplifications had to be made to

REMTECH

integrate the effects of free-stream turbulence into the algorithm. The relationship between turbulence intensity and Reynolds shear stress has been dealt with in various references including Hodge and Adams [13]. The proportionality between these two quantities depends on whether one is considering the inner or the outer layer and also on the nature of the boundary layer, incompressible or compressible. Roughly speaking, for isotropic turbulence

$$\overline{u'v'} = \psi \, \overline{u'^2} \qquad (3.5)$$

where the correlation coefficient, ψ, is approximated to be -0.45. The free-stream turbulence level, T_u, is given by,

$$T_u = \frac{\sqrt{\overline{u'^2}}}{U_e} \qquad (3.6)$$

Thus, from Eqs. 3.5 and 3.6,

$$\left(\overline{u'v'}\right)_{\text{Boundary Layer Edge}} = \psi \, U_e^2 \, T_u^2 \qquad (3.7)$$

This was converted to an equivalent EPSA ($\equiv \rho^2 \epsilon / \rho_e \mu_e$) value in subroutine TRMBL with the proper non-dimensionalization at the boundary layer edge of each station. The OTV nozzle was used as a test case for $U_e T_u = 200$. Since U_e increases continuously in the nozzle as the flow expands, the value of T_u drops off from 107.0 percent at the inlet to 1.24 percent at the nozzle exit, as shown in Fig. 3.11. The variation of EPSA is given for stations 6, 12, and 20 in Figs. 3.12, 3.13 and 3.14, respectively. As clearly seen, the effects of free-stream turbulence (with their magnitudes shown in Fig. 3.11) are much more significant in the EPSA profile for Sta. 6 compared to the other two stations. Wall shear stress values are plotted in Fig. 3.14, whereas $\Delta TAUW$ is plotted in Fig. 3.16. No validation could be made because of lack of relevant available data. However, the increase in shear stress at the wall due to free-stream turbulence is apparent. Similar plots were made for heat transfer rates in Figs. 3.17 and 3.18. The disturbing negative values for $\Delta QDOT$ in Fig. 3.18 are attributed to the "non-convergence" of the solution at Sta. 3 and its effects on the subsequent two stations. It is believed that this "non-convergence" occurred because of high T_u values in the first few stations in the BLIMPJ run.

The approach described above, even though innovative, must be checked out against other codes and any available data before it can be used as a reliable engineering tool.

REMTECH
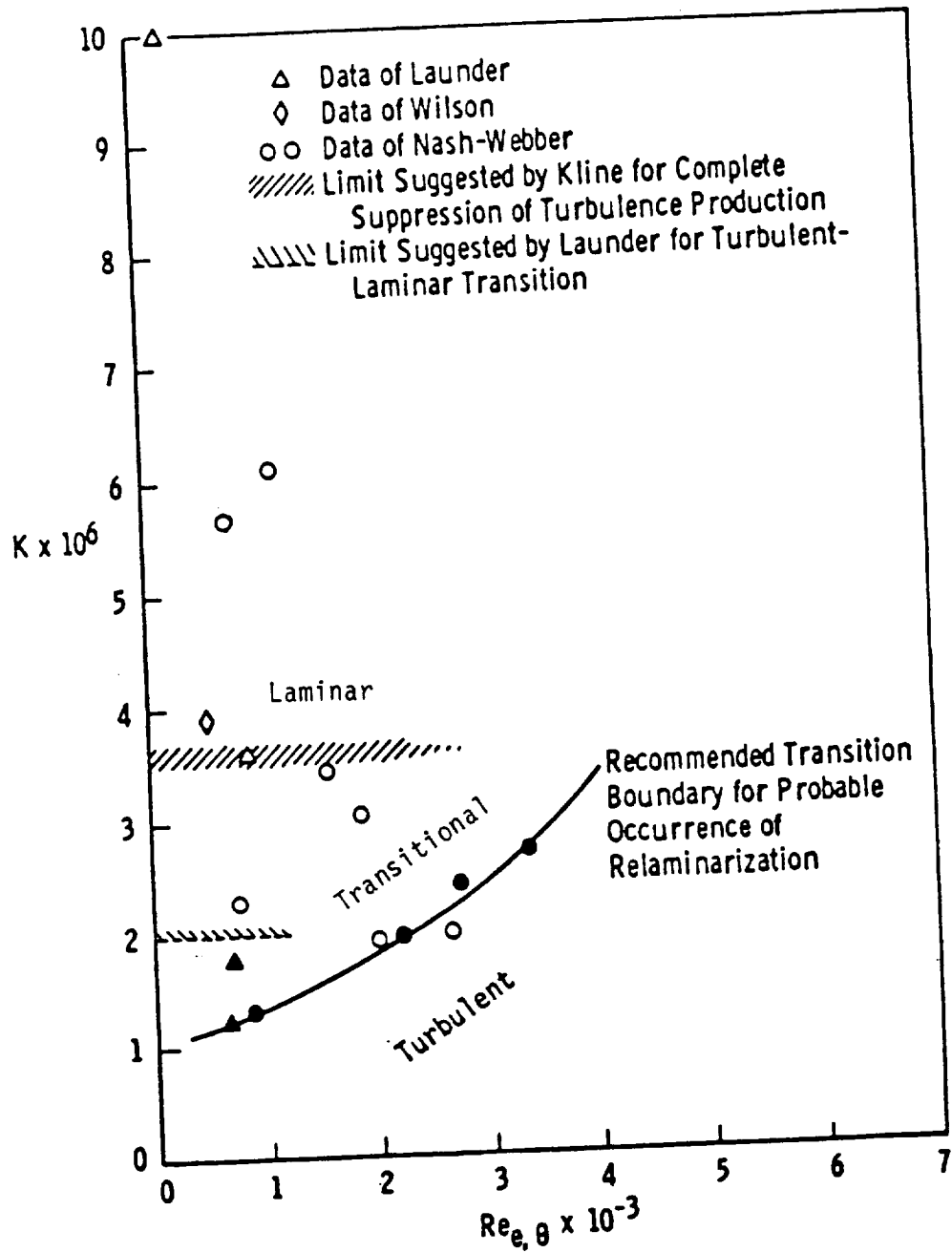
Figure 3.1: Turbulent-Laminar Transition Boundary

REMTECH
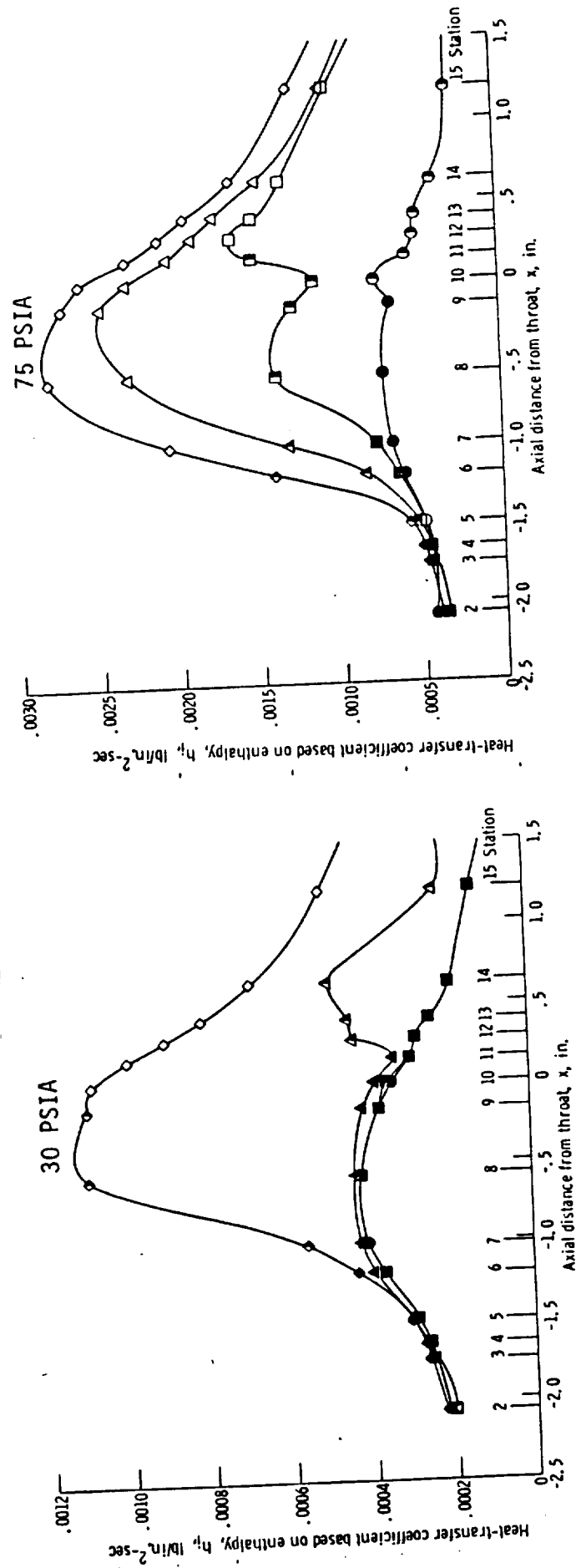
Figure 3.2: Measured Data for $Pc = 30$ and 75 psia with Four Roughness Levels
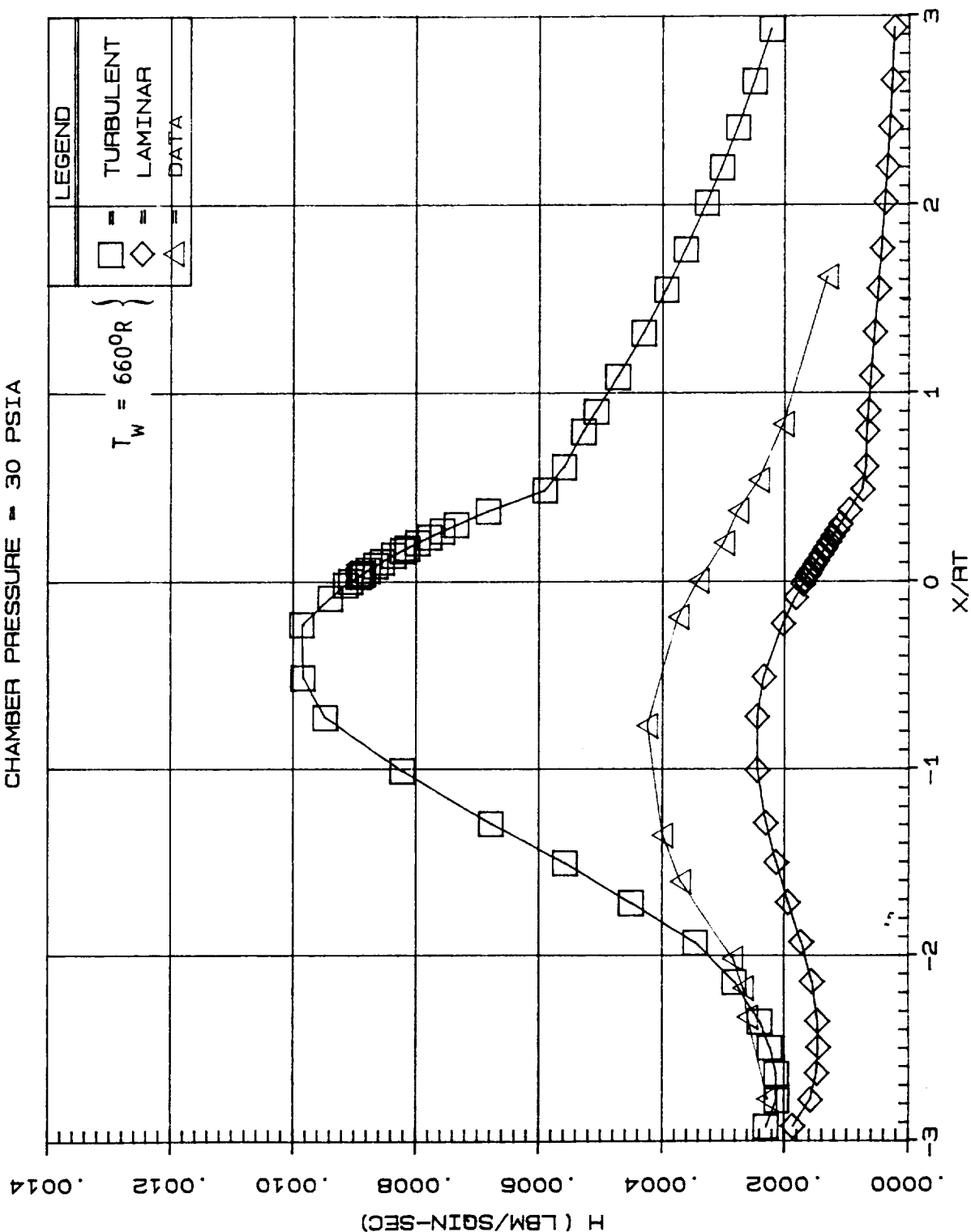
Figure 3.3: Comparison of Measured Data with Turbulent and Laminar Predictions
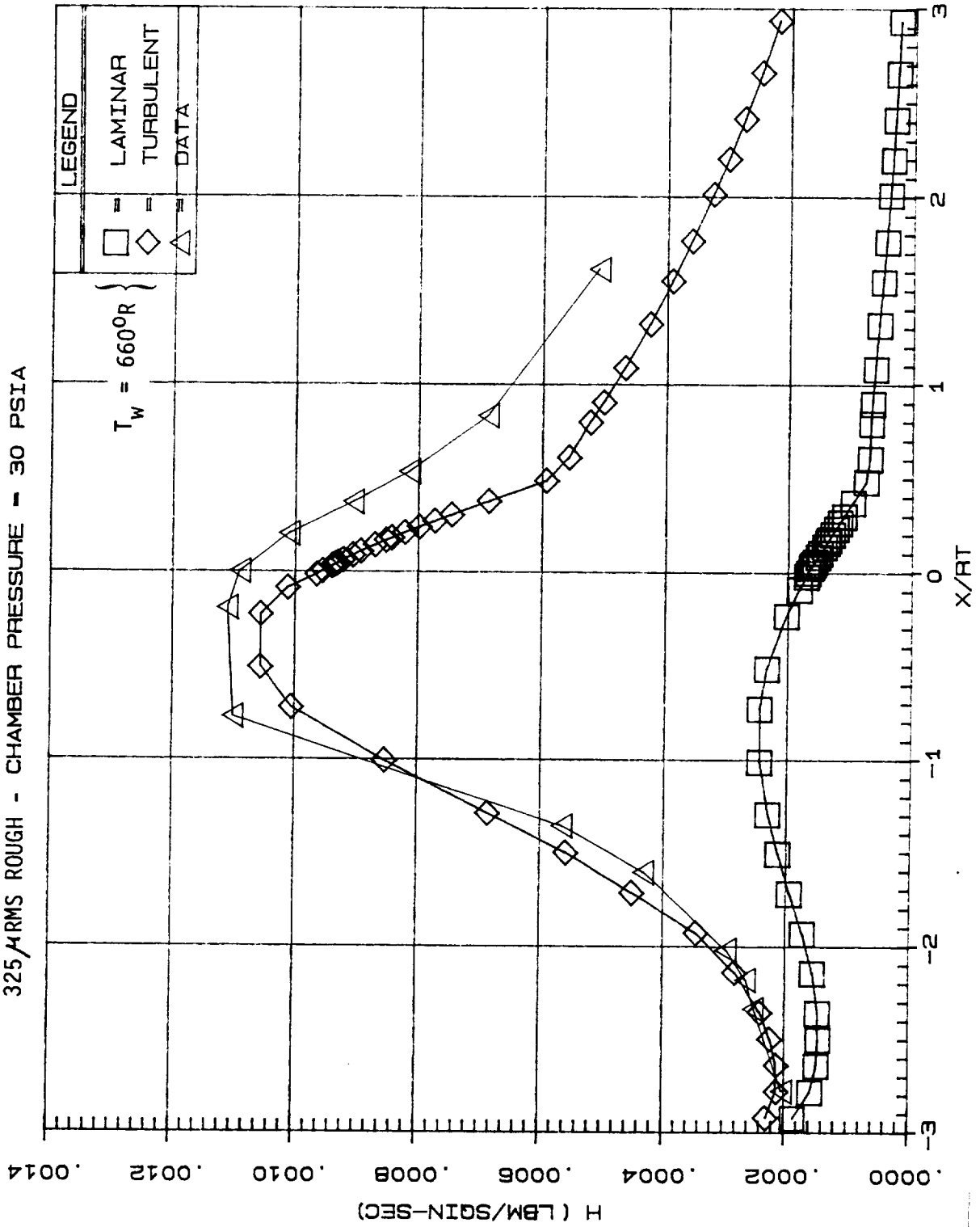
Figure 3.4: Comparison of Rough-Wall Data with Turbulent Rough-Wall and Laminar Predictions

P_c = 30 PSIA $\longrightarrow$ 300 PSIA

K_s = 0, 120, 175, and 325 μ IN.

⊙ 75 PSIA
⊡ 30 PSIA
"∕" REPRESENTS LOWER LIMIT

LAMINAR

TRANSITIONAL TURBULENT

K_{w_u} x10^6

K_{w_L} (Re$_\theta$ = 0) x 10^6

K_r x 10^4
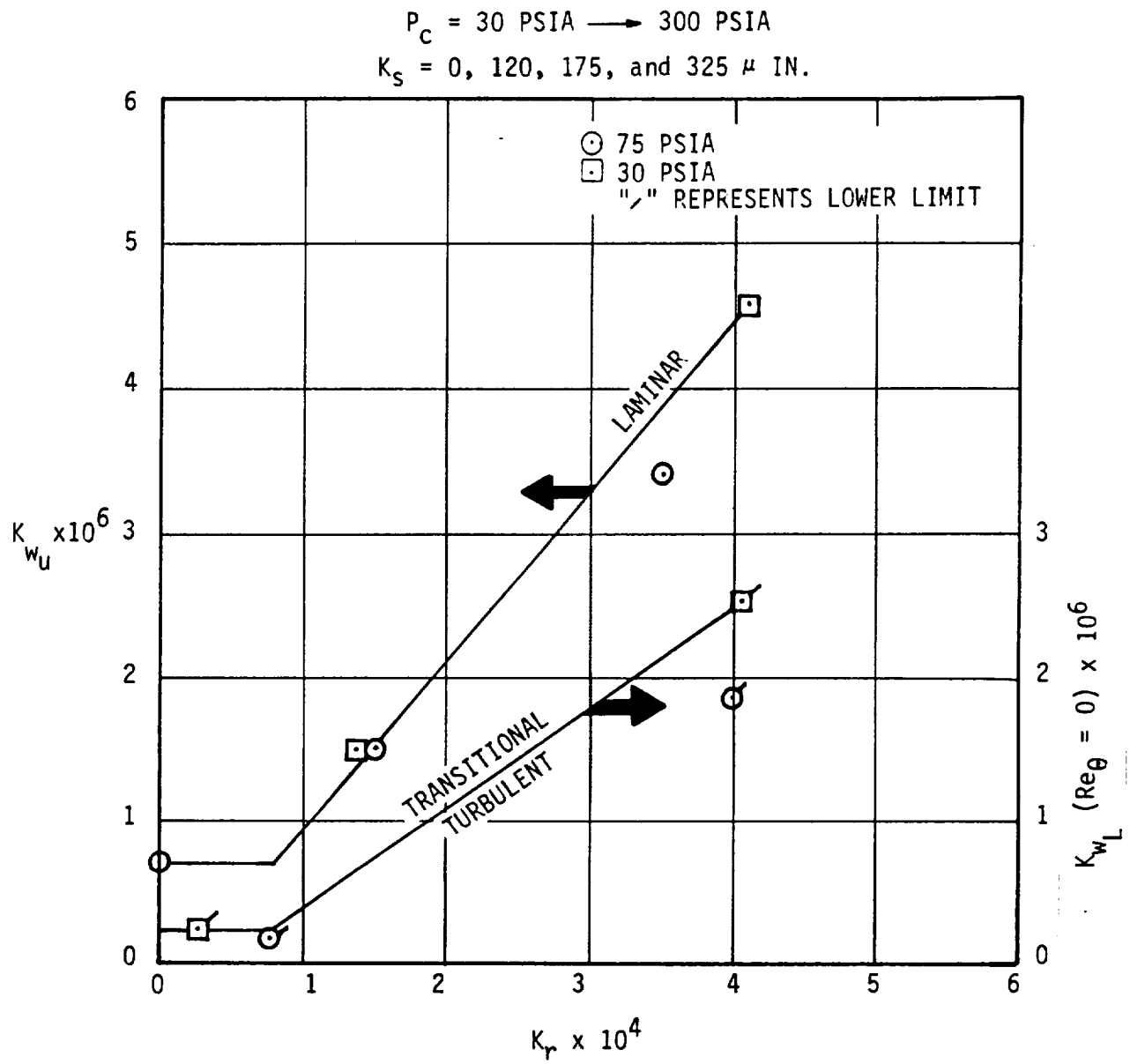
Figure 3.5: $K_W - K_r$ Correlation

ILAMIN = 1 (Relaminarization Flag Turned On)

P_c = 30 PSIA
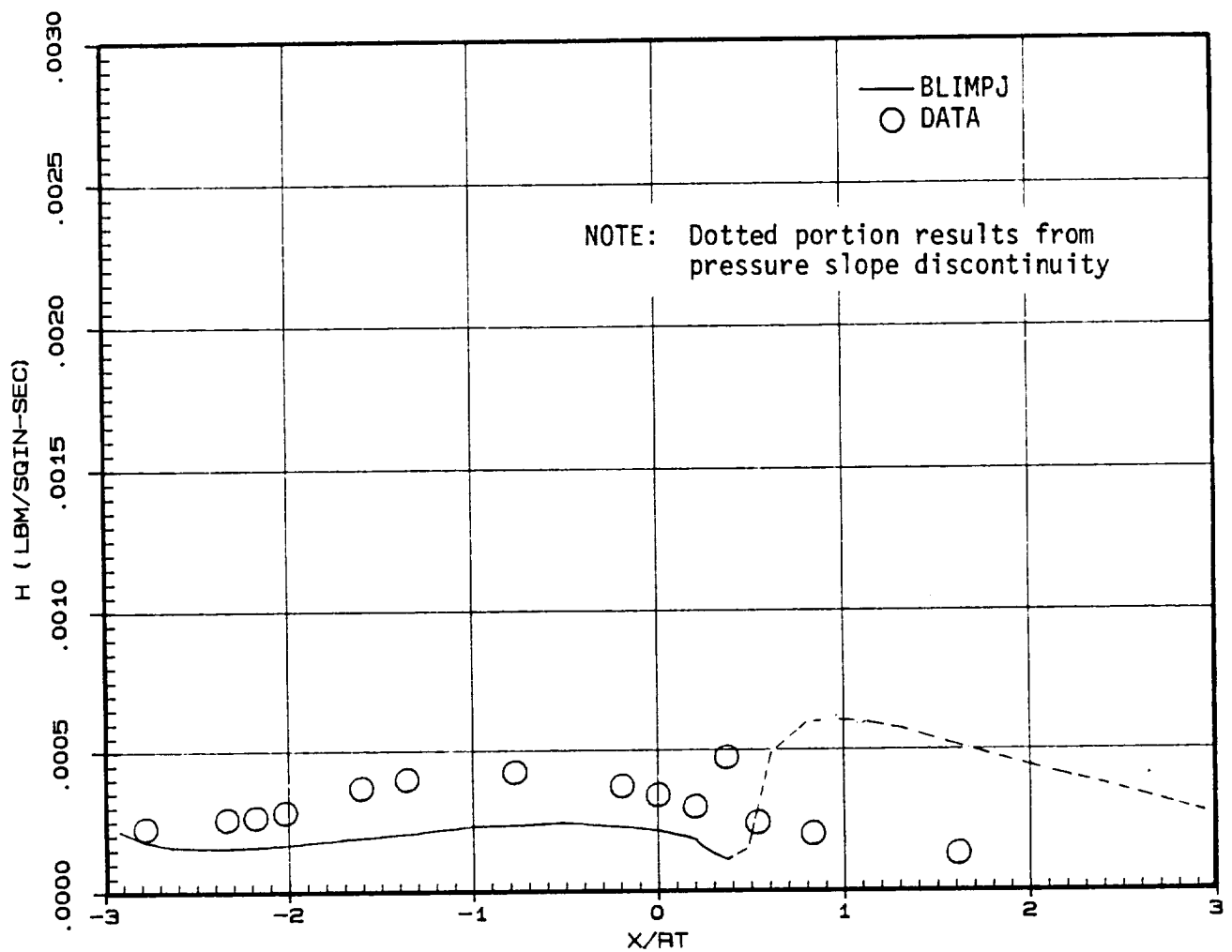
Figure 3.6: Heat-Transfer Coefficient Distribution for Smooth Wall

ILAMIN = 1

P_C = 75 PSIA, K_S = 325 μ RMS
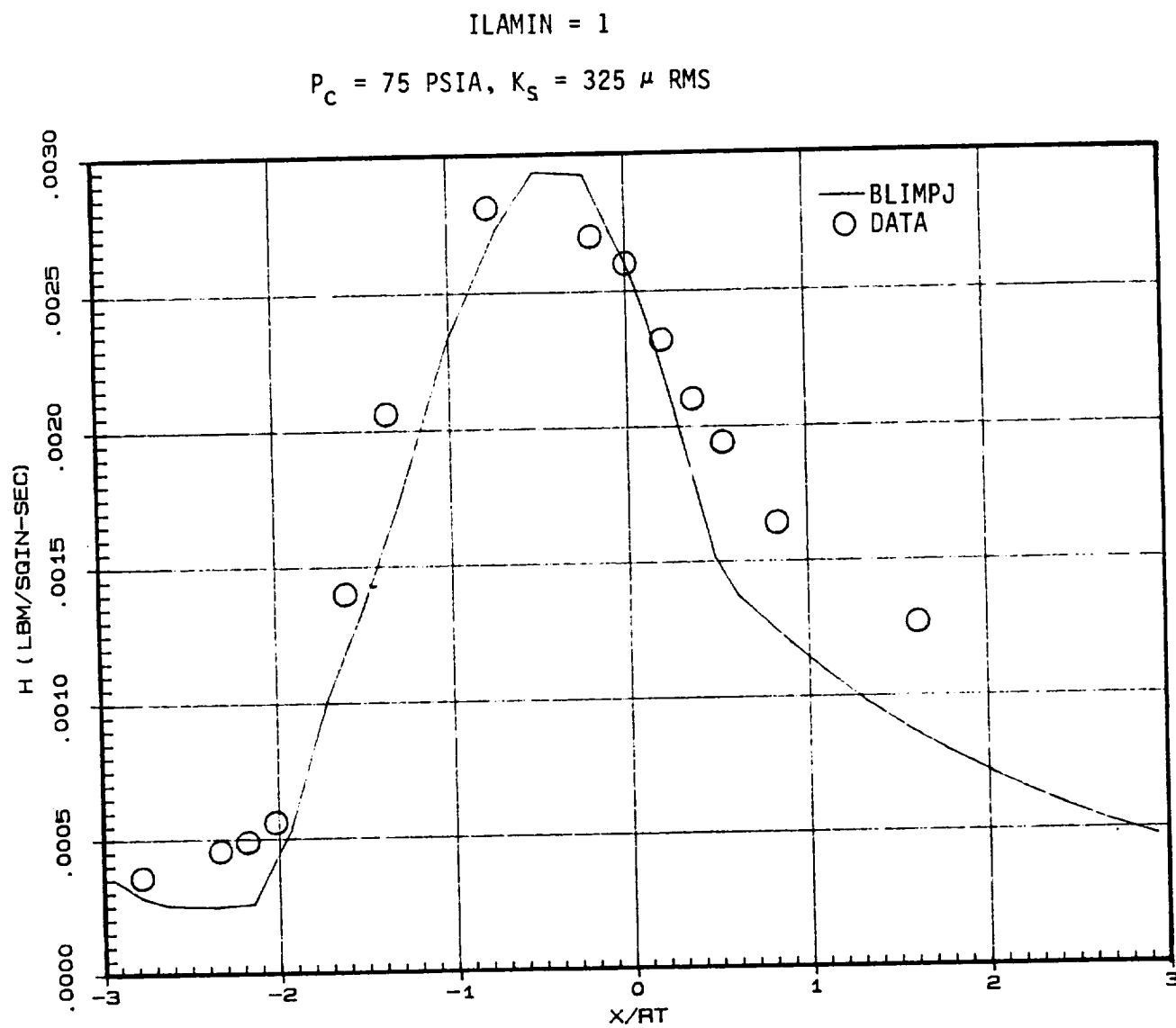
Figure 3.7: Heat-Transfer Coefficient Distribution for Rough Wall

$P_c = 75$ PSIA

$K_S = 120 \mu$ RMS
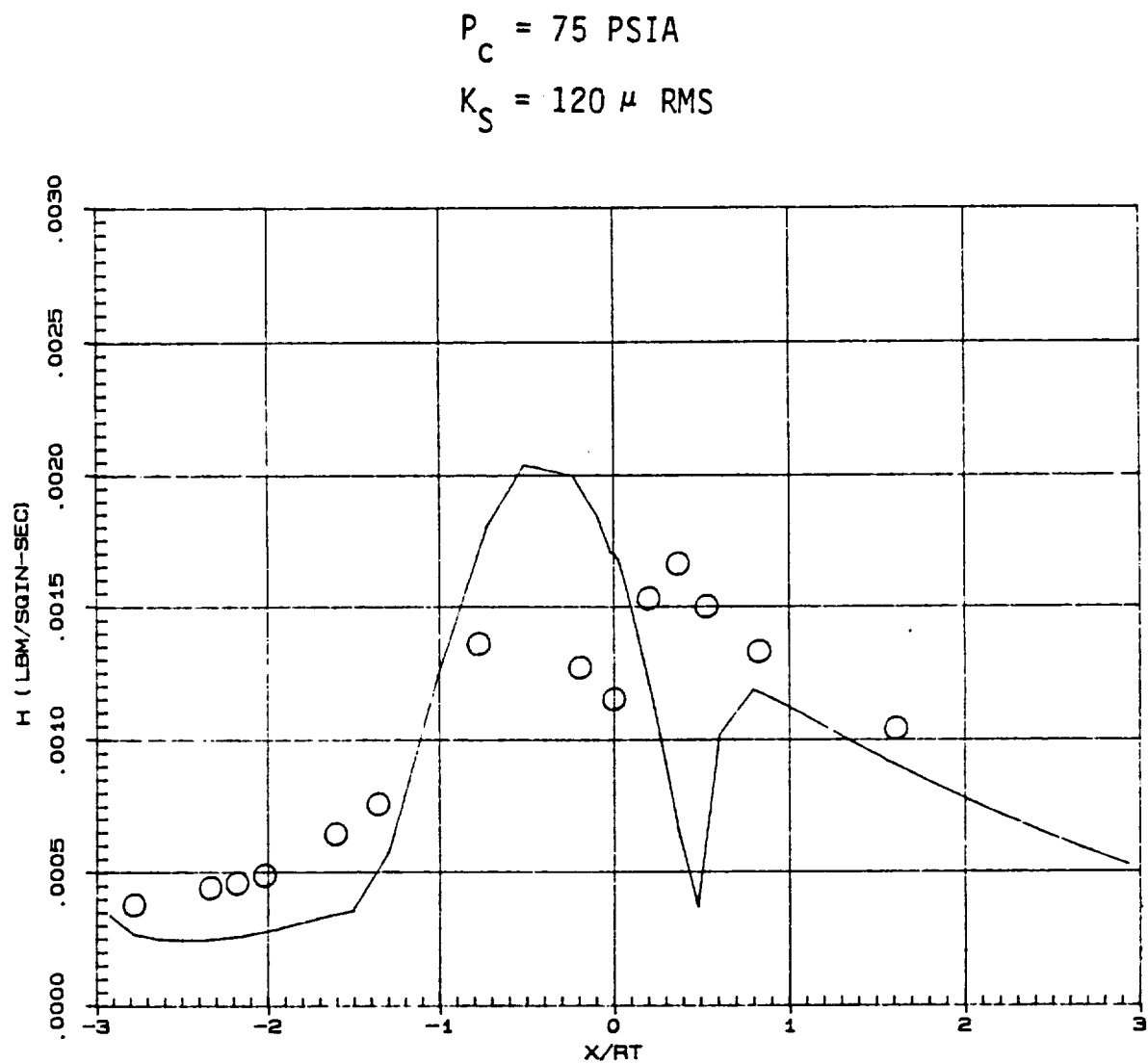
Figure 3.8: Heat-Transfer Distribution for Rough Wall

REMTECH
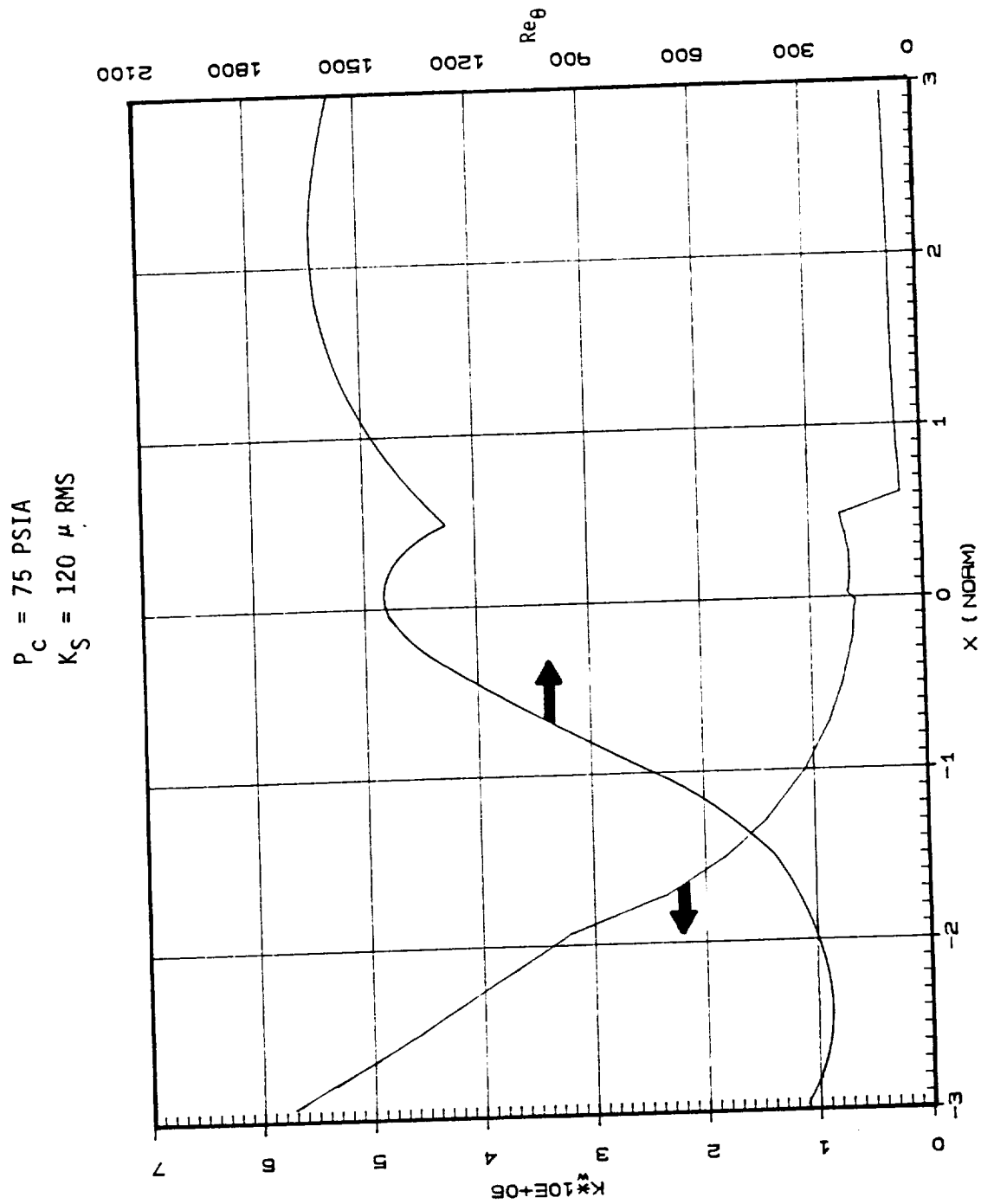
Figure 3.9: Variation of K_W and Re_θ vs. X/R_t for the Case in Fig. 3.8

$$P_c = 75 \text{ PSIA}$$

$$K_S = 120 \mu \text{ RMS}$$
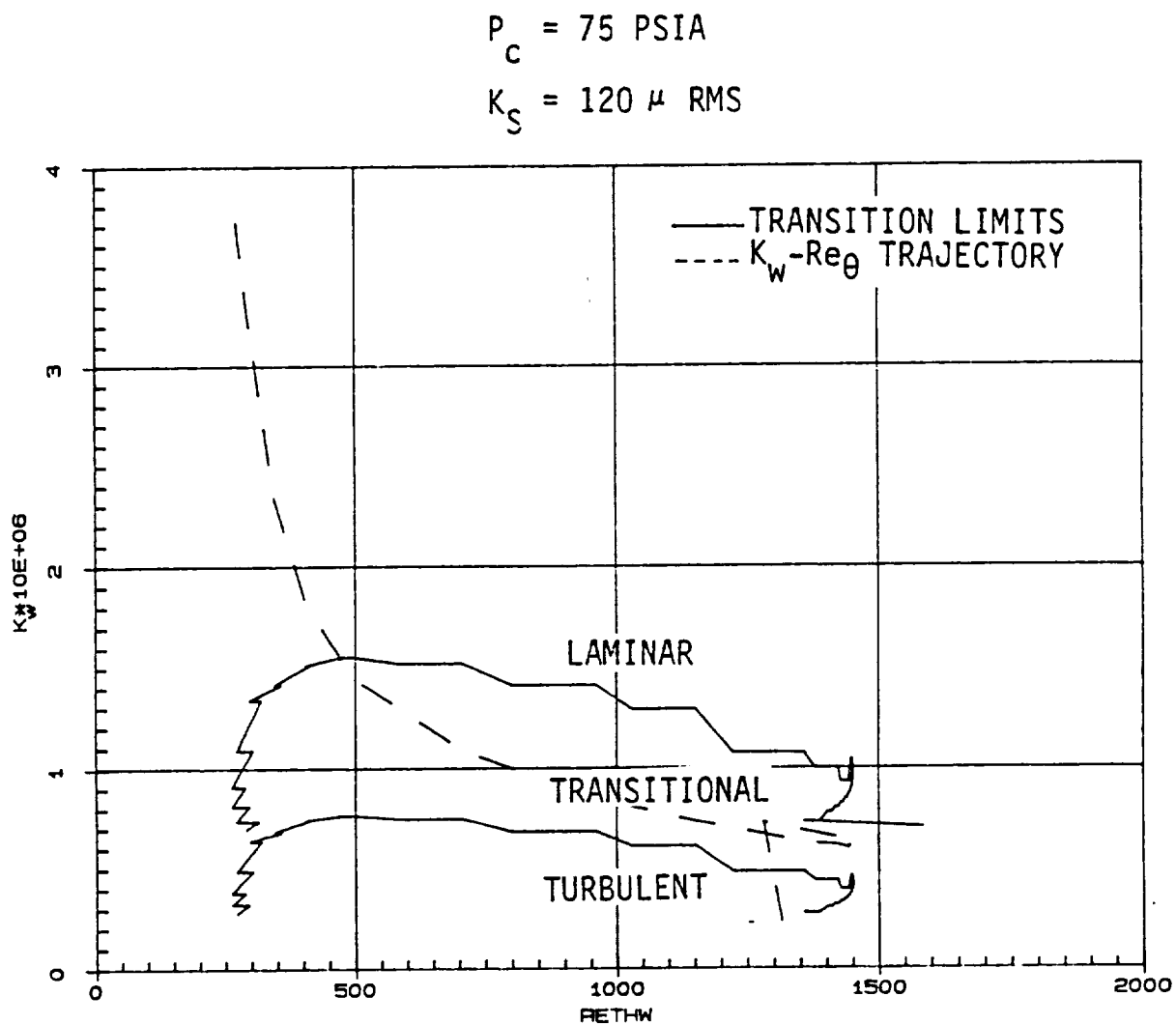
Figure 3.10: Transition Plot of the Case in Fig. 3.8

REMTECH
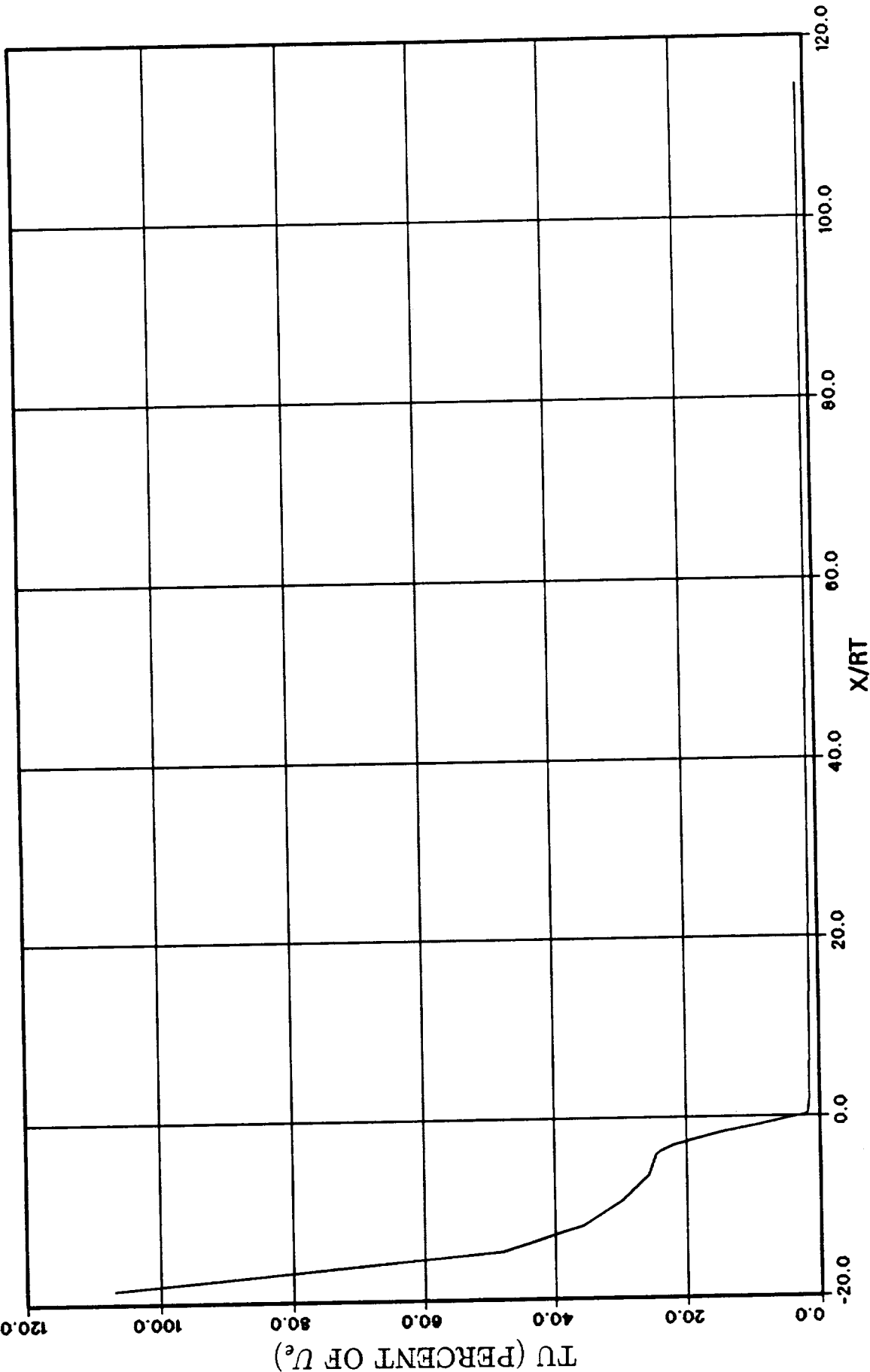
Figure 3.11: Free-stream Turbulence (T_u) Distribution on the OTV Nozzle

X/RT

TU (PERCENT OF U_e)

REMTECH

STATION 6 $(\frac{x}{R_T} = -4.177)$

$DEFINITION: EPSA = \dfrac{\rho^2 \epsilon}{\rho_e \mu_e}$
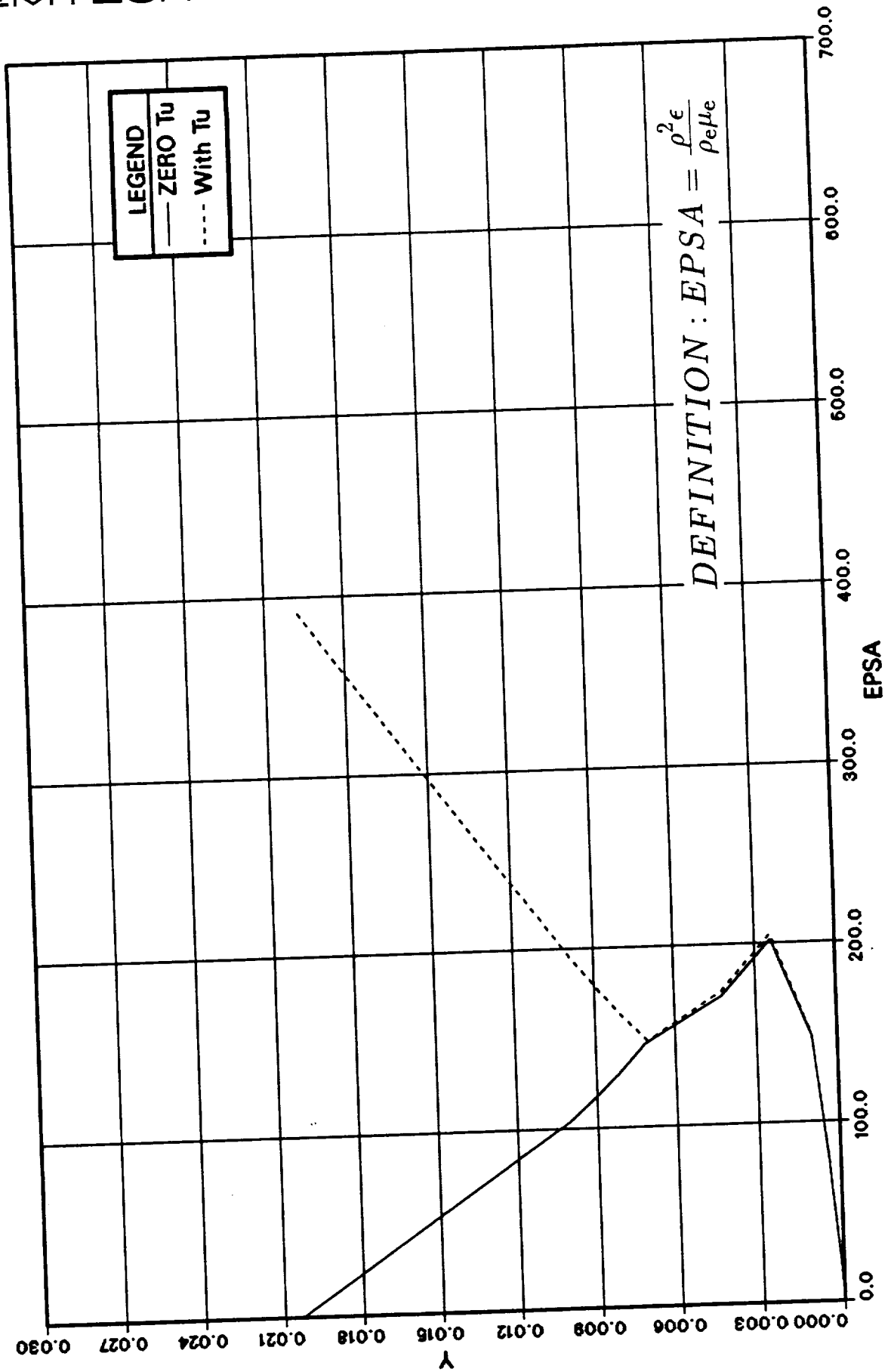
Figure 3.12: EPSA Profile for a Station of the Convergence Section

STATION 12 (THROAT)
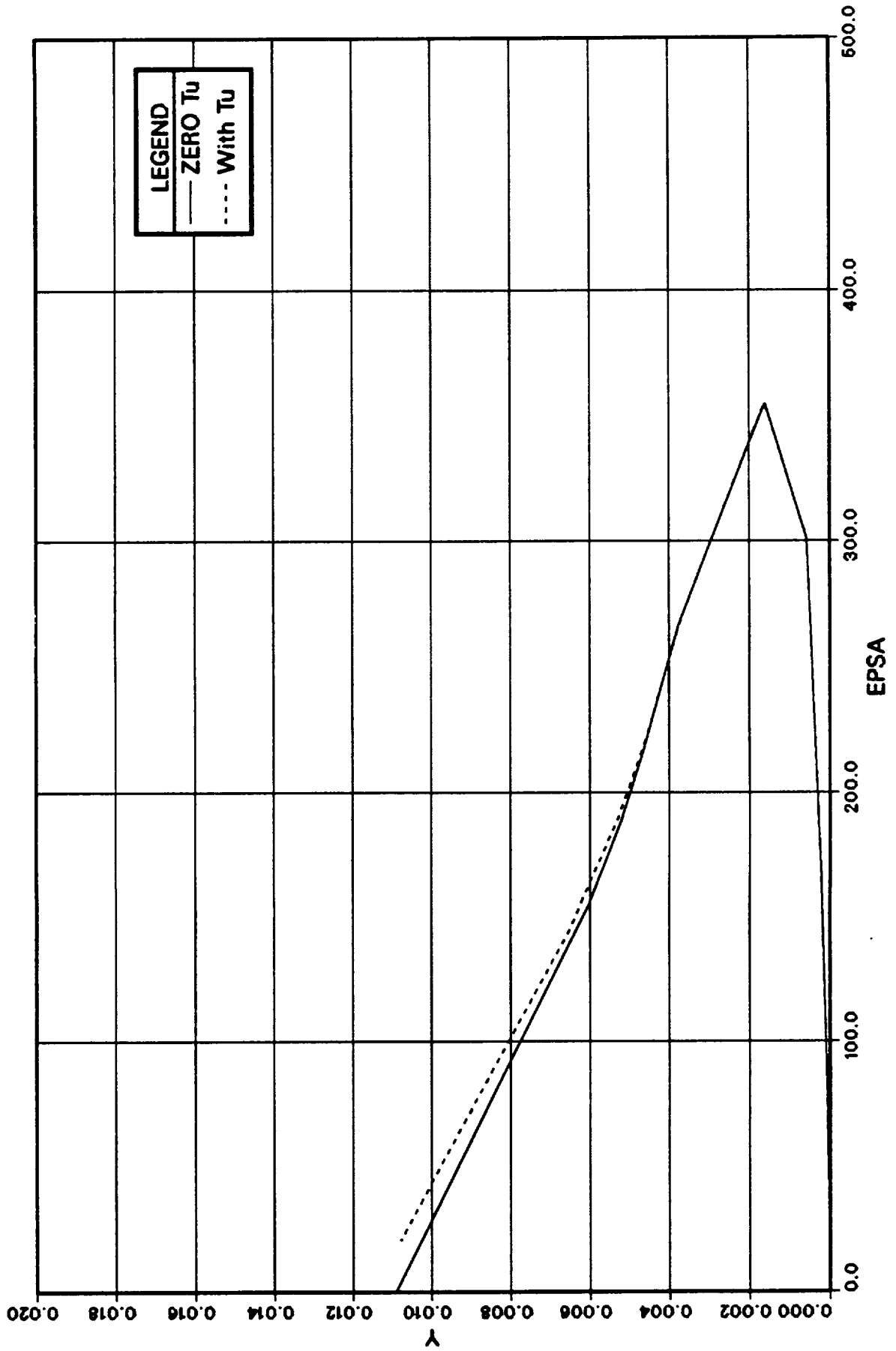
Figure 3.13: EPSA Profile for Throat Station

STATION 20 $\left(\frac{x}{R_T} = 0.293\right)$
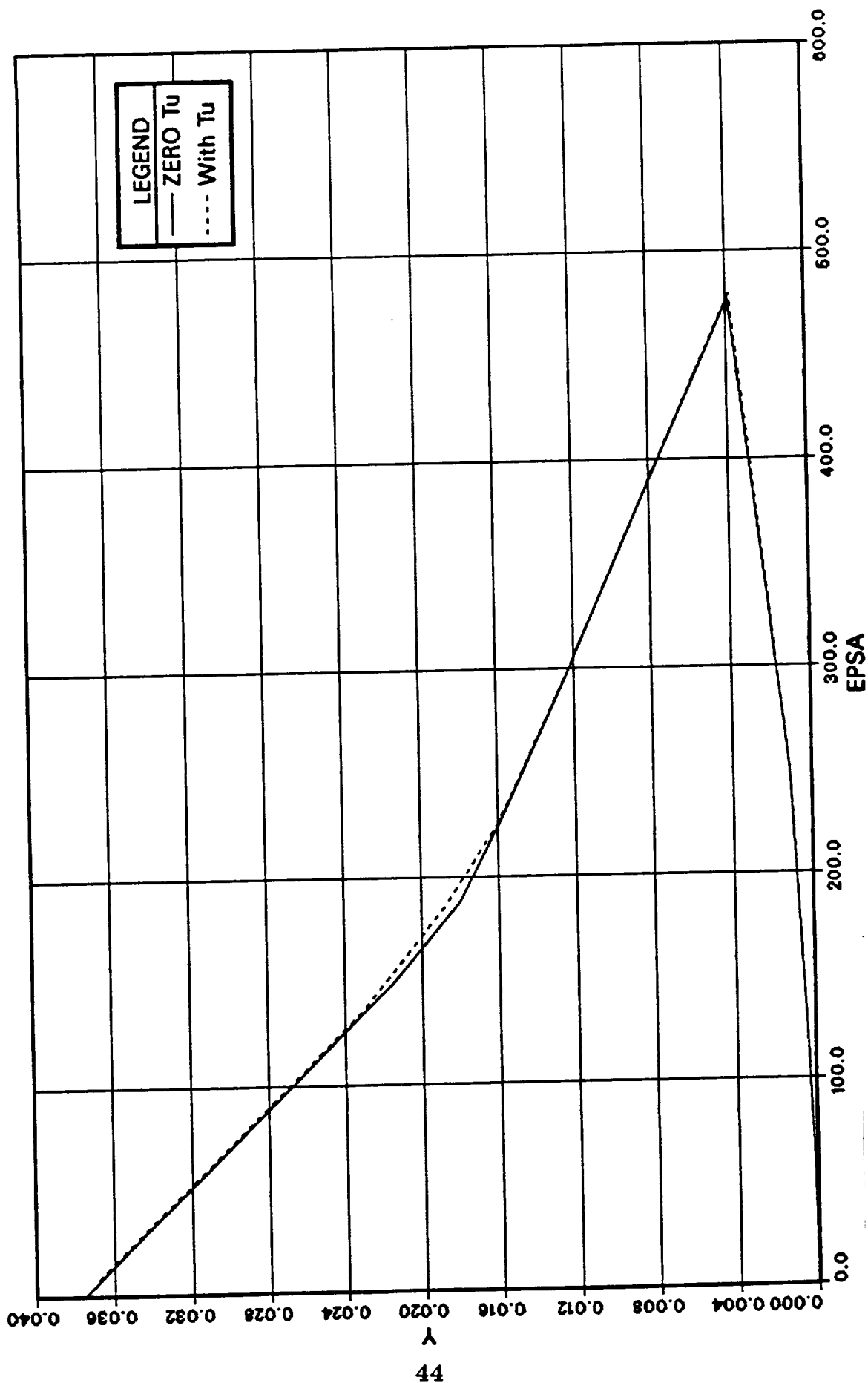
Figure 3.14: EPSA Profile for a Station Downstream of Throat

REMTECH
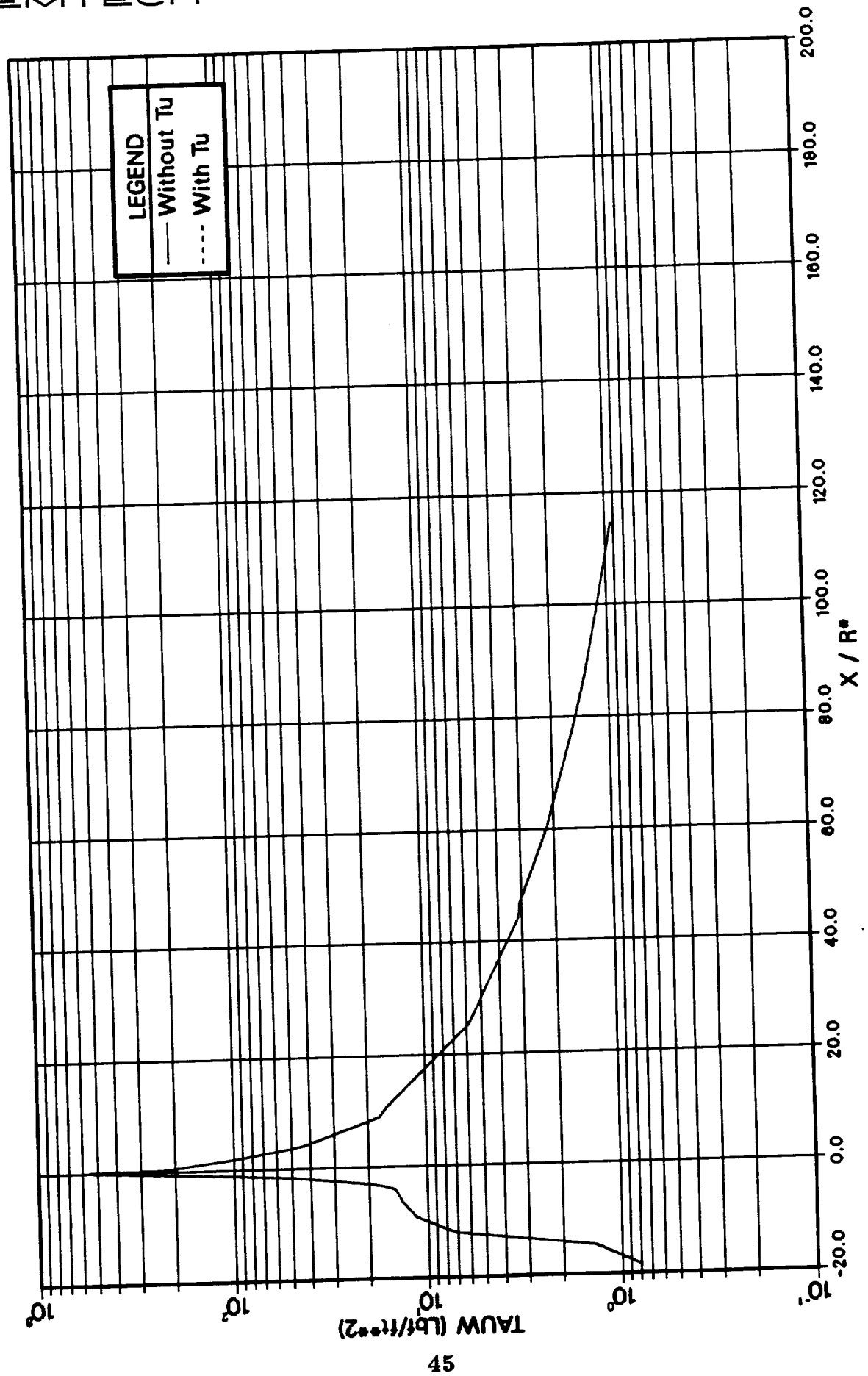
Figure 3.15: Wall Shear Distribution

REMTECH
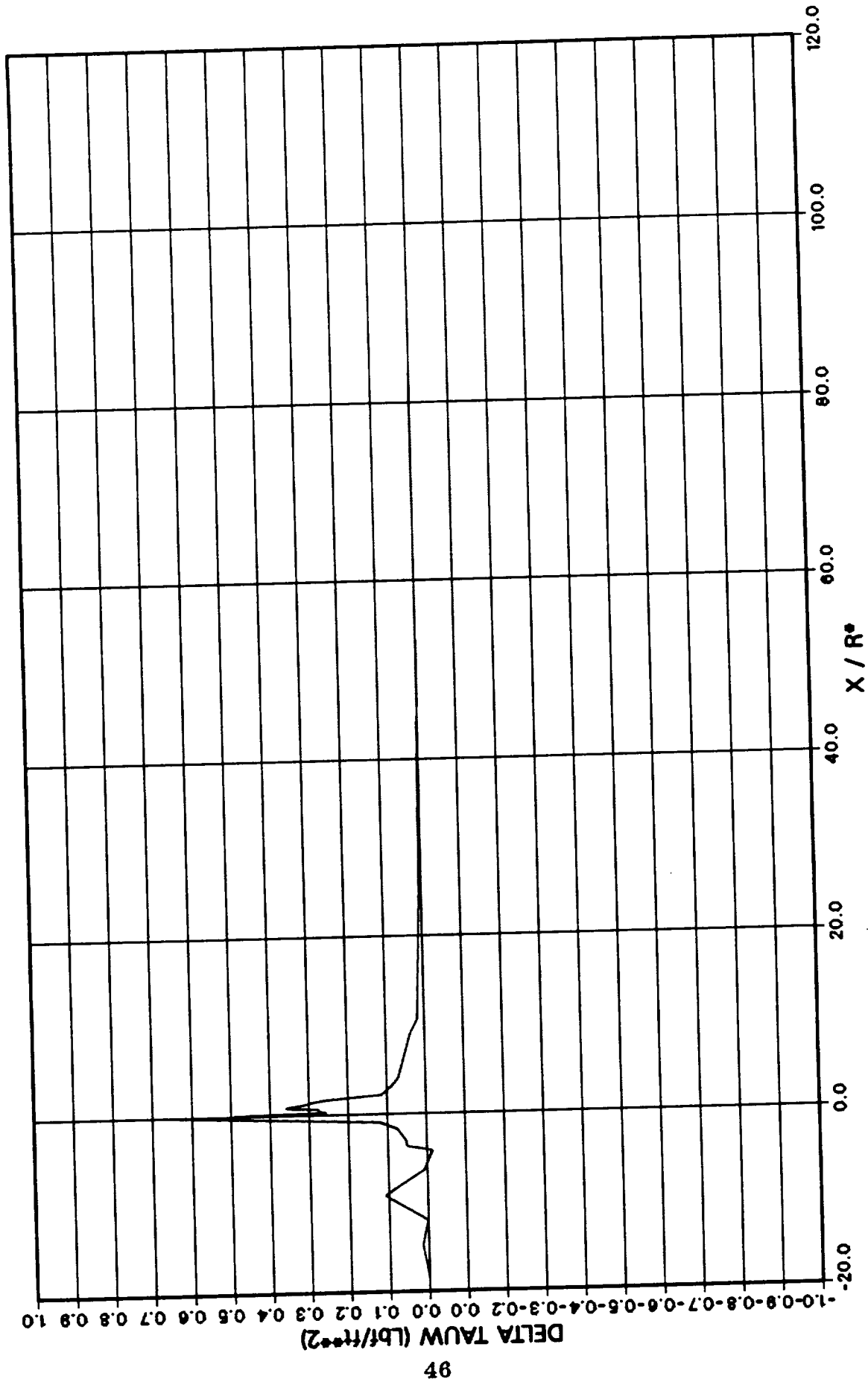
Figure 3.16: Delta TAUW Distribution for Free-stream Turbulence Effects

REMTECH
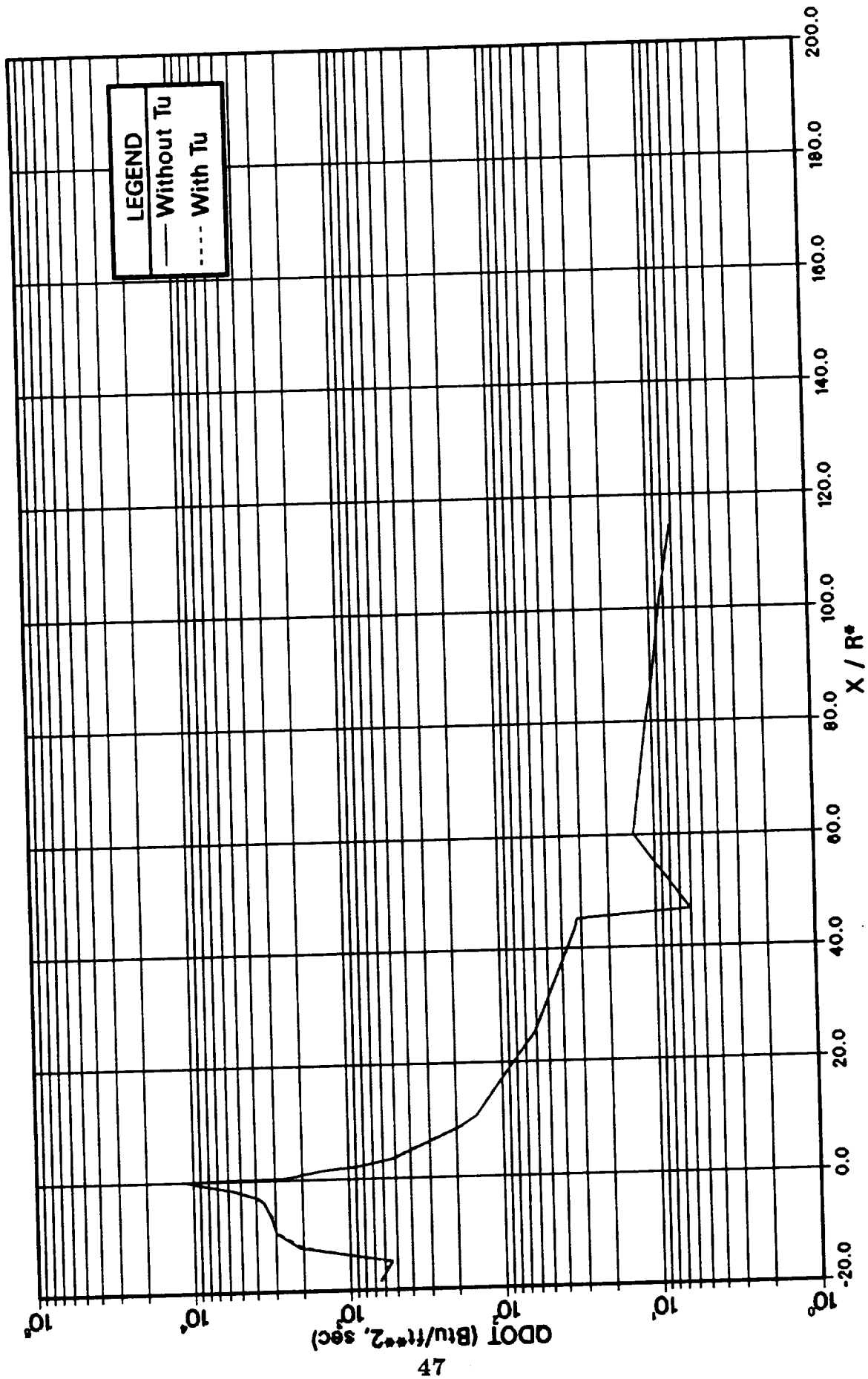
Figure 3.17: Heat Transfer Rate Distribution

REMTECH
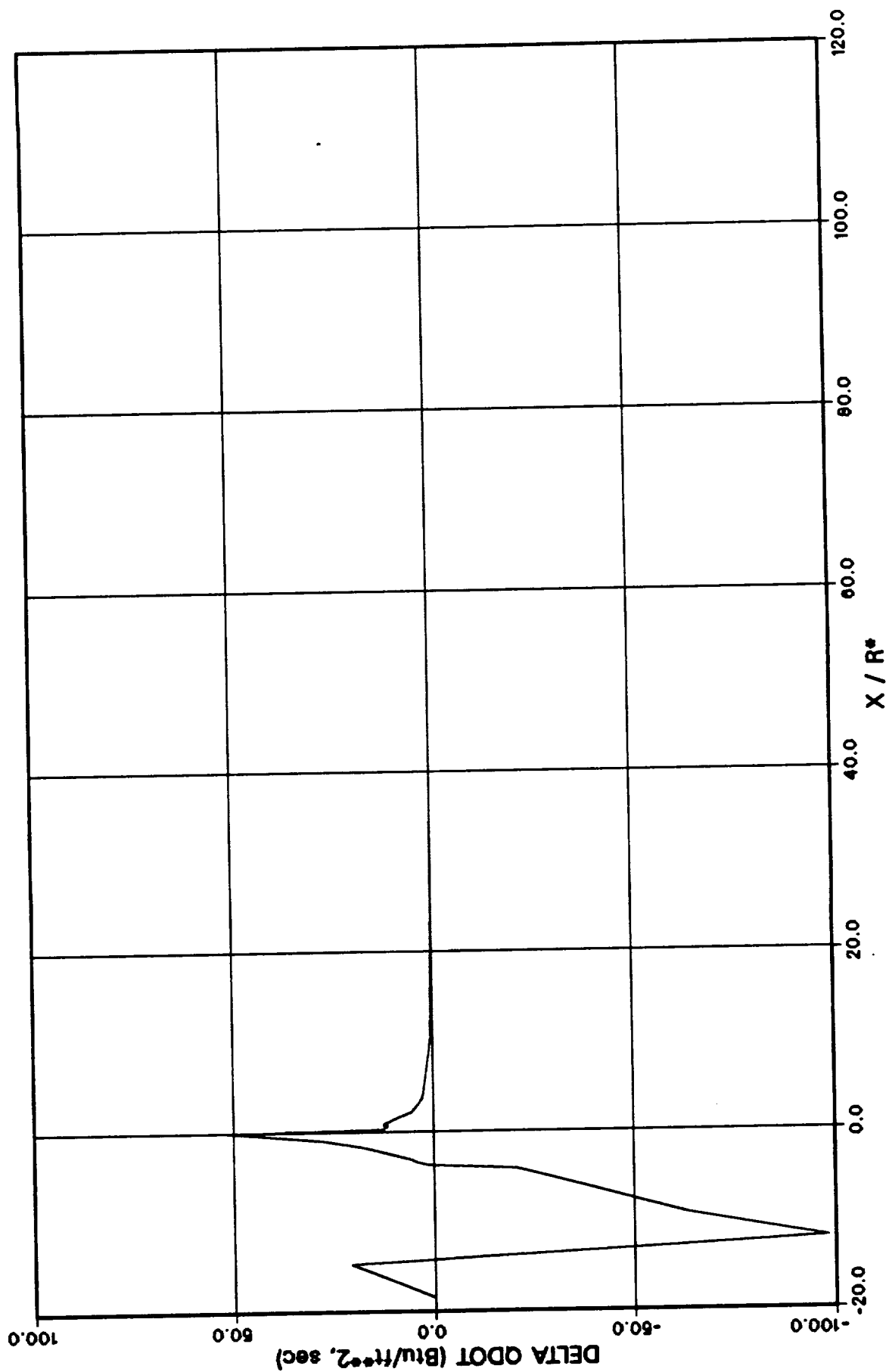
Figure 3.18: Delta QDOT Distribution for Free-stream Turbulence Effects

Section 4

EFFECTS OF CONDENSED PHASE

4.1 Background

The study of the boundary layer flow containing particles is of special interest to the rocket engineer because of the influence of the particles on the wall shear and heat transfer, the possible tendency of particles to collect near the wall and, ultimately, to cause a performance loss in the thrust chamber. Typical data in chemical engineering literature, correlated in terms of voidage, show that there is little effect caused by solid particles until the volume percent of solids reaches about 0.05 percent, and a marked increase occurs in heat transfer for higher solids loading. Correlation of gas-particle heat transfer in terms of solids loading and, sometimes, tube diameter (for pipe flow) is not entirely satisfactory, however, since such correlations ignore the effects of particle size.

Studies of the interaction of walls with a gas-particle turbulent flow have been accomplished by Tien [19], and Soo and Tien [20]. Tien [19] analyzed the increases in heat transfer in the fluid-particle system assuming incompressible, constant property flow with no radiation or velocity layer effects and no effect of the particle on the gas flowfield. In this case, there is no increase in the asymptotic or downstream heat transfer rate, but there is an increase while the flow is developing. Since this is similar to what happens in the expanding flow section in the rocket nozzle, the above results were coded in BLIMPJ [3]. It must be noted here that this formulation is valid up to a solids-to-fluid mass loading ratio of unity. The limited data taken by Farbar and Morley [21] showed that for solids loading ratios greater than unity, heat transfer to the wall increases rapidly. The solids affect both the gas boundary layer and the heat capacity of the flowing mixture. The empirical results derived from this work were also coded in BLIMPJ for rocket nozzle applications. Since small portions of the rocket nozzle contain laminar boundary layer, some of the laminar boundary layer correlations based on momentum integral approach were also coded in the existing version of BLIMPJ. All the above formulations were used as a separate module which is called at will by specifying the appropriate flag in the name-list input.

Since the OTV nozzles will be designed to operate at very low ambient pressures and flow will expand very rapidly in the nozzle, there is every likelihood of forming a

two-phase fluid cntaining liquid droplets and ice particles in the nozzle. Depending on the size of the particles, a fraction of the smaller sized particles will flow in the boundary layer, whereas most of the larger sized particles will flow in the axial region. It is also very likely that the particle sizes will vary along the wall in the boundary layer, as the flow expands down the nozzle. How the particle loading will affect the skin-friction and heat transfer characteristics at the wall is the subject to be investigated in this task.

The H_2-O_2 propellant system which will be used in the projected OTV engines could produce ice particles in the expansion section of the nozzle. Since these nozzles will have high area ratios, the expansion process will cool the gas which is mostly water vapor and the static temperature will be low enough to freeze the vapor and form ice particles. More and more ice particles will form as the gas flows through the expanding nozzle. It has been found from studies on these high area ratio nozzles, which are regeneratively cooled for part of the nozzle and radiation-cooled for the last portion of the nozzle, that heat transfer drops off drastically downstream of the throat and is almost negligible a moderate distance aft of the throat. So, the formation of water droplets and ice particles occurring in this part of the nozzle might not greatly impact the magnitude of heat transfer and skin friction. However, the presence of particles in the boundary layer would change the displacement and momentum thicknesses and, in turn, would alter the boundary layer losses in the performance of the thrust chamber.

It must be noted here that the effects of particles in nozzle boundary layers have not been treated extensively in the literature. The kind of work that exists usually refers to pipe flow problems. The "history" effects of the particles in boundary layer are very scarcely treated. As a consequence, only engineering approaches were implemented in the BLIMPJ update work in Ref. [3], where no modifications were made to the turbulence model.

If the loading of condensed phase changes as the flow expands in the nozzle, the laminar boundary layer formulation would be affected only by the species concentration effect. If the flow is turbulent, the formulation given for the turbulent boundary layer should be used. This formulation, derived from empirical considerations, depends on the condensed phase loading and should be used to yield skin friction and heat transfer quantities at the nozzle wall. The practical specification of this loading is not necessarily straightforward. It is difficult enough to produce a certain size particle and a certain loading externally with the help of a particle generator and supplying it to the nozzle flow. It is much more difficult a matter to be able to quantify the solids loading in various areas of the nozzle including the boundary layer. In the case of the high area ratio nozzle, where these condensed phases would appear in varying loading, theoretical and experimental

REMTECH

methods must be devised to quantify the loading, and the empirical and analytical approaches suggested below should be used to effectively quantify boundary layer losses.

4.2 Turbulence Model Representation for Condensed Phase Loading

Soo and Tien [20] considered particle motion in a turbulent fluid stream with emphasis on the effect of wall interference. The intensity of the particle motion was found to always be less than the intensity of the fluid motion and is reduced further by the wall interference effects. However, with respect to the core or mainstream intensities, the particle motion near the wall can have a high intensity because of the corresponding high local intensity of fluid motion near the wall.

Heat transfer will be affected at the wall because of the following two significant effects due to the presence of particles in the boundary layer.

1. The eddy viscosity in the boundary layer is expected to fall below its clean flow value because of particle loading in the boundary layer.

2. The specific heat of the two-phase flow will be modified because of the loading, resulting in a change in heat transfer to the wall.

For small particles, it has been shown by Soo and Tien [20] that the particle diffusivity is of a similar order as the eddy diffusivity of the stream. Thus, the turbulence model needs no modification. However, the particle loading effect which was considered by Tien [19], and Farbar and Morley [21] has been reported by Praharaj [3].

A review of the literature on the fluid dynamics of solid particles in multi-phase systems showed different and incomplete approaches to the problem of the motion of various size particles near the wall of a turbulent fluid. In the work of Soo [22] a specific expression for the ratio of particle diffusivity to eddy viscosity was found as a function of particle diameter, density, Reynolds Number (based on fluid stream turbulent intensity) and turbulence microscales. This expression is based on the analysis of the "probability of encounter for finite-size particles." The final steps for calculating the ratio of diffusivities are summarized below for completeness.

Assuming that the Reynolds Number based on relative velocity between the particle and its surrounding fluid is small enough so that particle drag is given by Stokes' Law, the particle diffusivity, D_p, can be defined by the equation:

$$D_p = \lim_{t \to \infty} \frac{1}{2t} E\left\{y^2(t)\right\} \tag{4.1}$$

where $E\left\{y^2(t)\right\}$ is the mean square particle displacement and is given by the following equation:

$$\lim_{t \to \infty} E\left\{y^2(t)\right\} = 2t\lambda^* < u'^2 > - \frac{2 < u'^2 >^{1/2}}{\lambda_E^2} t \frac{\lambda^{*2}}{F}\left(\frac{6}{F\lambda^* + 1}\right) + O\left(\frac{1}{\lambda_E^4}\right) \tag{4.2}$$

where $< u'^2 >^{1/2}$ is the intensity of fluid stream turbulence,

$$\lambda^* = \lambda_L / < u'^2 >^{1/2} , \tag{4.3}$$

$$F = 6\pi r_p \mu / m_p , \tag{4.4}$$

and λ_L and λ_E are the Lagrangian and Eulerian microscales of stream turbulence, respectively. Thus,

$$D_p = < u'^2 > \lambda^* \left\{1 - \frac{\lambda^{*2} < u'^2 >}{\lambda_E^2} \frac{1}{F\lambda^*}\left(\frac{6}{F\lambda^* + 1}\right)\right\} \tag{4.5}$$

The fluid diffusivity (eddy diffusivity) obtained from the Taylor formula, using the Lagrangian correlation coefficient, is

$$D_f = \lambda^* < u'^2 > = \lambda_L < u'^2 >^{1/2} \tag{4.6}$$

Then, the ratio of particle diffusivity to eddy diffusivity may be written as,

$$\frac{D_p}{D_f} = 1 - \frac{\lambda^{*2} < u'^2 >}{\lambda_E^2} \frac{1}{F\lambda^*}\left(\frac{6}{F\lambda^* + 1}\right) + O\left(\frac{1}{\lambda_E^4}\right) \tag{4.7}$$

Introducing the impulse response parameter I,

$$I = \frac{2}{F\lambda^*} \tag{4.8}$$

The parameter I is defined as the ratio of particle impulse response time to the time a fluid particle remains in a velocity correlated region. For spherical particles, this parameter can be written as,

$$I = \left(\sqrt{\pi} \,/\, 18\right) < N_{Re} > \left(\rho_p \,/\, \rho_f\right) \left(^{2r_p} \,/\, \lambda_L\right) \tag{4.9}$$

where

$$< N_{Re} > = \left(^{2r_p} \,/\, \nu\right) < u'^2 >^{1/2} \tag{4.10}$$

is the particle Reynolds Number. Upon substitution of Equations 4.3 and 4.8 into Equation 4.7, the ratio of particle diffusivity to eddy diffusivity becomes,

$$\frac{D_p}{D_f} = 1 - \frac{\lambda_L^2}{\lambda_E^2} \left(\frac{3I^2}{I+2}\right) + O\left(\frac{1}{\lambda_E^4}\right) \tag{4.11}$$

Within the context of the BLIMPJ algorithm using the algebraic eddy viscosity models, the following simplifications and assumptions were made.

From Soo [22], λ_E was considered to be the radius of a pipe containing the two-phase flow. In our case, λ_E was assumed to be equal to the local boundary layer height, δ. Since the turbulence intensity is not calculated in BLIMPJ as it is done with a $k - \epsilon$ turbulence model, certain simplifications had to be made. The eddy contribution to the shear stress is

$$-\rho \,\overline{u' v'} = \tau - \mu \frac{du}{dy} \tag{4.12}$$

From Schlichting's book, the shear stress is related to the turbulence intensity by a correlation coefficient, ψ, given by

$$\psi = \overline{u' v'} \,/\, \overline{u'^2} \tag{4.13}$$

From a limited set of data, ψ was approximated to be -0.45. Then, from Eqns. 4.12 and 4.13,

$$\left(\overline{u'^2}\right)^{1/2} = \left[\epsilon \,\tau \,/\, 0.45(\mu + \rho\,\epsilon)\right]^{1/2} \tag{4.14}$$

where ϵ is the kinematic eddy viscosity. Since the problem usually is to obtain the ratio in Eq. 4.11 for a given particle loading, it is essential to obtain an equivalent size spherical particle at a given point in the boundary layer. Particle loading is given by

$$\frac{W_p}{W_f} = \frac{\rho_p \, n_p \, v_p}{\rho_f} \tag{4.15}$$

Particle mass flow rate in an elemental ring located at radius, r, of width, Δy,

$$= (2\pi r)\,(\Delta y)\,(\rho_{\text{mix}})\,(MF_p)\,,\ \frac{\text{lbm}}{\text{ft}} \qquad (4.16)$$

This is also equivalent to the width of the particle phase ring, $\bar{a}$, which

$$= (2\pi r)\,(\bar{a})\,(\rho_p)\,,\ \frac{\text{lbm}}{\text{ft}} \qquad (4.17)$$

From Eqns. 4.16 and 4.17,

$$\bar{a} = n_p\,V_p\,\Delta y \qquad (4.18)$$

This formulation must be considered approximate since, clearly, $\bar{a}$ is not the radius of an equivalent sphere. A more detailed analysis is necessary for computing the diffusivity ratio in such a situation.

The significance of various terms in Eq. 4.11 is dealt with in Ref. [22]. For a fixed λ_L/λ_E and small particle impulse response, I, a solid particle "follows" the fluid motion perfectly, and its diffusivity is equal to the fluid diffusivity. However, for a fixed λ_L/λ_E, a solid particle with large I does not respond to the fluid motion; it tends to remain stationary and not diffuse.

In order to correlate the diffusivity ratio with the eddy viscosity, one can assume constant turbulent Schmidt Number. Consequently,

$$Sc = \left(\frac{\epsilon}{\epsilon_D}\right)_p = \frac{\epsilon}{\epsilon_D} \qquad (4.19)$$

or,

$$\frac{\epsilon_p}{\epsilon} = \frac{\epsilon_{D_p}}{\epsilon_D} \qquad (4.20)$$

This was coded in a subroutine called PARTCL2 and integrated in BLIMPJ.

4.3   Concept Checkout

In order to check out the turbulence model coded for the presence of particles in the boundary layer, the OTV nozzle configuration (Fig. 4.1) was chosen. As an example, Aluminum was chosen to be the particle material present in the boundary

layer. The particle loading (PLOADING) was chosen to be $W_p/W_f = 0.5$ in the whole boundary layer and BLIMPJ was run by turning on the particle option, IPART=2. (The particle option, IPART=1, uses an engineering approach [3].) As discussed in Sec. 4.1, the major effects of the particle presence in the boundary layer are due to the species composition and the damping effects. In order to examine the former effect, TKP(3,J) in the input was chosen to be 0.3333, which is equivalent to $W_p/W_f = 0.5$, and IPART was set to zero in order not to call any of the two particle subroutines corresponding to IPART=1 and 2. Then, in addition to the input above, a separate run was made with IPART=2. The boundary layer thicknesses for these runs including a clean flow run are plotted in Fig. 4.2. The Al content in the boundary layer alone reduces the boundary layer height because of a reduction of total enthalpy of the system. The damping effects of particles in the fluid further reduce the boundary layer height because of a reduction in turbulence intensity. Figures 4.3 through 4.5 show kinematic eddy viscosity profiles at Stations 12, 41 and 48 (marked in Fig. 4.1). At the throat (Station 12), EPSA is reduced almost down to zero, thus making the boundary layer almost laminar. However, at stations 41 and 48, the boundary layer heights are seen to be lower than the clean-flow values, but EPSA values are higher in the inner layer. These EPSA values, however, are lower than those for the specie composition effects alone. Profiles of the particle diffusivity ratios at these stations are plotted in Fig. 4.6, where, again, the effects are maximum at the throat. The shear profiles for these stations are given in Figs. 4.7 through 4.9, where reductions of shear are observed across the boundary layer. Even though EPSA values are somewhat higher in the inner layer. These EPSA values, however, are lower than those for the mixture effects alone. Profiles of the particle diffusivity ratios at these stations are plotted in Fig. 4.6, where, again, the effects are maximum at the throat. The shear profiles for these stations are given in Figs. 4.7 through 4.9, where reductions of shear are observed across the boundary layer. Even though EPSA values are somewhat higher in the inner layer for Stations 41 and 48, the thinning of the velocity profiles causes the velocity gradients to be lower at a higher rate than the increase in eddy viscosity, thus resulting in lower shear values. Figure 4.10 gives the wall shear distribution for no particles, the species mixture effect and the total effect including damping. The curves are so close to each other in the scale given in this figure, a separate plot was made in Fig. 4.11 to show the ΔT_W between the no particles and the total effect cases, where maximum reduction is seen to occur at the nozzle throat. Similar comparisons were made for heat transfer rate in Figs. 4.12 and 4.13, where, again, the maximum delta occurs at the nozzle throat.

In order to check the new particle option against any available data or any available formulation, the previously coded particle option as chosen and was run for a loading of 0.5. The comparisons of these two options are shown in Figs. 4.14

REMTECH

and 4.15. The comparison is only approximate. More credibility, however, should be placed on the "IPART=2" option, since it considers all the effects such as mixture, damping and "history" effects. In contrast, the "IPART=1" option assumes constant property flow in the boundary layer, does not consider damping effects and does only "point" calculations.

REMTECH
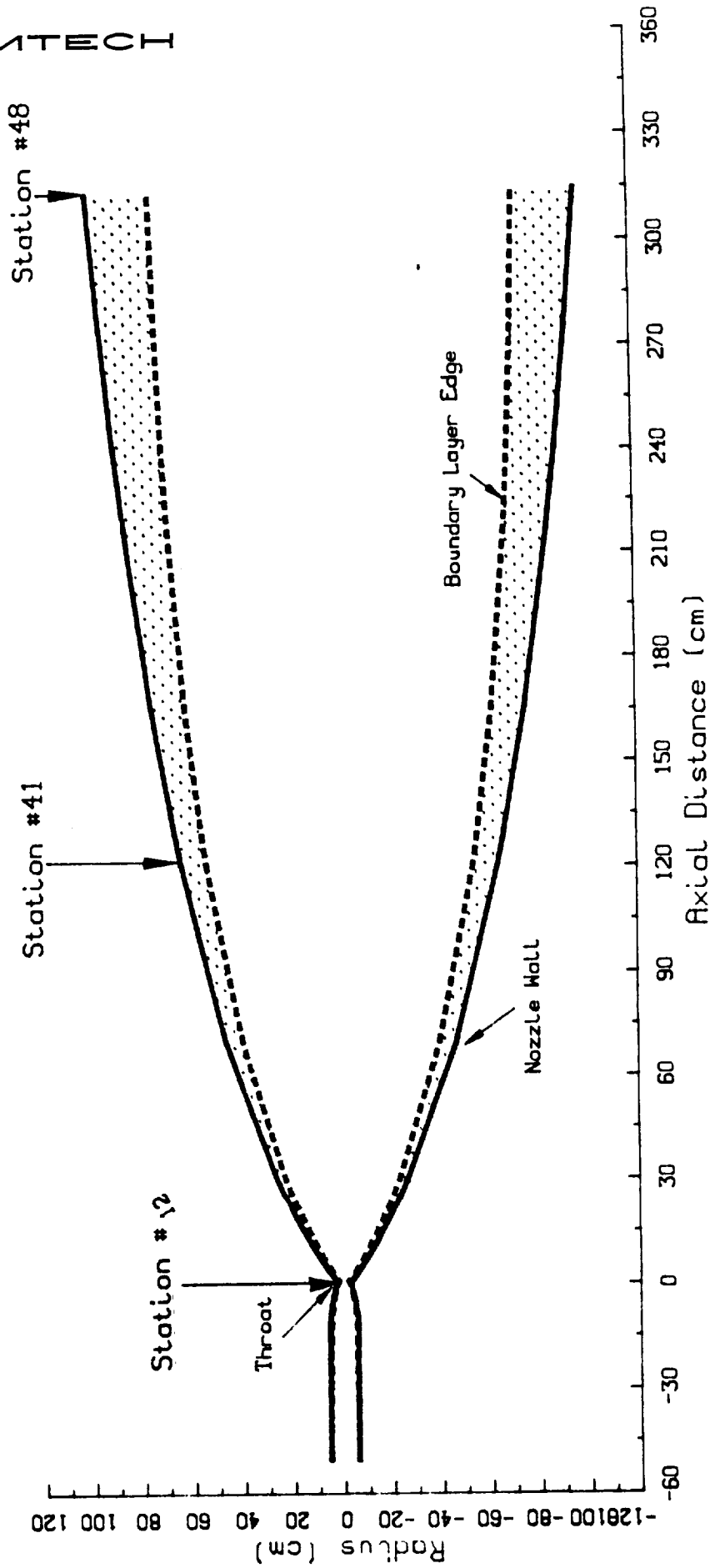
Figure 4.1: OTV Nozzle Configuration and Turbulent Boundary Layer Thickness. (The selected stations are also shown for the Condensed Phase Study.)

REMTECH

OTV NOZZLE
LOADING = 0.5

LEGEND
— No Particles
- - - Specie Composition Effect
······· Total Effect
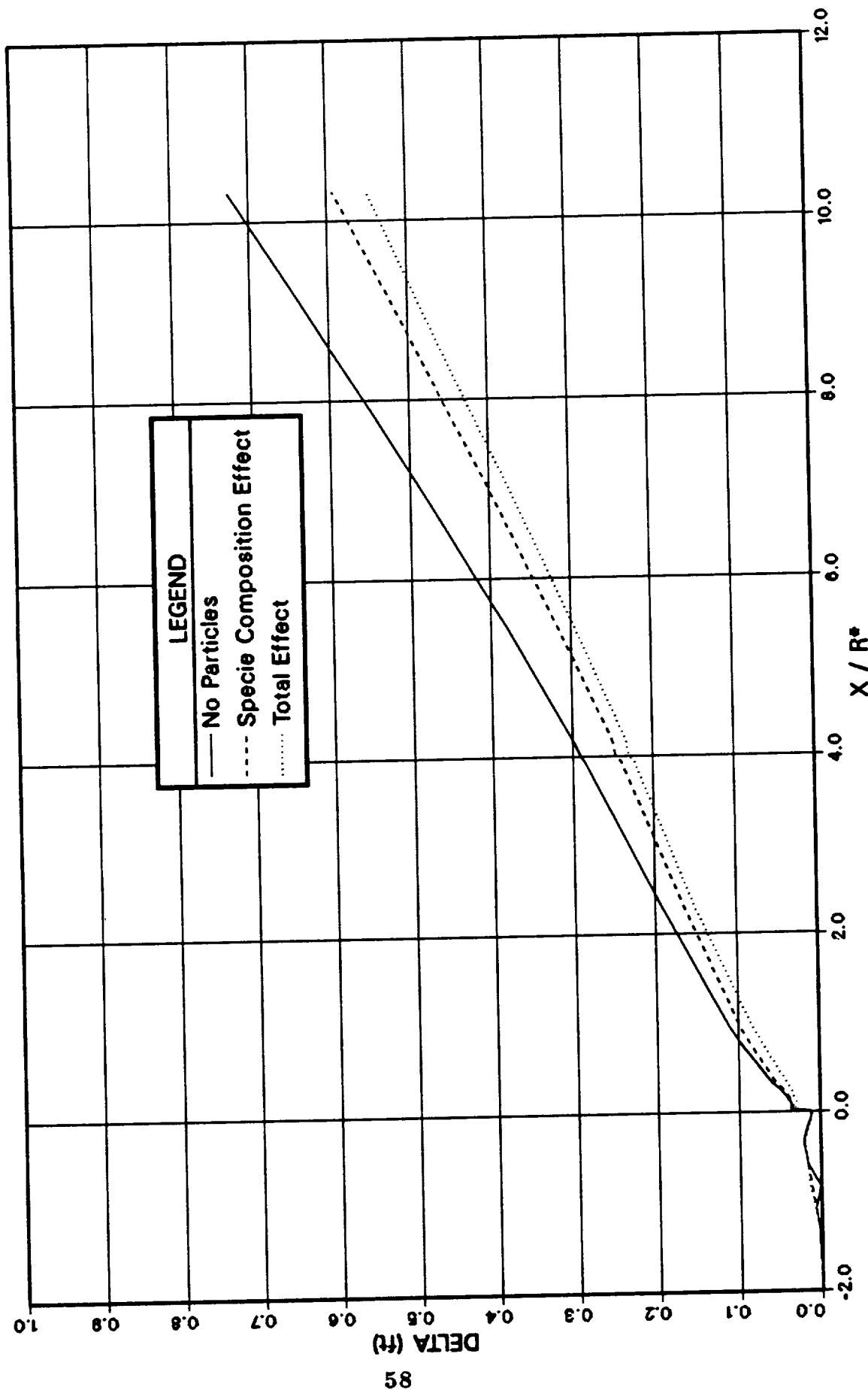
Figure 4.2: Effects of Specie Composition Effect and Particle Damping Effects on Boundary Layer Size

58

REMTECH
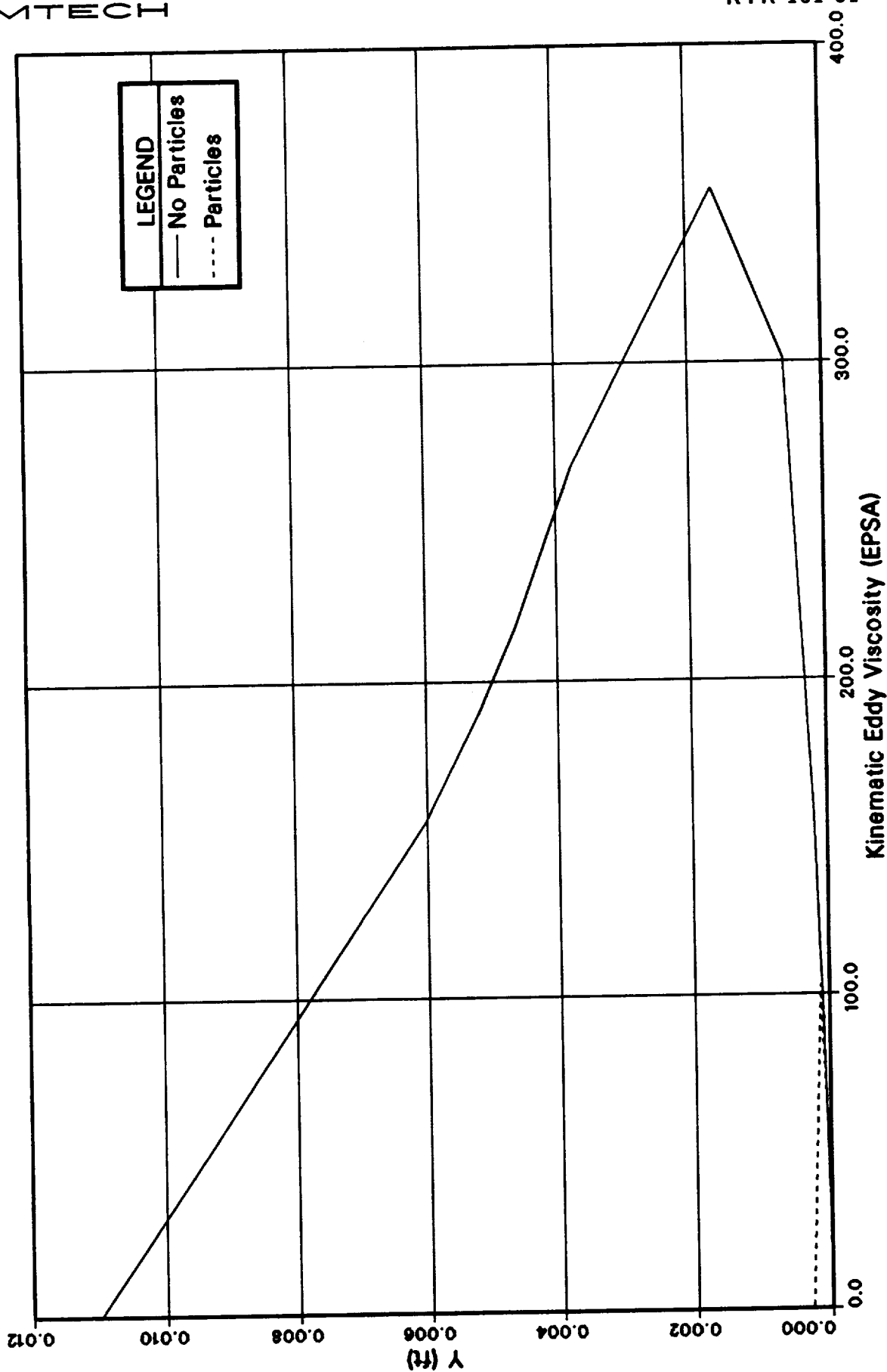
Station 12

Figure 4.3: Profiles of EPSA With and Without Particle Loading at the Throat

REMTECH
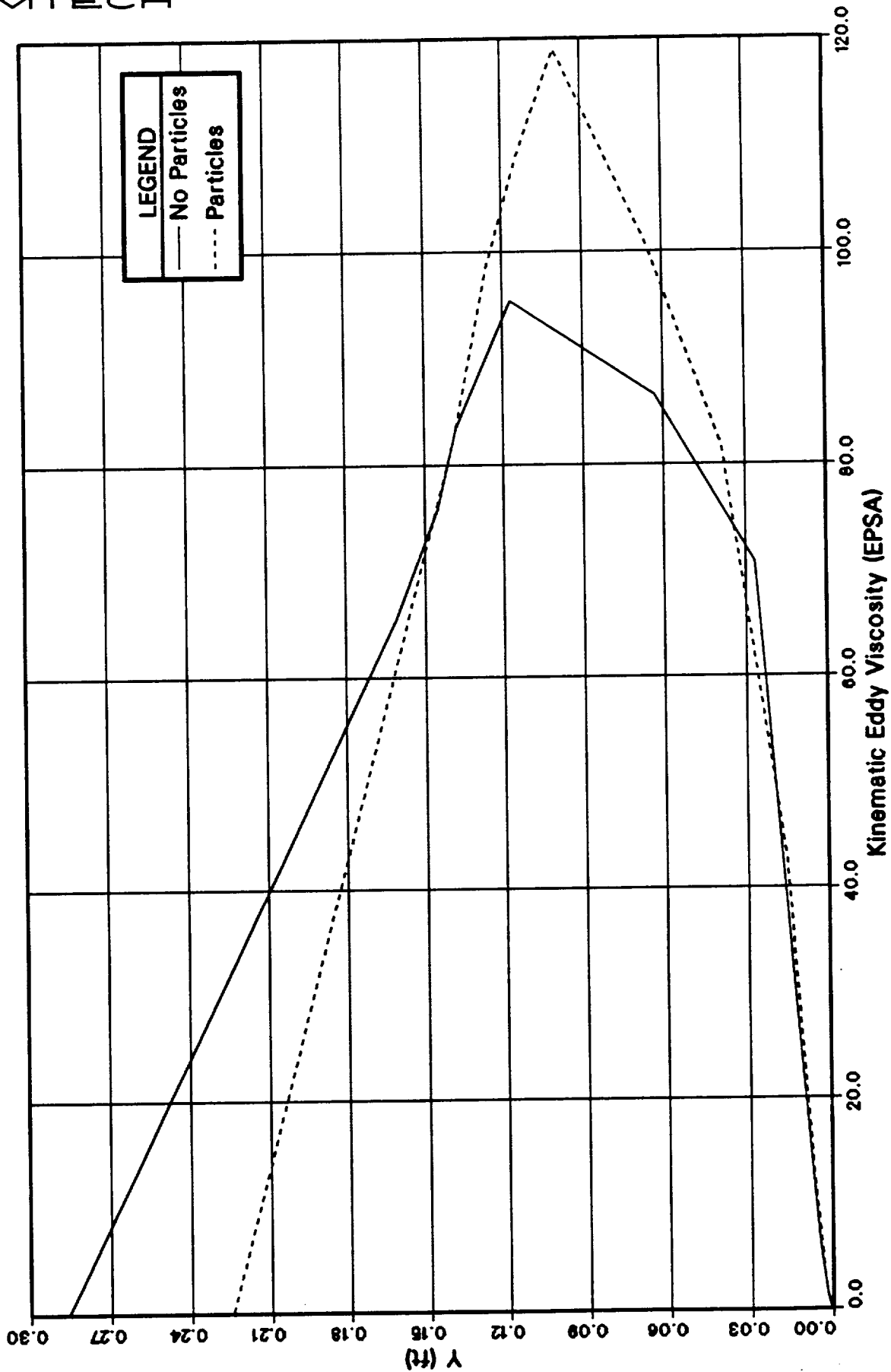
Station 41

Figure 4.4: Profiles of EPSA with and without Particle Loading Downstream of the Throat

REMTECH

Station 48

Figure 4.5: Profiles of EPSA With and Without Particle Loading at the Exit

61
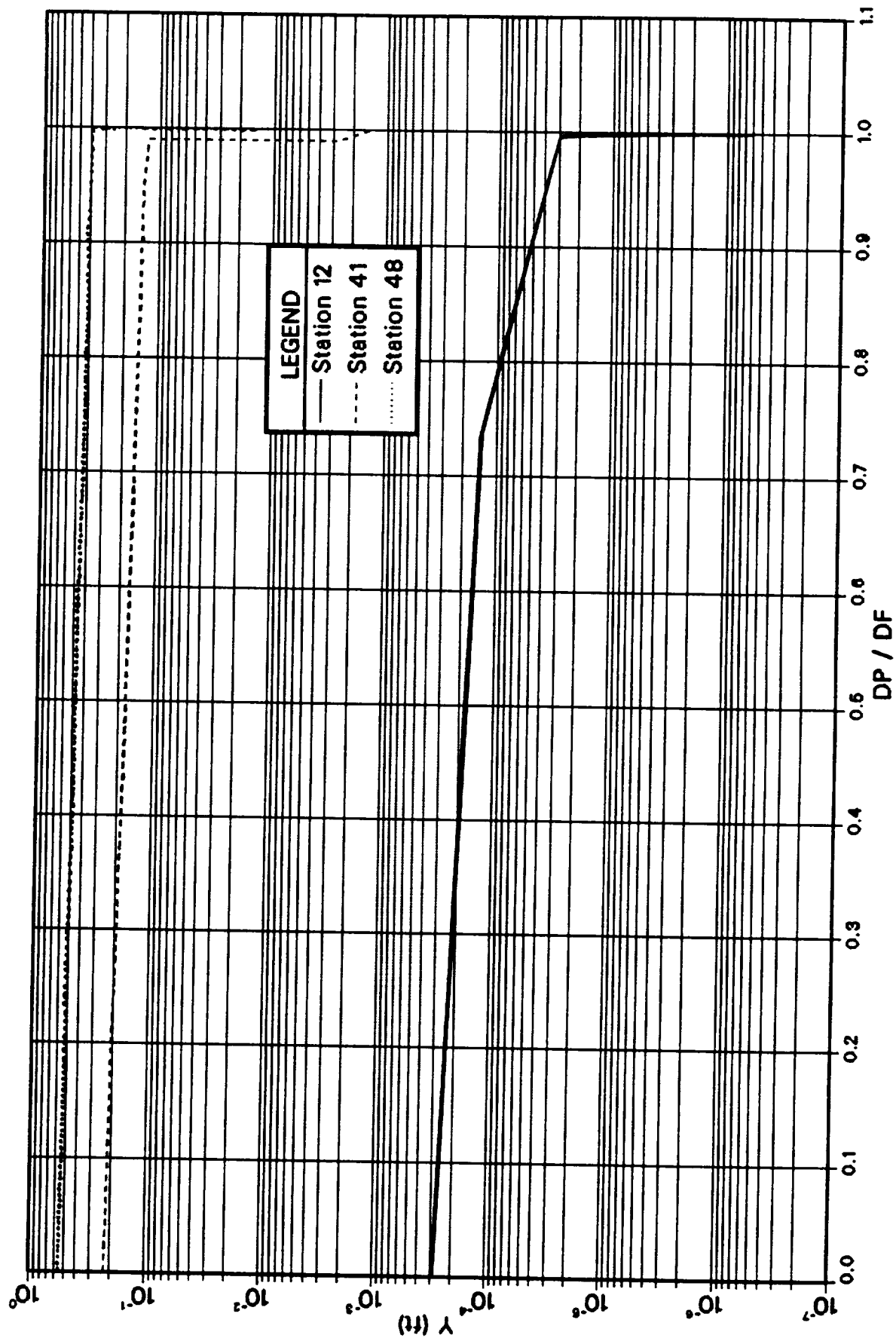
Figure 4.6: Profiles of Eddy Diffusivity Ratio with Particle Loading at the Three Stations

REMTECH
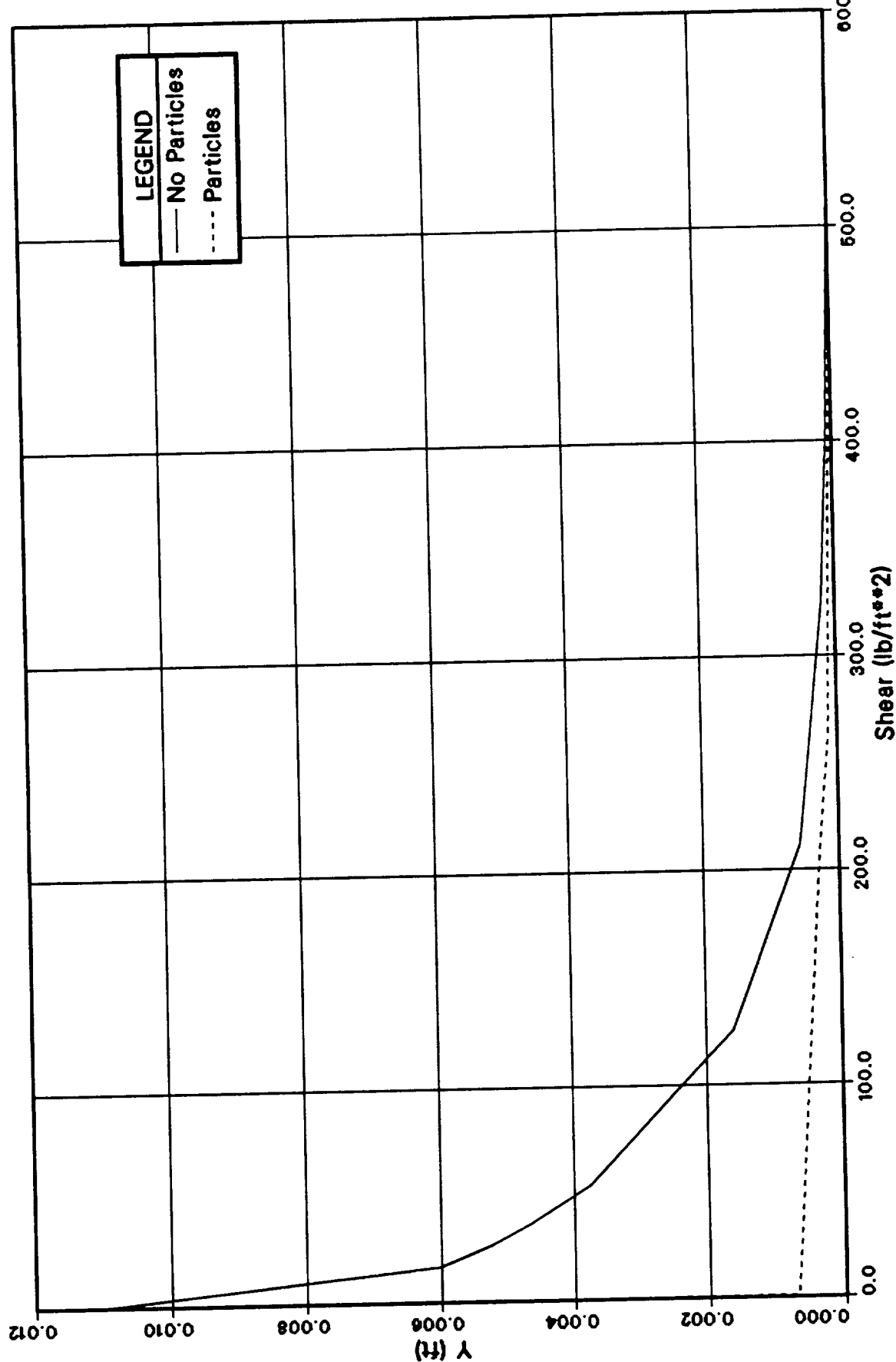
Station 12

Figure 4.7: Profiles of Shear With and Without Particle Loading at the Throat

Station 41
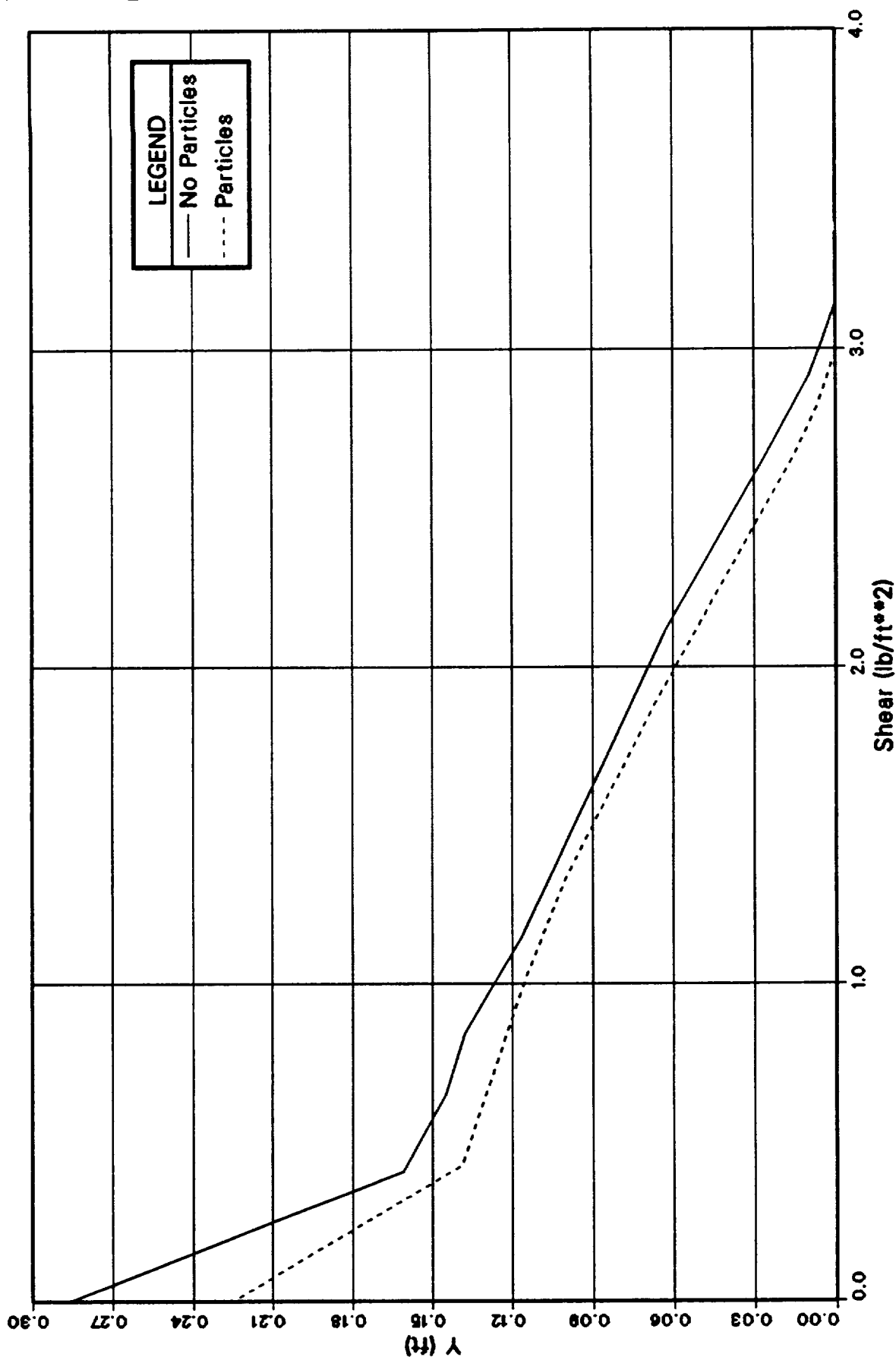
Figure 4.8: Profiles of Shear With and Without Particle Loading Downstream of the Throat

Station 48
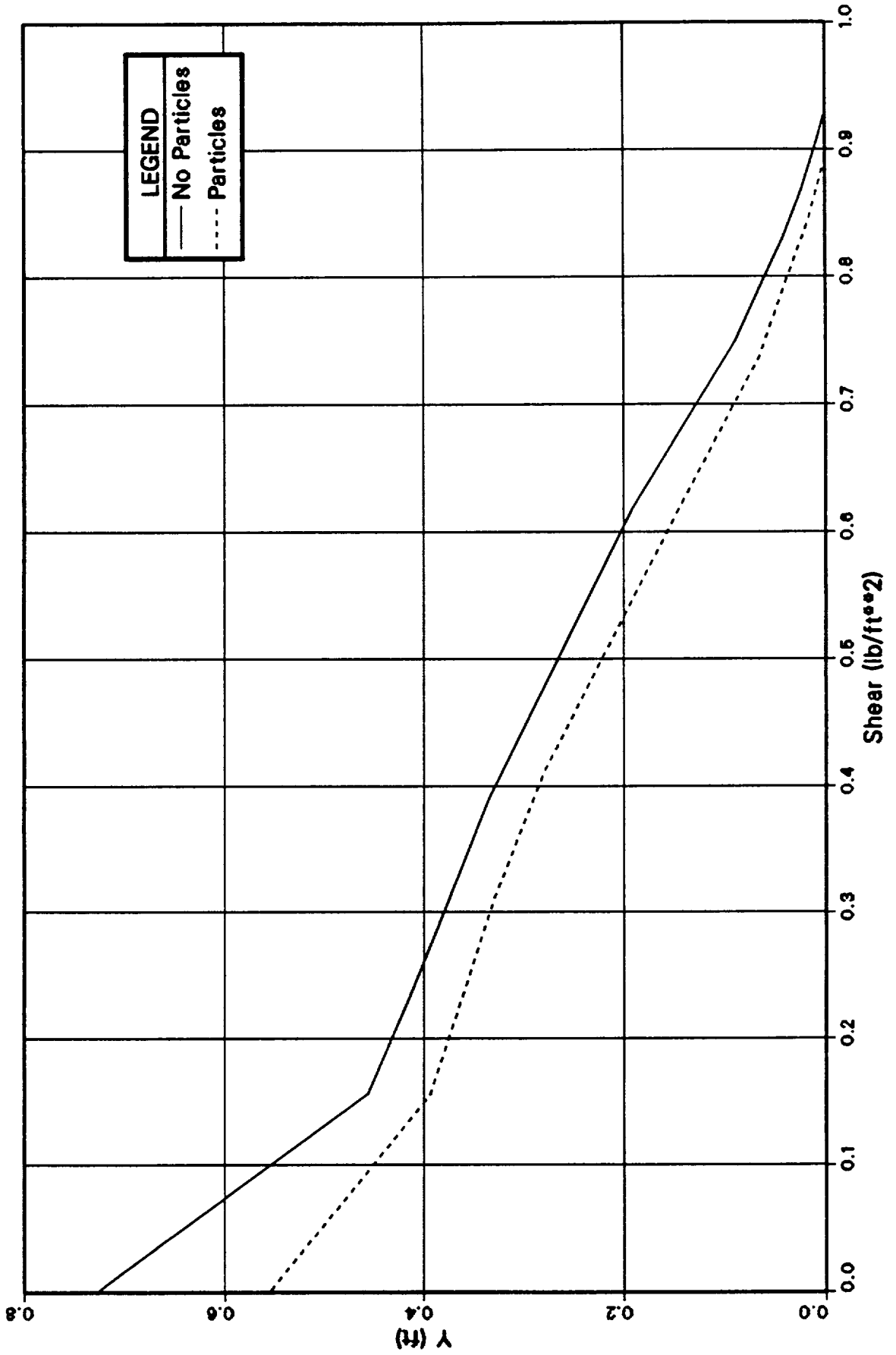
Figure 4.9: Profiles of Shear With and Without Particle Loading at the Exit
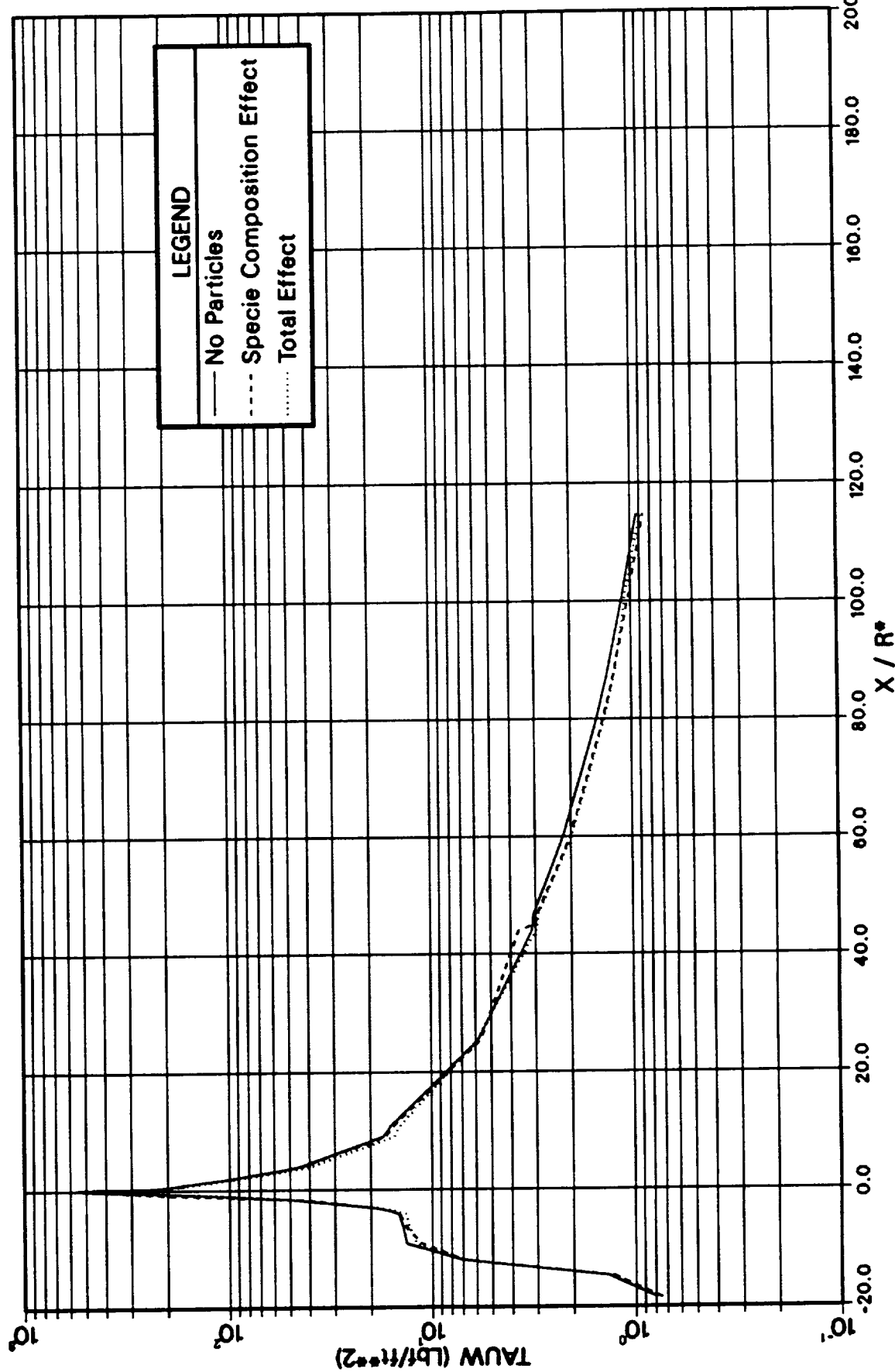
Figure 4.10: Shear Distribution Over the Whole Nozzle Length

REMTECH

OTV NOZZLE
LOADING = 0.5
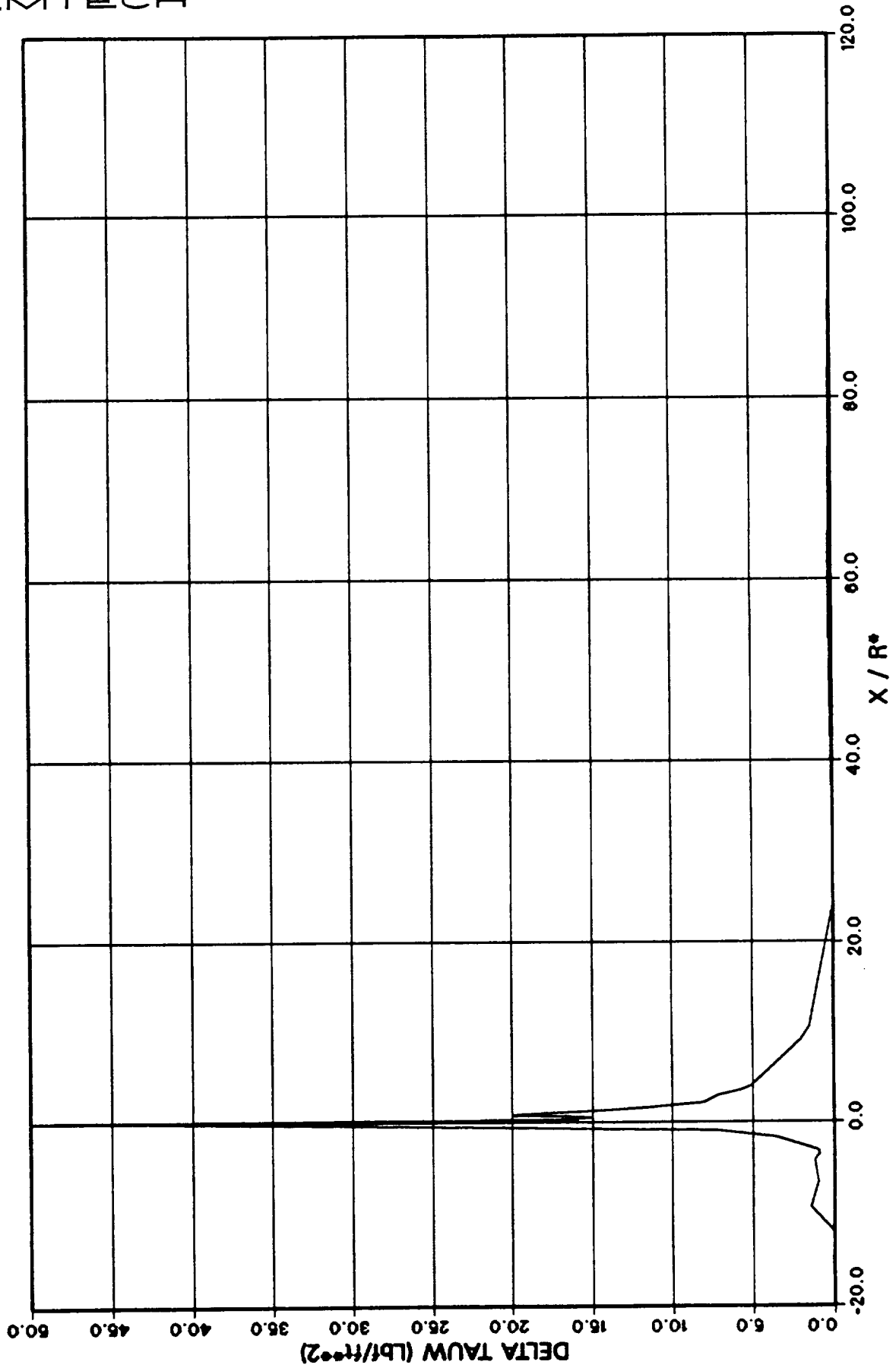
Figure 4.11: Delta Tauw between Total Particle Effects and Clean Flow Cases

67
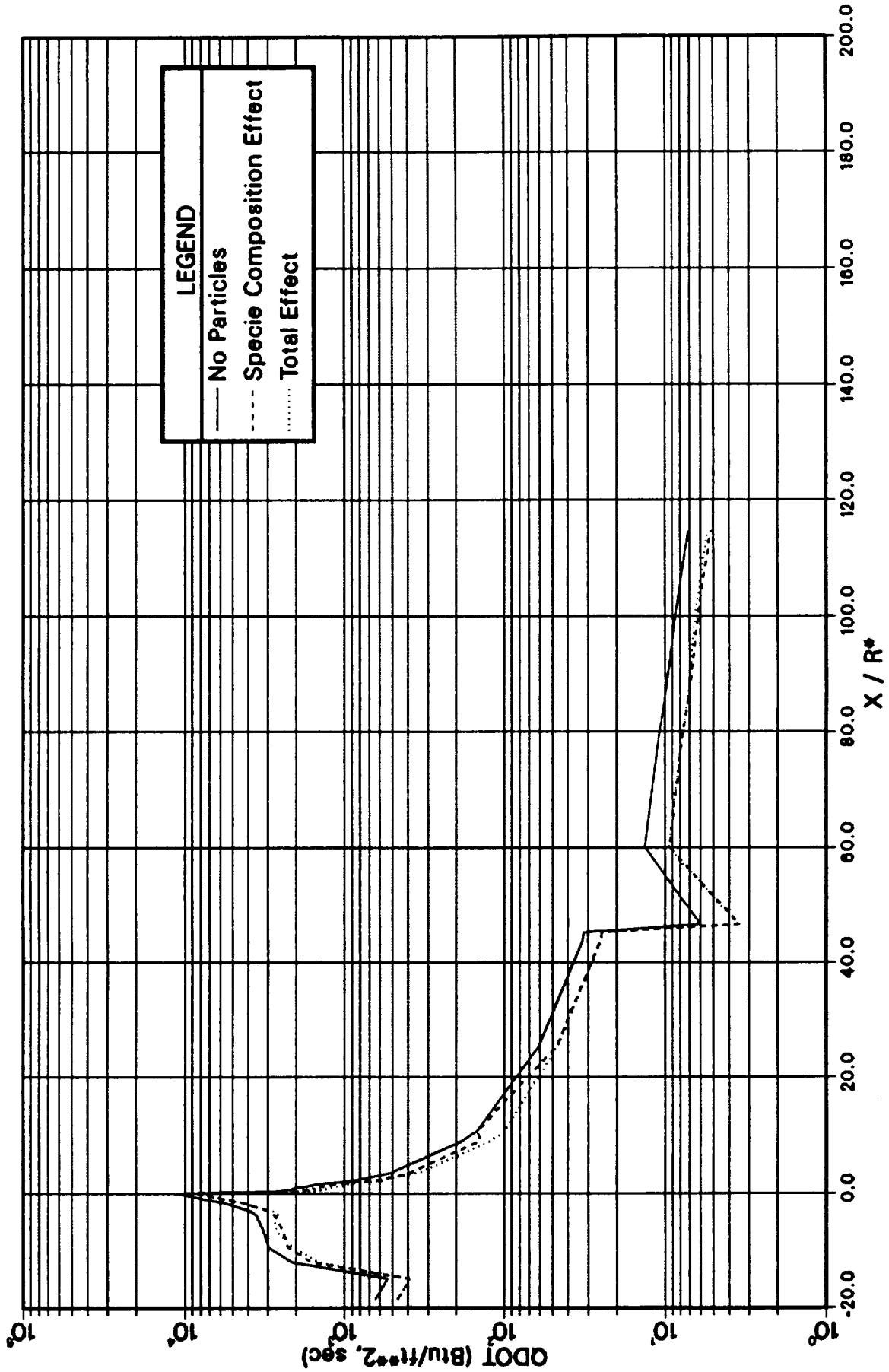
Figure 4.12: Heat Transfer Distribution Over the Whole Nozzle Length

REMTECH

OTV NOZZLE
LOADING = 0.5
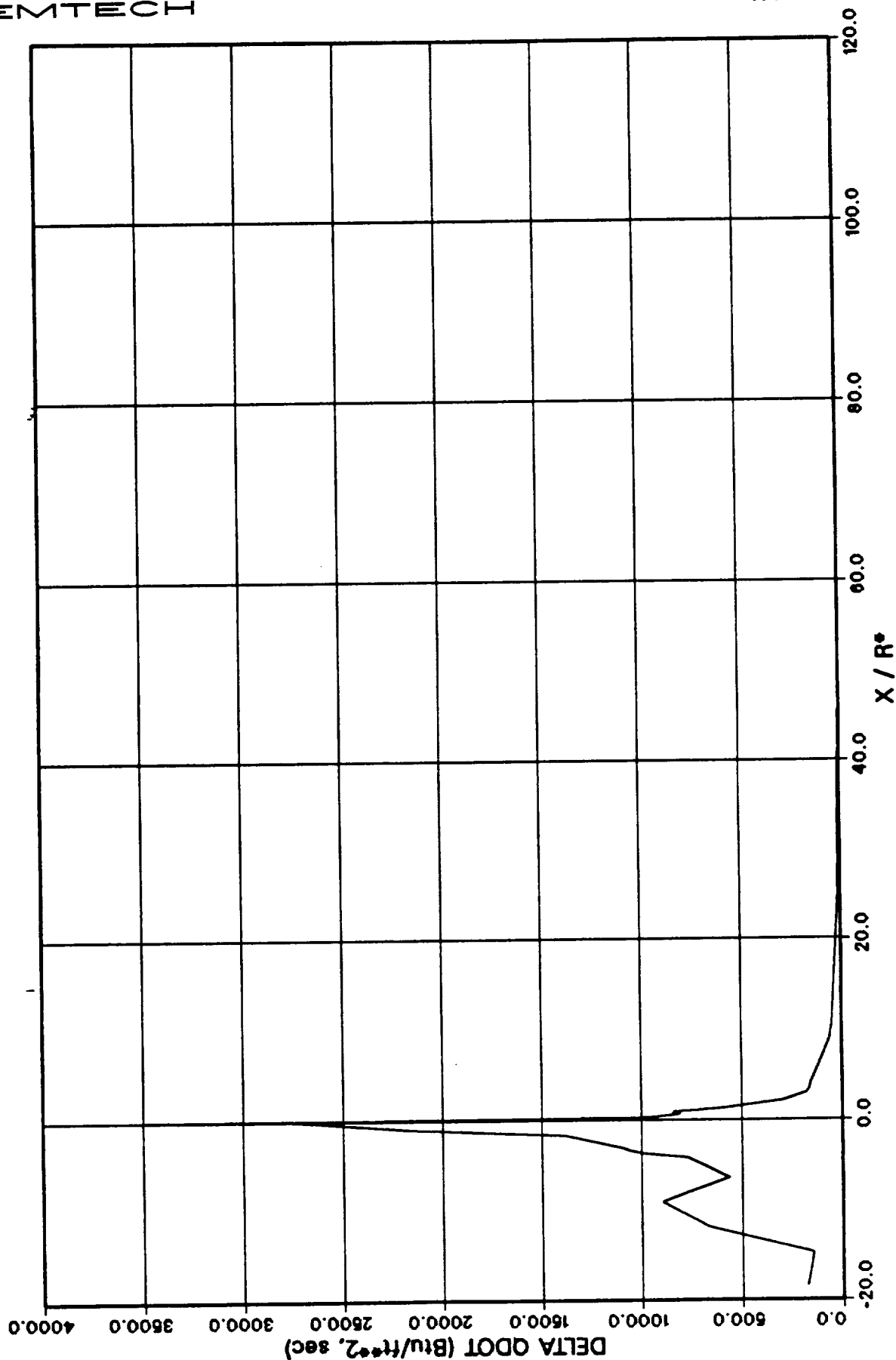
Figure 4.13: Delta Qdot between Total Particle Effects and Clean Flow Cases

X / R*

DELTA QDOT (Btu/ft**2, sec)
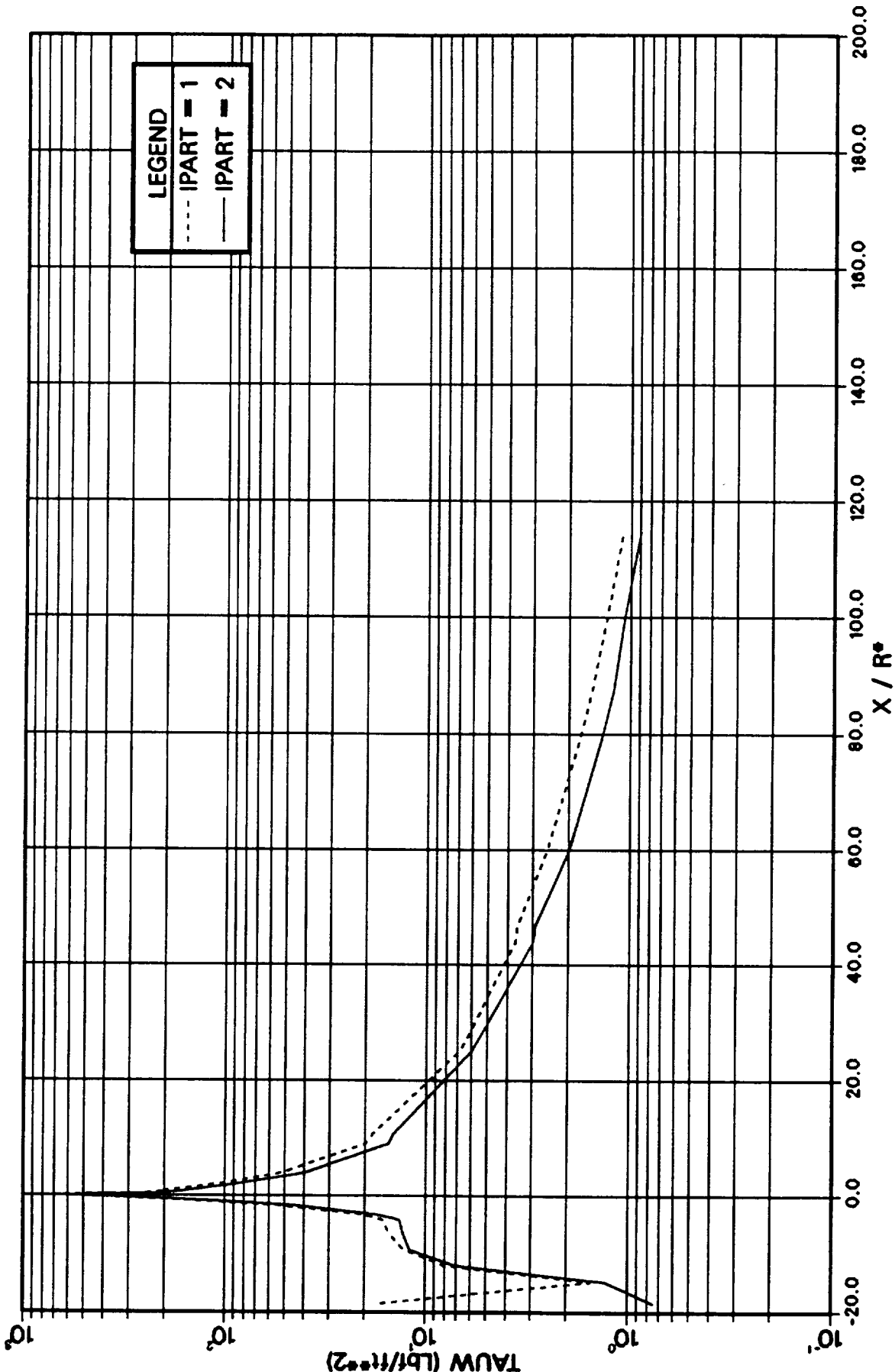
Figure 4.14: Comparison of Wall Shear Between the Two Coded Options in BLIMPJ
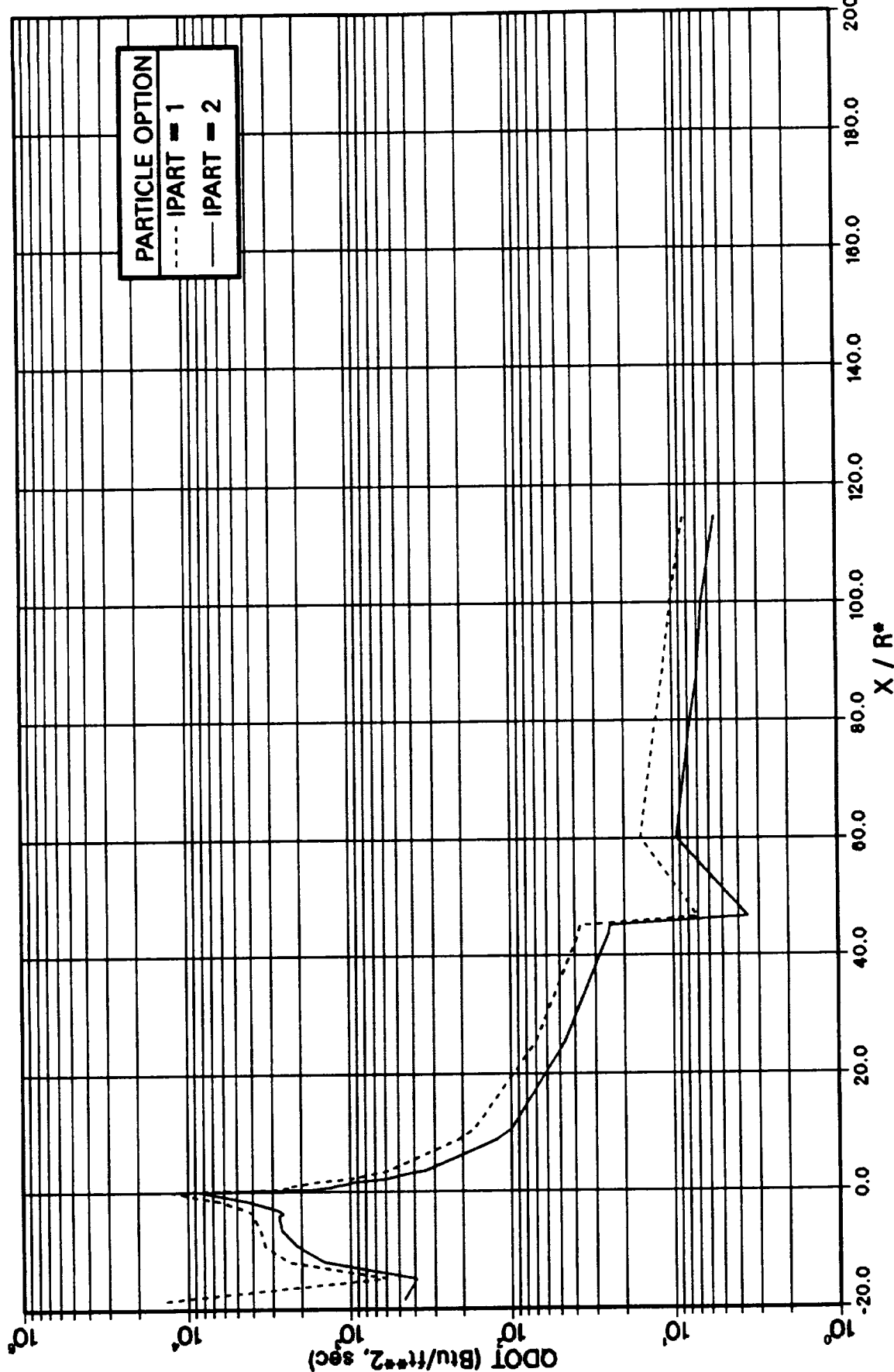
Figure 4.15: Comparison of Heat Transfer between the Two Coded Options in BLIMPJ

Section 5

THRUST DECREMENT CALCULATION

5.1 Background

The thrust loss calculation originally implemented in BLIMPJ [1] has been modified by REMTECH in Ref. [3]. The modified procedure is particularly applicable to the projected OTV engine nozzles with high area ratio. The boundary layer size in such nozzles depends basically on:

1. Longitudinal wall curvature

2. Pressure gradient normal to the wall

3. Transverse curvature

4. Fluid stratification (density)

The first two items are related through the y-momentum equation. The governing boundary layer equations and their solution in BLIMPJ take into account transverse curvature effects. The last item is a result of density gradients in the boundary layer. In general, similarity cannot be satisfied in such nozzles with all the above effects present. Fortunately, BLIMPJ does not assume similarity. Three out of the above four effects were not accounted for in the original version of BLIMPJ. Not only that, but the expression for the thrust loss calculation did not include the consequences of these effects. So, in order to take these into account, an approximate procedure (in keeping with the philosophy of simplified procedures) was implemented in Ref. [3]. In this procedure, the pressure which is an input parameter to BLIMPJ was replaced by an average value of the pressure distribution within the thickness of the boundary layer. The above approximation, in effect, included the contributions of longitudinal curvature, normal pressure gradient and fluid stratification to thrust decrement calculation. This procedure was applied in Ref. [3] to a typical Orbit Transfer Vehicle (OTV) nozzle and was seen to converge in the iteration procedure employed. Some of the assumptions made in the iteration procedure are the following:

1. The average inviscid pressure obtained from TDK across the boundary layer width is a reasonable value to be used in BLIMPJ to define the boundary layer in the successive iterations.

REMTECH

2. The longitudinal curvature effect is only considered approximately through the pressure averaging procedure.

In the previous work [3], all these assumptions along with other standard boundary layer assumptions were made. It also provided procedures for calculating the performance of a rocket nozzle experiencing thick boundary layers for the two different cases given below:

Case 1 – The potential nozzle contour is given and the objective is to define the hardware wall contour.

Case 2 – The hardware wall contour is given and the objective is to define the potential contour and calculate the nozzle performance.

The method had been checked out for the OTV nozzle using the procedure for Case 1. It used RAMP [23] as the inviscid code to define the pressure profiles and some of the pressure averaging was performed by hand. The current procedure uses TDK instead of RAMP to define the inviscid flowfield and a code was developed consisting of FORTRAN and control language to couple TDK and BLIMPJ to perform the iteration procedure in an automatic mode. The details are given in the following subsection.

5.2 Coupling of TDK with BLIMPJ

Calculation of the thick boundary layer effects on thrust loss has been accomplished using the procedure shown in Fig. 5.1. The first step of this procedure is to calculate the inviscid internal flowfield using TDK. As part of this procedure, two factors must be considered when running TDK:

1. Since the inviscid flowfield data need to be stored for the region where the boundary layer exists, special care has to be taken in running TDK. The extent of the flowfield calculations from the current TDK version is limited by the last left-running characteristic line emanating from the initial Start line, the nozzle axis or the shock, and ending at the nozzle lip. As a result, the streamline data throughout the boundary layer width at the exit plane are not available. Thus, in order to compute this additional streamline information, the nozzle must be extended for the input to TDK.

2. The size of the flowfield data file may be exceeded depending on the number of start line data points and geometry of the nozzle. If this size is exceeded, then the data file will be overwritten. To extend the size of the file, the

variable IDMAX must be increased in the TDK input file (default: IDMAX = 50,000).

Step two of the procedure is to run BLIMPJ to calculate the thickness of the boundary layer. For the first iteration, BLIMPJ uses the wall pressures as an approximation of the pressure distribution within the boundary layer. For every additional iteration, BLIMPJ uses the integrated pressures generated by the Near Wall Profile code (NWP) [24], written by the authors to couple TDK and BLIMPJ.

The third step in the procedure is to run NWP to calculate the thickness of the boundary layer. The inputs to this code include the flowfield data file generated by TDK, and the boundary layer thickness generated by BLIMPJ. The output of NWP includes a streamline data file which is generated in the first iteration and accessed by each successive iteration. This coupling logic which was written for the VAX (and can be easily written for the CRAY) is reproduced in Fig. 5.2. The operation of this software requires one-time inputs to both TDK and BLIMPJ.

Since the potential contour is given (Case 1), the hardware contour is obtained from

$$R_B = R_P + \delta^* \cos \phi \tag{5.1}$$

where R_B is the hardware contour radius, R_P is the potential contour radius, δ^* is the converged value of the boundary layer and ϕ is local wall slope. The procedure for Case 2 is well documented in Ref. [3] and will not be dealt with here.

5.3 Concept Checkout

The NWP code linking the outputs of TDK and BLIMPJ compiles the flowfield data for the streamlines emanating from the start line profile, going across the shock located in the flowfield and ending on the last left-running characteristic line running to the extended nozzle lip; calculates pressure profiles at given x-locations by interpolating on individual streamlines; and integrates the pressure profiles and calculates average pressure values on the wall.

The OTV nozzle was extended at its exit plane in a conical fashion, keeping the exit flare angle to be the same. The length of the nozzle needed to provide streamline information within the boundary layer was $X/R_T = 200$, where the area ratio was 2107·7. TDK was run up to this area ratio, yielding the streamlines shown in Fig. 5.3. Figures 5.4 and 5.5 show, respectively, the calculations of the boundary layer thickness distribution and of the pressure profiles in a direction normal to the

axis between the nozzle wall and the boundary layer edge location based on the information obtained from the streamline data. This is the first iteration. Since the boundary layer edge is not known for a thick boundary layer, an iteration procedure (Fig. 5.1) is required. Figures 5.6 and 5.7 represent the results for the second iteration. Examination of the iterated average pressure values along the wall in Fig. 5.8 and the thrust decrement due to the boundary layer in Fig. 5.9 shows that no more iterations are necessary.

In the above calculations the boundary layer thickness was measured from the wall in a direction normal to the nozzle axis. Since it is more accurate to measure the boundary layer normal to the nozzle wall, NWP was modified and the first iteration was completed. The zeroth iteration in BLIMPJ utilized the inviscid wall pressures from TDK and calculated boundary layer quantities including the thrust loss. This boundary layer width was sufficient to show a variation of pressure across the boundary layer region of the inviscid flowfield. Thus, an iteration was necessary in BLIMPJ to use an average pressure across the boundary layer region obtained from the streamline information output by TDK. The extent of the boundary layer width in relation to the inviscid streamlines is given in Fig. 5.10. Note that the boundary layer plotted here is measured normal to the wall. This is the first iteration. Iterations continued until a convergence of the thrust loss was achieved with a specified tolerance between successive iterations. Figure 5.11 shows the boundary layer width plot in the second iteration. It is obvious that the boundary layer thickened because of lower average input pressures at the wall. The pressure profiles in the second iteration plotted on the projection of the wall-normal boundary layer width on the Y-direction are given in Fig. 5.12. The average pressure values along the nozzle wall for the inviscid wall pressure case and for the two iterations are given in Fig. 5.13. It is also seen that the first and second iterations are very close to each other. The reason for the unsmooth nature of the curves for the last two iterations in the X/R_T range of 6 to 32 is not very clear. The thrust loss distributions along the wall are given for the zeroth and second iterations as a function of area ratio in Fig. 5.14. It is seen that the losses are reduced due to the convergence procedure. Figure 5.15, on the other hand, gives the overall thrust loss of the nozzle as a function of the BLIMPJ iterations and compares the results of the new method described here against the more approximate method reported earlier. Method II, which is more exact than Method I, shows somewhat more thrust loss, but quicker convergence. The thrust area ratio distribution from ODE, ODK, TDK and actual calculations using this procedure are given in Fig. 5.16.

5.4 Thrust Loss Optimization

The concept of using a high area ratio nozzle in the projected OTV engine stems from the fact that the specific impulse loss is minimized in such nozzles. As the area ratio grows in magnitude, the two-dimensional losses become smaller and smaller. However, as the area ratio increases, so does the friction loss. This has been pointed out by numerous investigators. As a result, the exit area ratio at which the inviscid thrust is maximum may be different from the area ratio at which the actual thrust reaches a maximum.

The subject of thrust loss optimization must be considered during the design stage. The desirability of improving on the "perfect" nozzle has been the subject of various optimization procedures. One of those is due to Rao [25] where, given the throat flow characteristics, nozzle length and ambient pressure, the procedure provides a nozzle contour yielding maximum thrust. This optimization procedure does not include the effects of wall friction.

The thrust loss optimization problem may follow the procedure given below:

1. Calculate a series of potential nozzles using such procedures as implemented in the Rao algorithm and others for various lengths. Each nozzle has a different area ratio and an optimized contour.

2. Calculate the corresponding inviscid thrust for each nozzle.

3. Once the nozzle contours are available, thick boundary layer calculations based on the procedure described earlier should be followed to define the thrust loss, and final displacement thickness distribution along the nozzle wall and the corresponding hardware nozzle wall contour. This defines the thrust loss variation with area ratio for nozzles with optimum contours.

4. Optimize the resulting thrust (= T inviscid − friction drag) with respect to area ratio with possible length or structural weight constraints.

The above procedure must be considered preliminary at this stage. Other issues such as structural design and other nozzle losses may play significant roles in this optimization process.

It is well known that the gain of the ISP obtained by expanding the flow in a high area ratio nozzle is limited by the boundary layer losses. It was seen in Fig. 5.14 that as the area ratio increases, so does the boundary layer loss. Thus, the area ratio must be optimized to yield maximum performance. A parametric study was conducted for a typical high expansion area ratio nozzle such as the OTV

nozzle. The only parameter chosen for the study was area ratio. The geometry of the nozzle for each area ratio was assumed to be a part of the same overall high area ratio nozzle. The thrust calculations shown in Fig. 5.16 were obtained from the ODE, ODK, TDK and real thrust calculation algorithms. The differences between ODE and ODK are due to the kinetic losses. The differences between ODK and TDK are attributed to the two-dimensional losses. The thrust decrements due to the boundary layer losses are given by the lower curve. Note that the thrust decrement iteration procedure described earlier has been taken into account for the lower curve.

The thrust loss optimization work performed so far was applied to the OTV nozzle. The area ratios higher than the design exit area ratio were obtained by extending the nozzle from the exit plane. The extended length of the nozzle needed to apply the iteration procedure was at an area ratio, $A/A^* = 2500$. BLIMPJ was run up to this area ratio. The thrust loss distribution from the zeroth iteration over the nozzle length is shown in Fig. 5.17. The abrupt change in slope of this curve around $A/A^* = 1293$ may be attributed to the abrupt change in the second derivative of the nozzle area ratio with respect to axial distance. This also shows the thrust loss variation with area ratio as a function of iterations as the solution converges. The convergence required only three iterations to reach the tolerance of 1 lb. thrust between iterations at the exit plane area ratio, $A/A^* = 1852$. Although the original intention was to run up to an area ratio of 2500 to obtain all the needed profile information at the exit plane area ratio of approximately 2000, the last left-running characteristic did not yield all the streamline information all the way up to the boundary layer edge location at Sta. 2000. As a result, the last station at which all the streamline information was available was Sta. 1852. Figure 5.18 shows the thrust loss as a function of iterations for $A/A^* = 1852.53$ and 1267.22. The last A/A^* was close to the former exit area ratio of 1293. It must be noted that the tolerance between the second and third iteration is one lb. for both stations. The thrust information is given in Fig. 5.19 where the inviscid thrust from TDK, thrust loss from BLIMPJ for the last iteration and the resulting actual thrust are plotted.

One can already observe the ineffectiveness of the nozzle in producing more thrust beyond $A/A^* = 1293$. To quantify this thrust increase with area ratio, Fig. 5.20 was prepared showing change of thrust from station to station as a function of area ratio. It is very clear that beyond $A/A^* = 1852.22$ where the change of thrust from its previous station is about 15 lbs., no more appreciable thrust gain will be realized by further extending the nozzle. The zero location of this plot was not obtained for the following reasons:

1. It was not possible to run beyond $A/A^* = 1852$ at REMTECH's VAX be-

cause of space limitations.

2. Since the inviscid thrust increases by extending the nozzle in a conical fashion, and the thrust loss also increases because of higher displacement effects with running length, the total thrust may be asymptotic in nature. This must be considered a conjecture at this point.

3. On the other hand, if the nozzle were extended in a cylindrical fashion, the inviscid thrust should level off and the viscous losses should increase, thus resulting in negative change of thrust from station to station. This has not been exercised at this point.

REMTECH
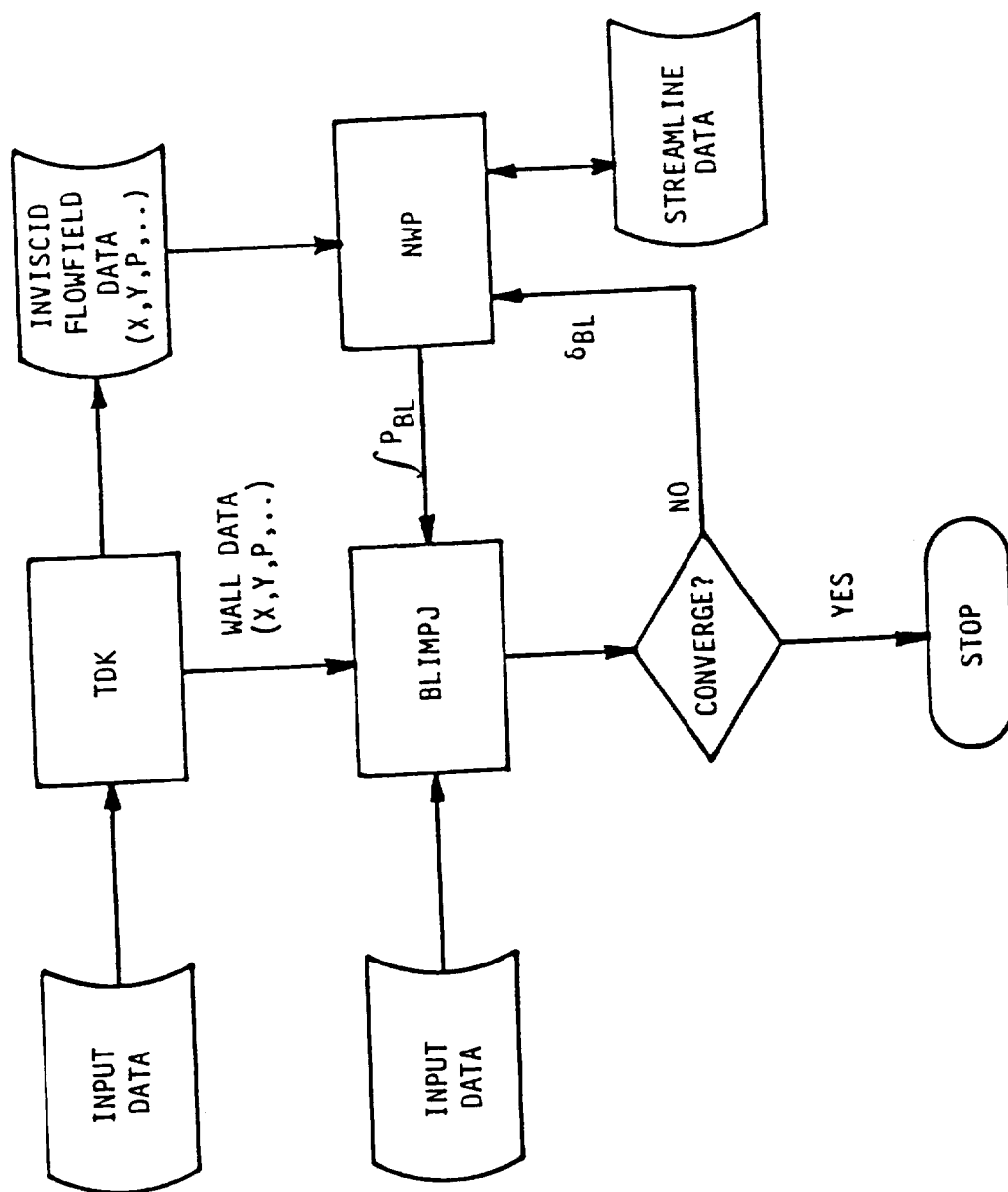
Figure 5.1: Schematic of Coupling between TDK and BLIMPJ

```
$!
$! The following is a set of jcl to execute the TDK, BLIMPJ and NWP1 until
$! a solution is found ( i.e. thrust loss for a given model is less
$! than 20 lbs )
$!
$!
$! Note: All text to the right of an "!" is to be considered a comment
$!
$! D. Hollman
$! REMTECH Inc.
$! 29-APR-88
$ SET DEF DSA1:[HOLLMAN.TDK] ! Move to current directory
$
$ WRITE SYS$OUTPUT " 1.   START AT BEGINNING"!
$ WRITE SYS$OUTPUT " 2.   START AT BLIMPJ3"  ! Output menu to user
$ WRITE SYS$OUTPUT " 3.   START AT NWP1"     !
$ WRITE SYS$OUTPUT ""
$
$ INQUIRE/NOPUN CHOICE "ENTER CHOICE -->" ! Get input from user
$ WRITE SYS$OUTPUT ""                     !

$ IF CHOICE .EQ. 1 THEN GOTO START ! If user selects "1", start at beginning
$ INQUIRE COUNT "ENTER ITERATION NUMBER -->" ! Get starting iteration number
$ IF CHOICE .EQ. 2 THEN GOTO BLIMPJ ! Start at BLIMPJ
$ IF CHOICE .EQ. 3 THEN GOTO NWP ! Start at NWP
$
$ START:
$
$ COUNT = 1                     !
$ OPEN/WRITE FILE ITER.DAT ! Output current iteration number to "ITER.DAT"
$ WRITE FILE ''COUNT'         !
$ CLOSE FILE                  !
$
$ BLIMPJ:
$ CLOSE ITER.DAT
$ UNLOCK ITER.DAT
$ P1 = "BLM_ITER''COUNT'.OUT" ! Assign iteration dependent filenames to
$ P2 = "AVG_PRESS_ITER''COUNT'.PLT" ! average pressure and BLM_ITER

$ ASSIGN "THRUST_LOSS_ITER''COUNT'.PLT" FOR072 ! Output thrust loss data
$                                         ! to unit 72
$ WRITE SYS$OUTPUT "ITERATION =''COUNT'" ! Notify user of progress
$ WRITE SYS$OUTPUT "EXECUTING BLIMPJ ..."!
$ @dua0:[eng_codes.tdk]b3 'P1 'P2 ! Execute BLIMPJ code
$ DEASS FOR072
$
$
$ NWP:
$ COUNT1 = COUNT + 1
$ COPY RADIUS2.DAT BNDRY_ITER'COUNT.DAT ! Copy radius information to bndry
$                                       ! layer file
$ ASSIGN "AVG_PRESS_ITER''COUNT1'.PLT" FOR071 ! Assign iteration dependent
$ ASSIGN "BNDRY_ITER''COUNT'.DAT" FOR020 ! average pressure and boundary layer
$                                        ! files to FORTRAN unit numbers
$ WRITE SYS$OUTPUT "EXECUTING NWP ..."
$ RUN NWP1 ! Execute NWP code
```

Figure 5.2: VAX JCL for Coupling Software

```
$ DEASS FOR071 ! Deassign FORTRAN unit numbers
$ DEASS FOR020 !
$
$ ! IF NWP HAS DECLARED THAT ANOTHER ITERATION SHOULD BE DONE, THEN GOTO ITER
$ OPEN/READ FILE ITER.DAT ! If NWP code declares we should stop, it will
$ READ FILE P1            ! write an "-1" in "ITER.DAT".  This routine will
$ CLOSE FILE              ! stop when condition is true.
$ IF P1 .EQ. "-1" THEN GOTO EXIT
$
$ ITER:
$ COUNT = COUNT + 1 ! Increment iteration counter
$ OPEN/WRITE FILE ITER.DAT ! Output iteration number to "ITER.DAT"
$ WRITE FILE ''COUNT'
$ CLOSE FILE
$ GOTO BLIMPJ ! Goto BLIMPJ section and repeat process
$
$ EXIT: ! Stop excecution
$
```

Figure 5.2: VAX JCL for Coupling Software (Concluded)
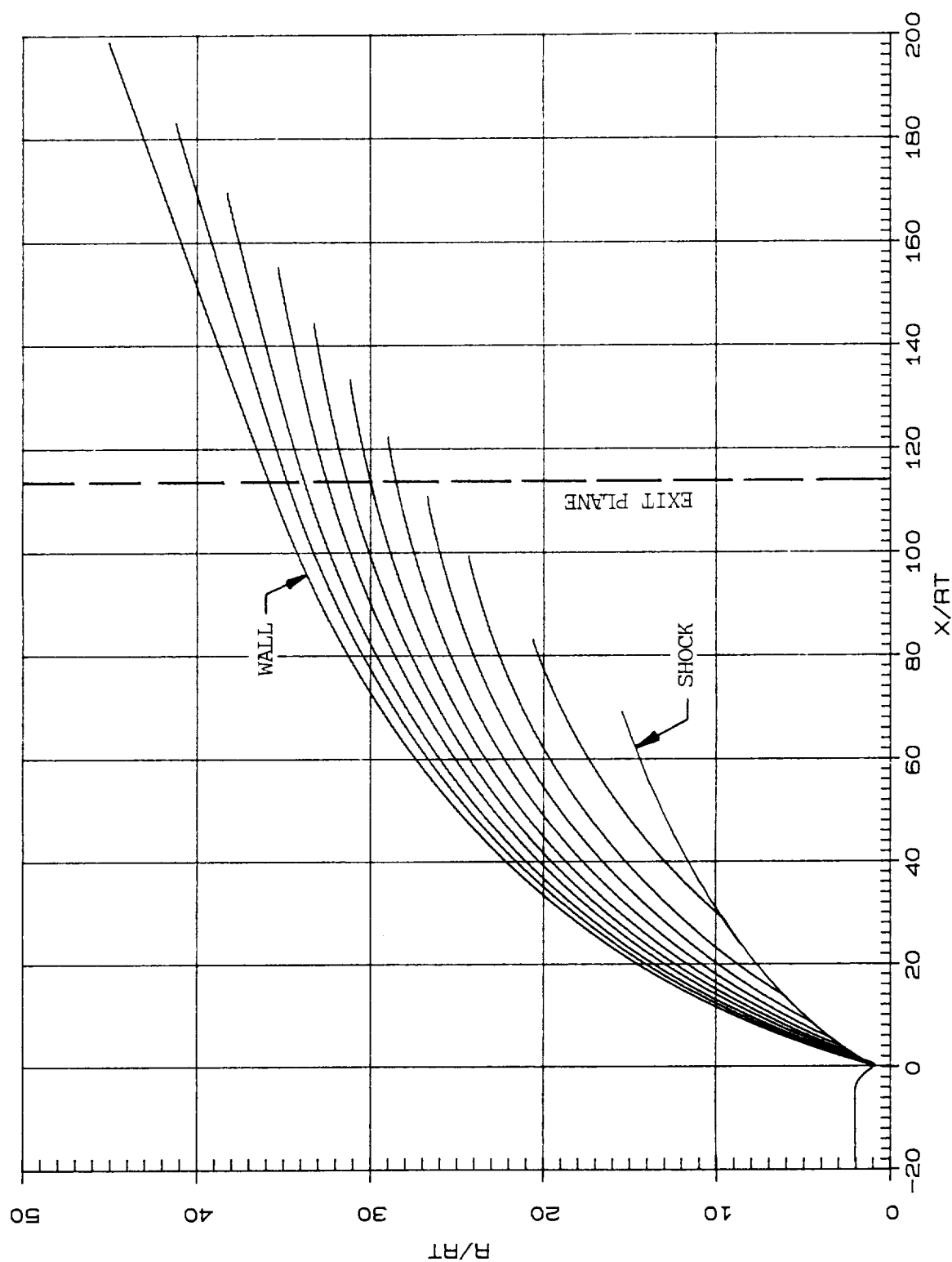
Figure 5.3: Streamlines in Near-Wall Region of the OTV Nozzle

REMTECH
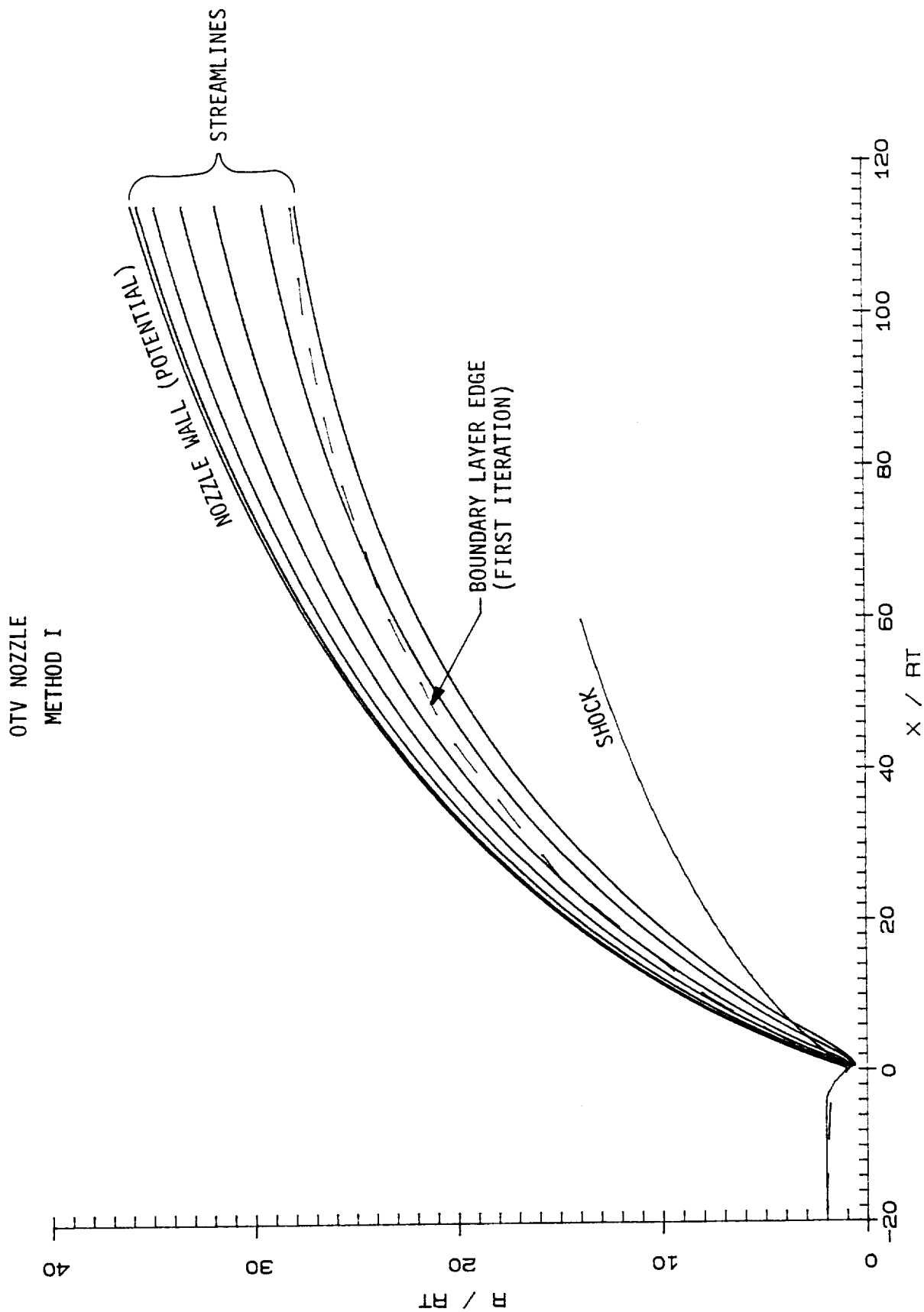
Figure 5.4: TDK-derived Streamlines Near the Nozzle Wall

REMTECH

OTV NOZZLE
METHOD I
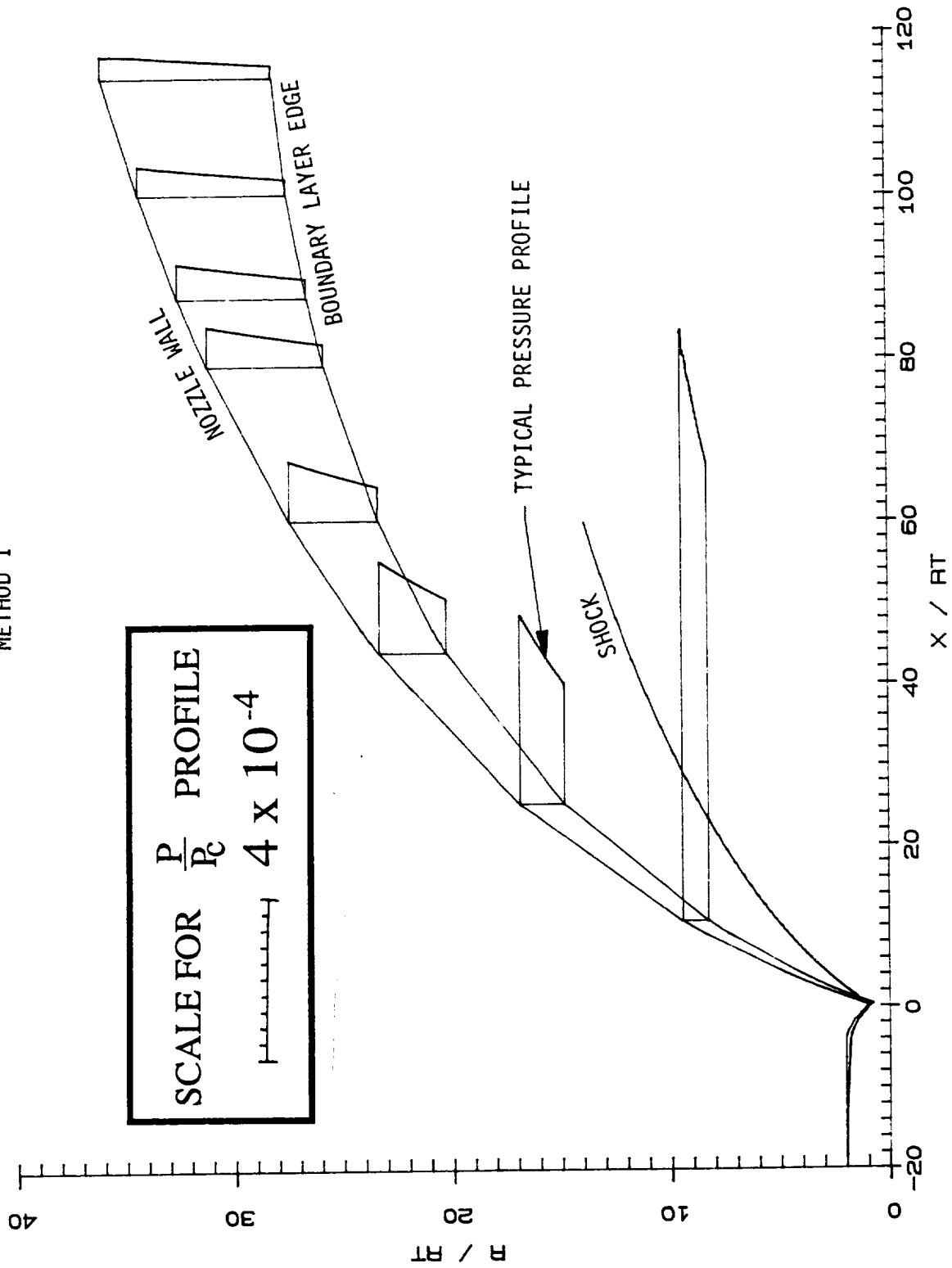
Figure 5.5: Inviscid Pressure Profile Between Nozzle Wall and Boundary Layer Edge Along a Direction Normal to the Axis (First Iteration)

REMTECH

OTV NOZZLE

METHOD I

SCALE FOR $\dfrac{P}{P_C}$ PROFILE

$\longmapsto$ 4×10^{-4}
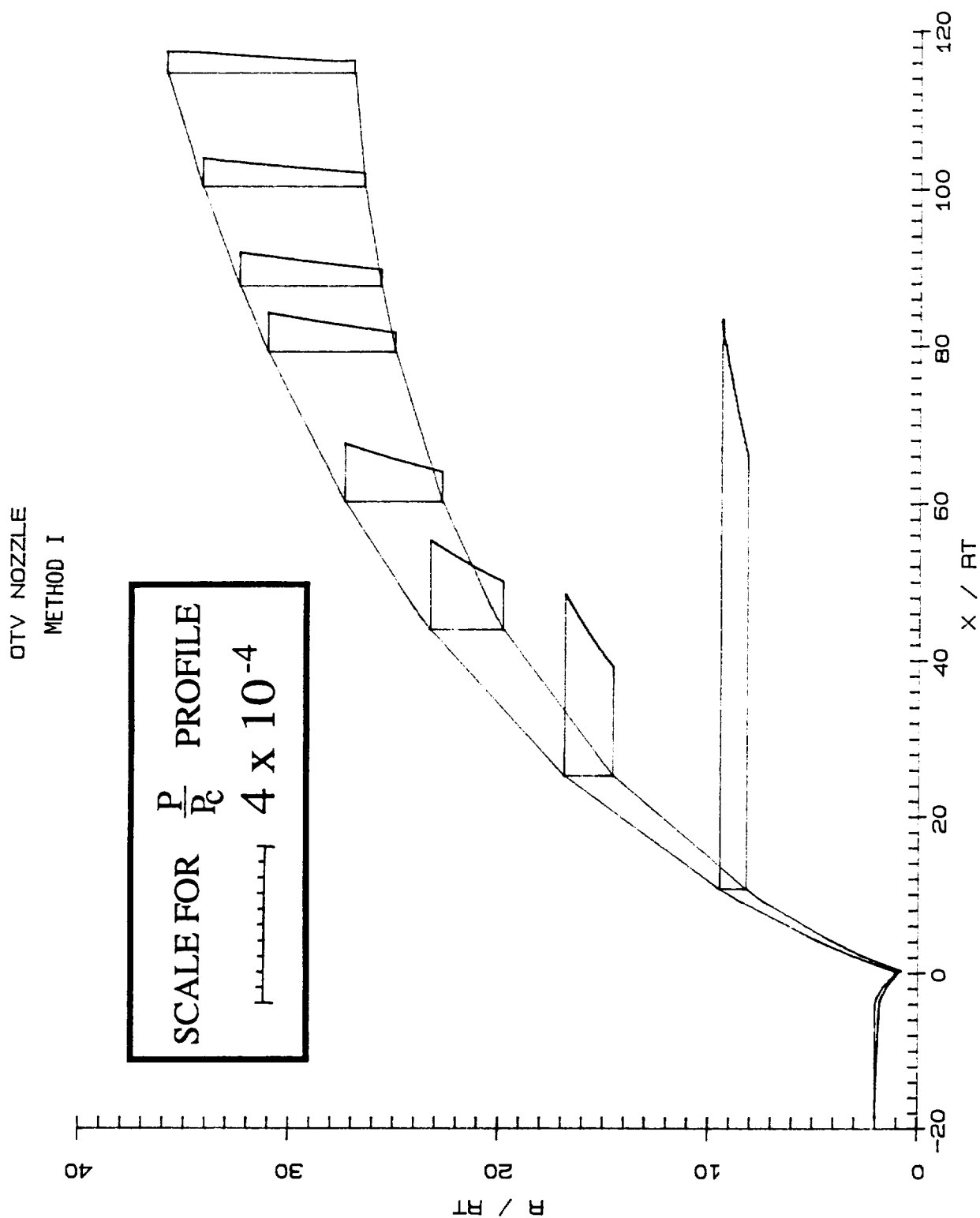
Figure 5.7: Pressure Profiles for Second Iteration of Boundary Layer Edge Along a Direction Normal to the Axis
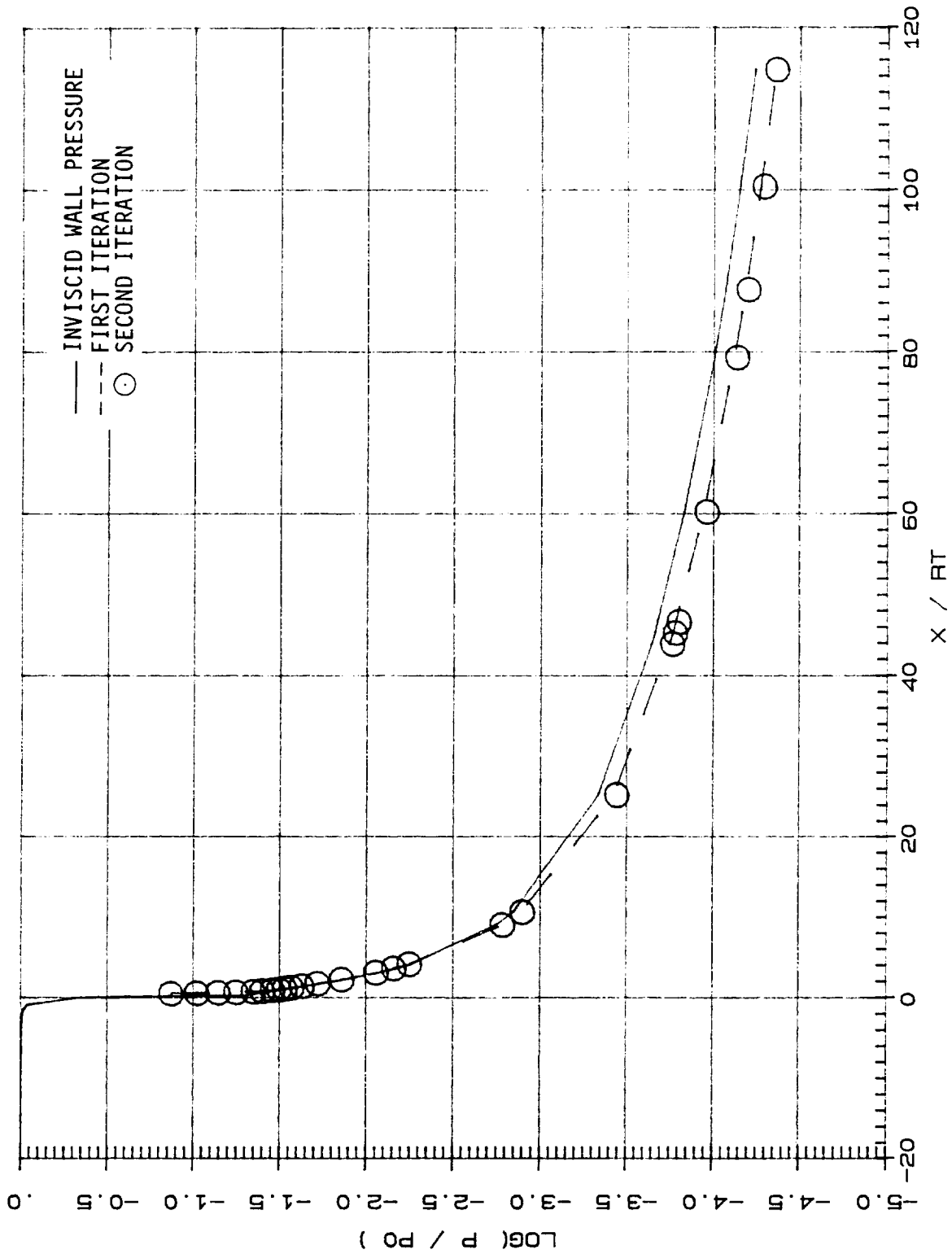
REMTECH

Figure 5.8: Pressure Distribution Along Nozzle Wall at Successive Iterations in Method I

REMTECH
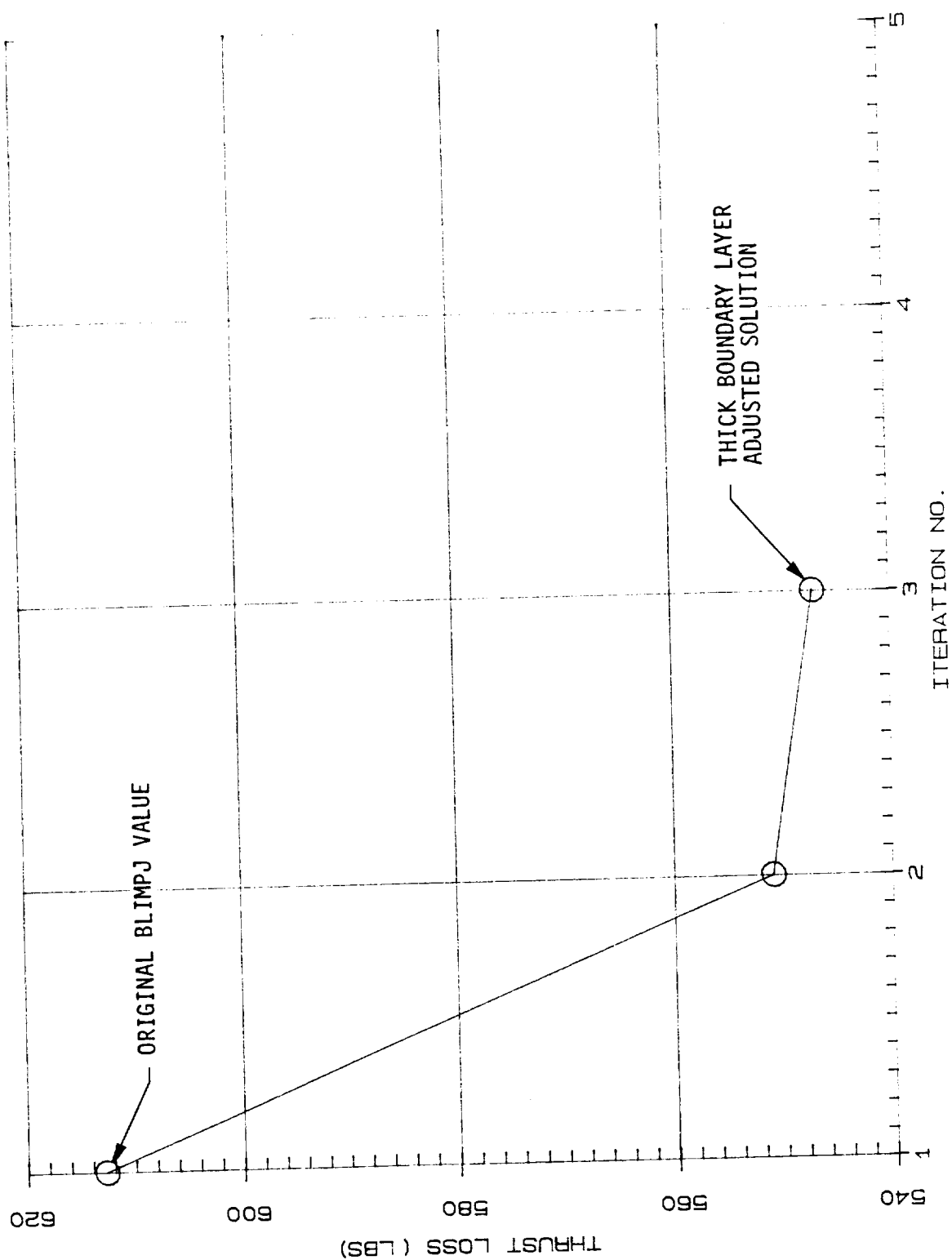
Figure 5.9:   Thrust Loss Iteration in Method I

REMTECH

OTV NOZZLE
METHOD II
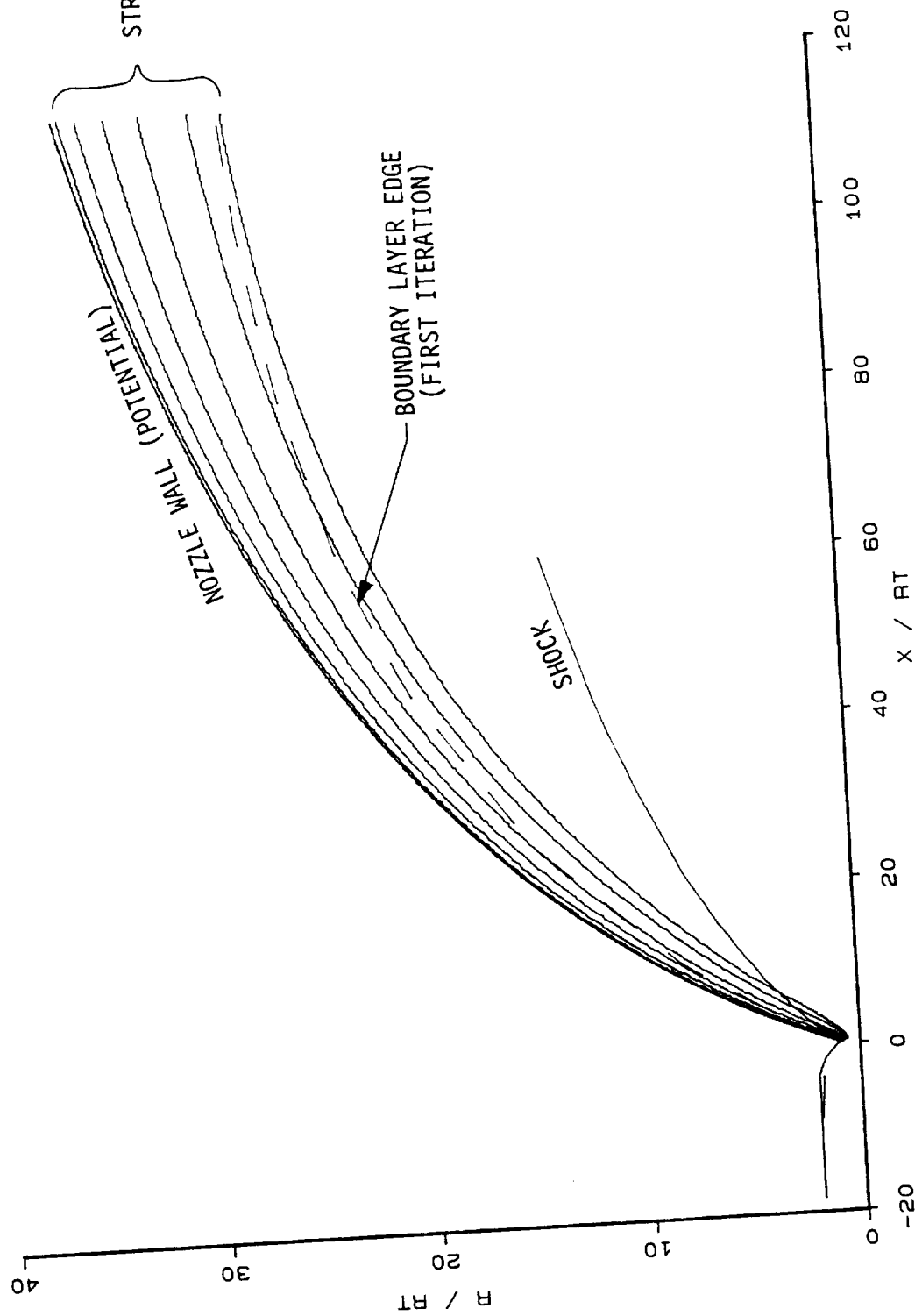
Figure 5.10: TDK-derived Streamlines Near the Nozzle Wall and Boundary Layer
Width (Normal to the Wall) in First Iteration
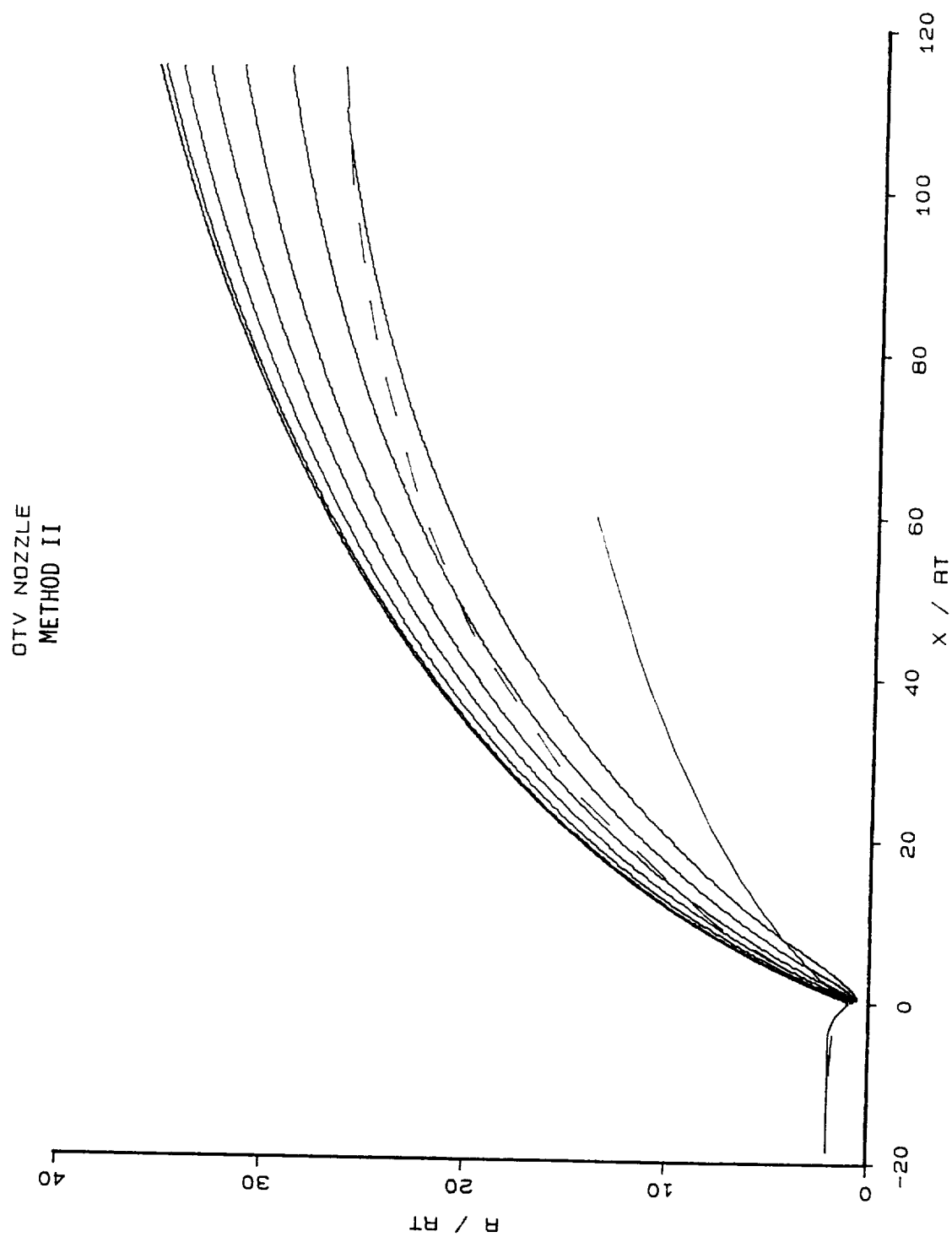
Figure 5.11: TDK-derived Streamlines Near the Nozzle Wall and Boundary Layer Width in Second Iteration
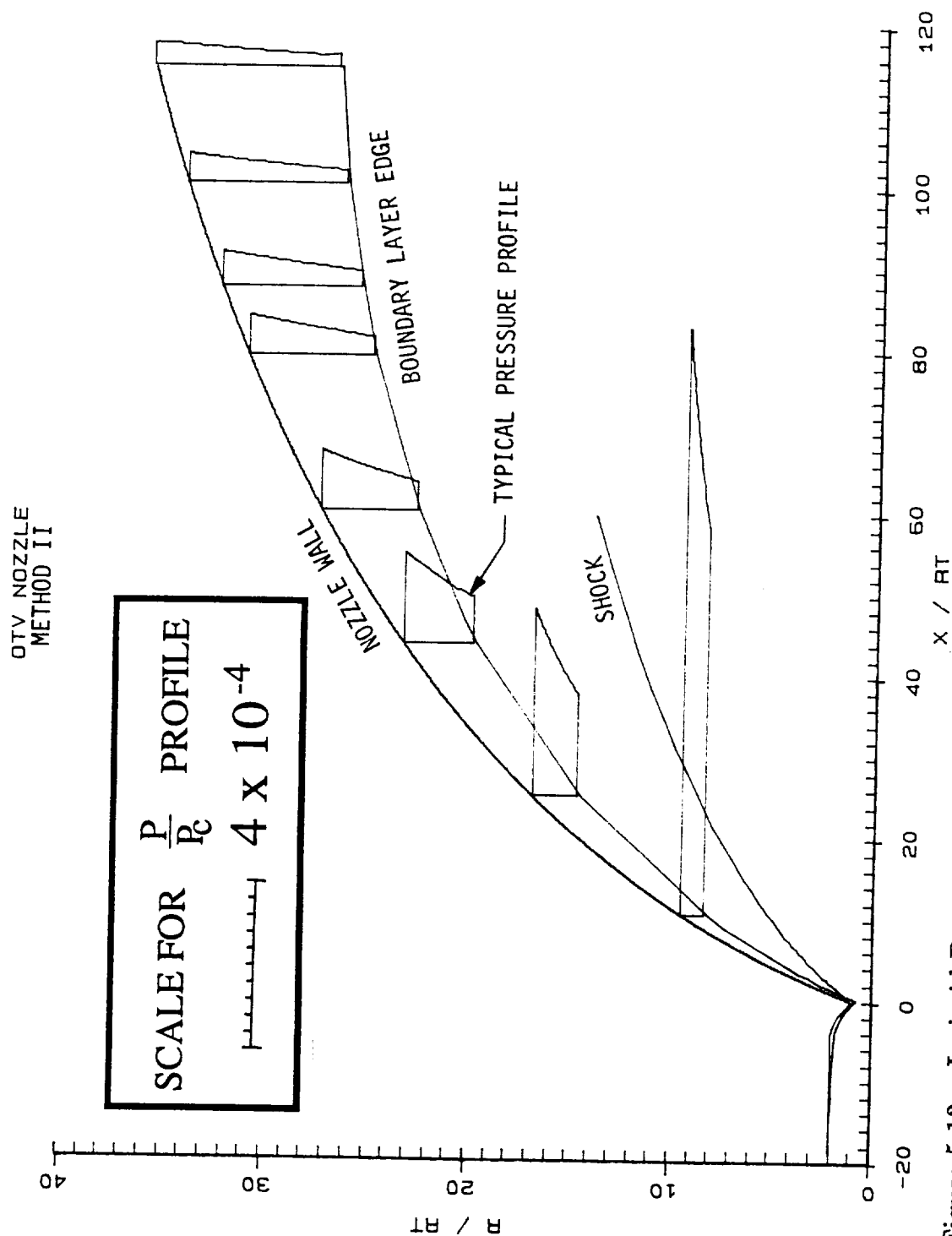
Figure 5.12: Inviscid Pressure Profile between Nozzle Wall and Boundary Layer Edge in Second Iteration
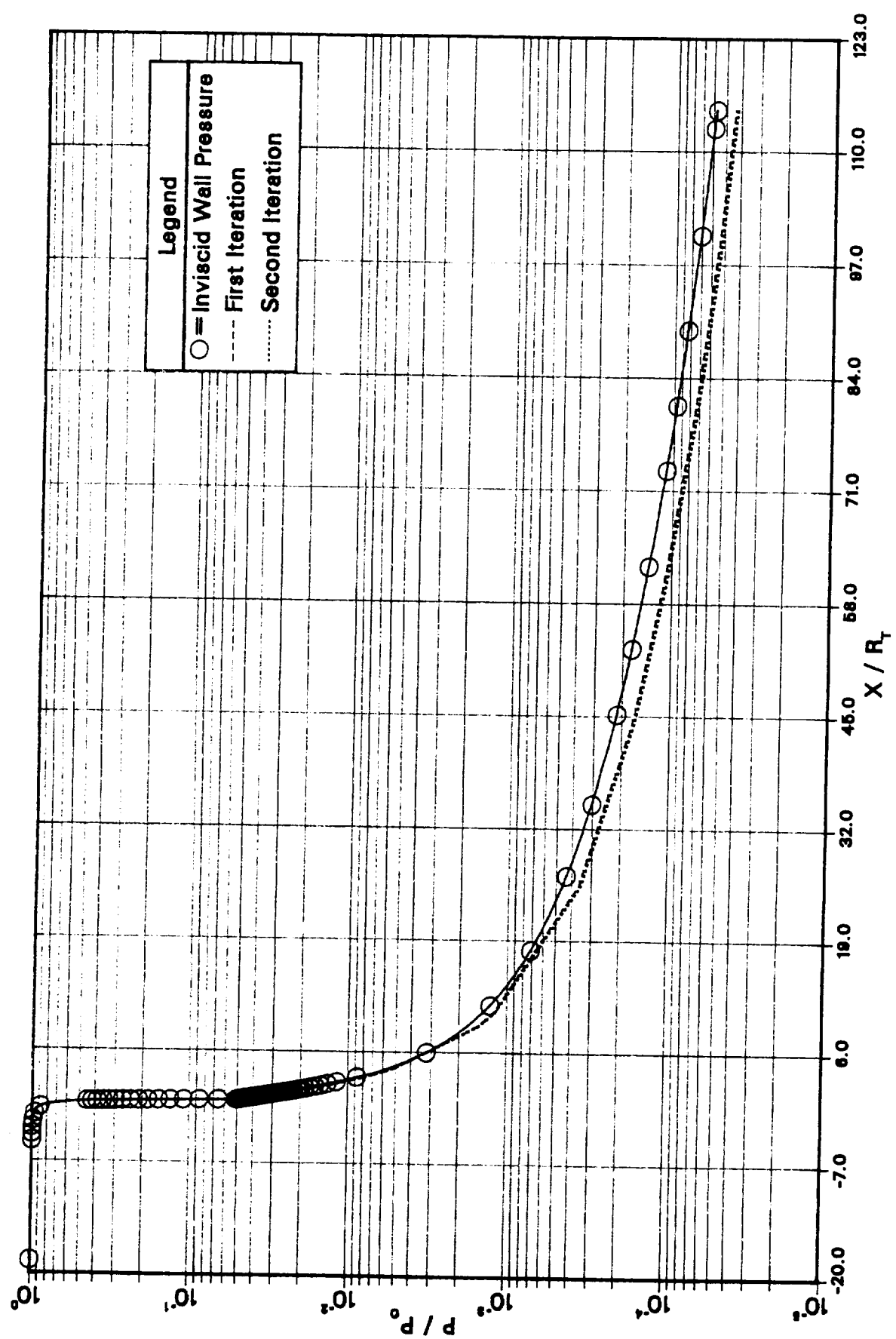
Figure 5.13: Average Pressure Distribution on Nozzle Wall
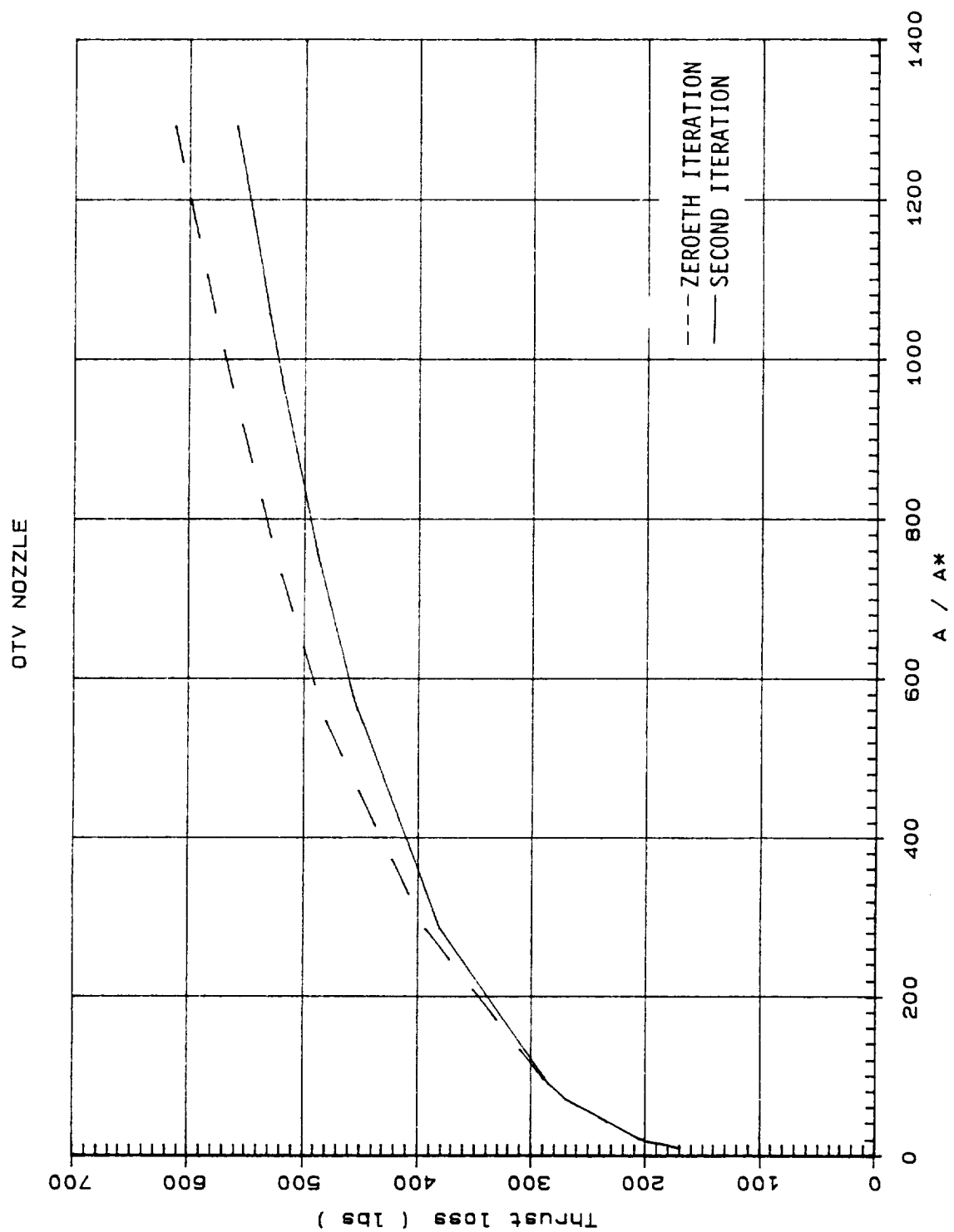
Figure 5.14: Thrust Loss as a Function of Area Ratio in Method II
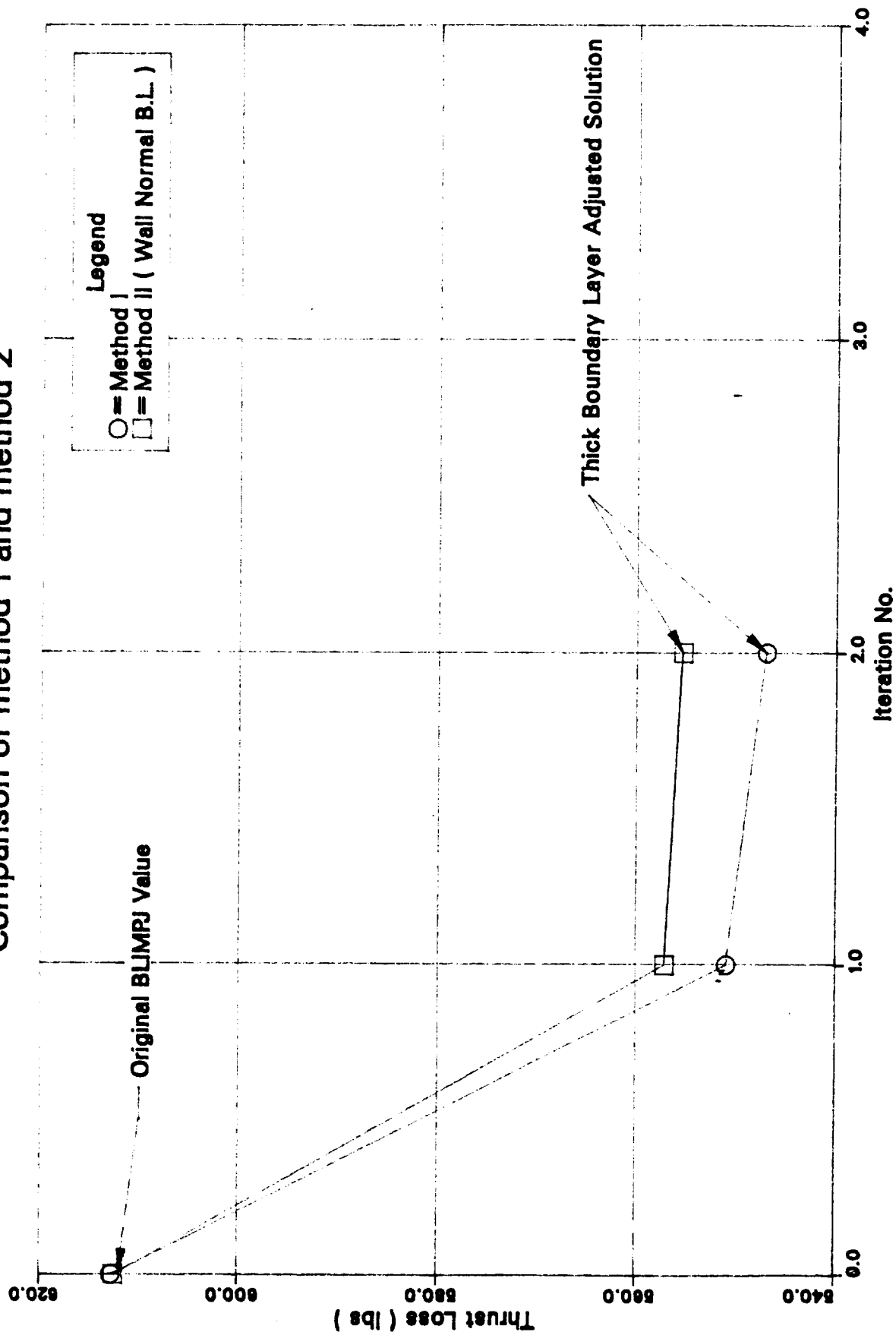
Figure 5.15: Thrust Loss Iteration
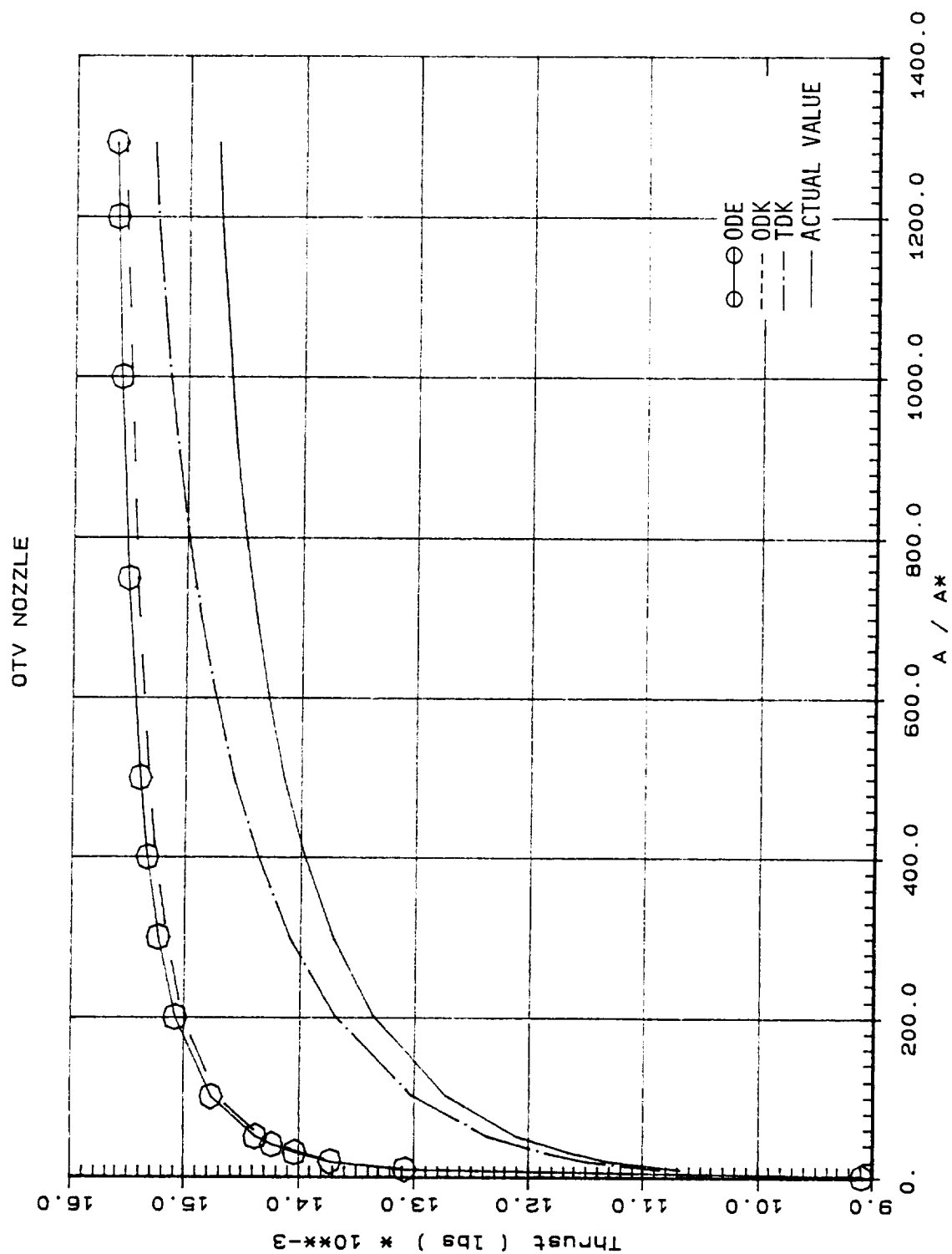
Figure 5.16: Thrust Variation with Area Ratio

Extended OTV Nozzle

Area Ratio = 1852.53
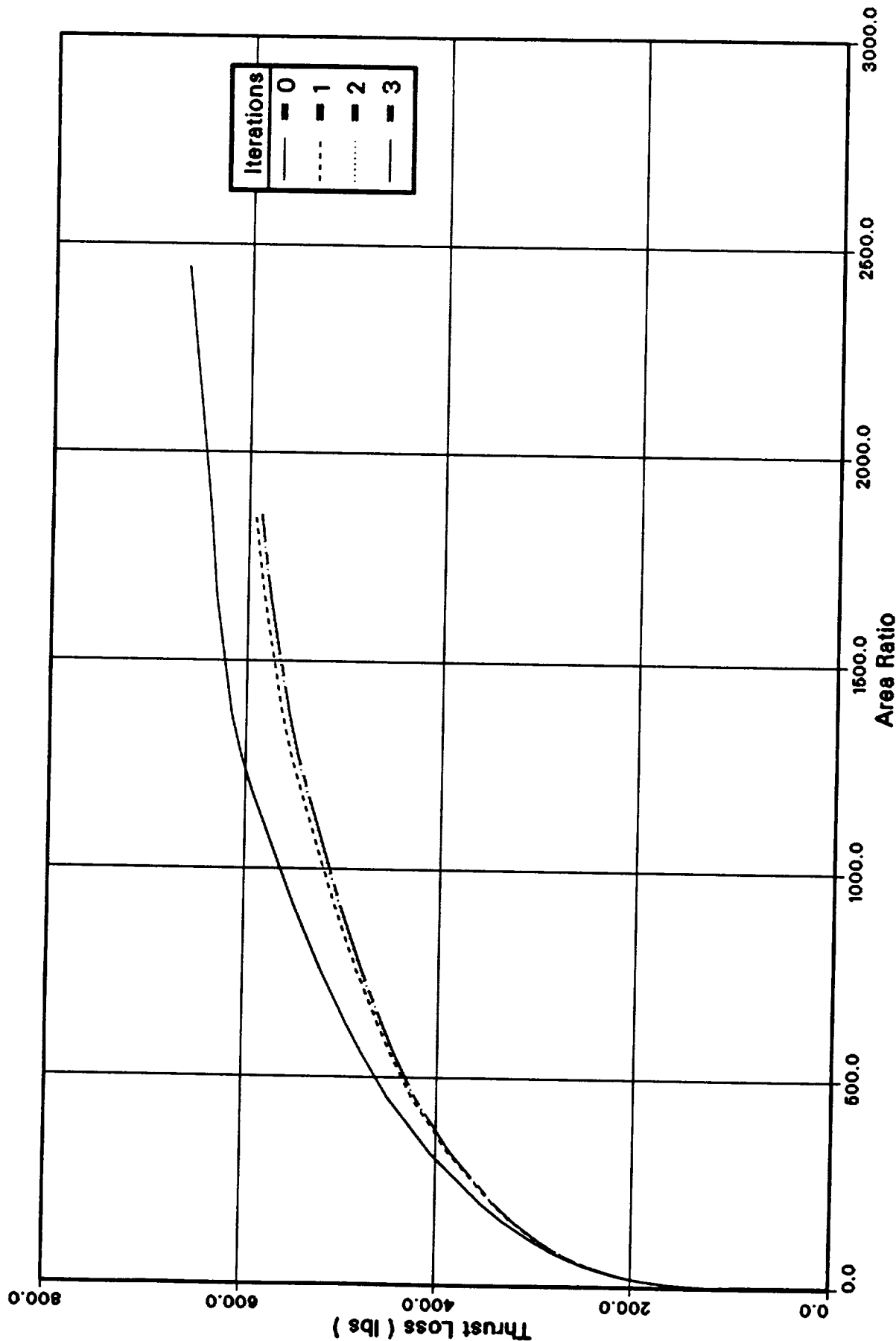
Figure 5.17: Thrust Loss Iterations for Extended OTV Nozzle

Extended OTV Nozzle
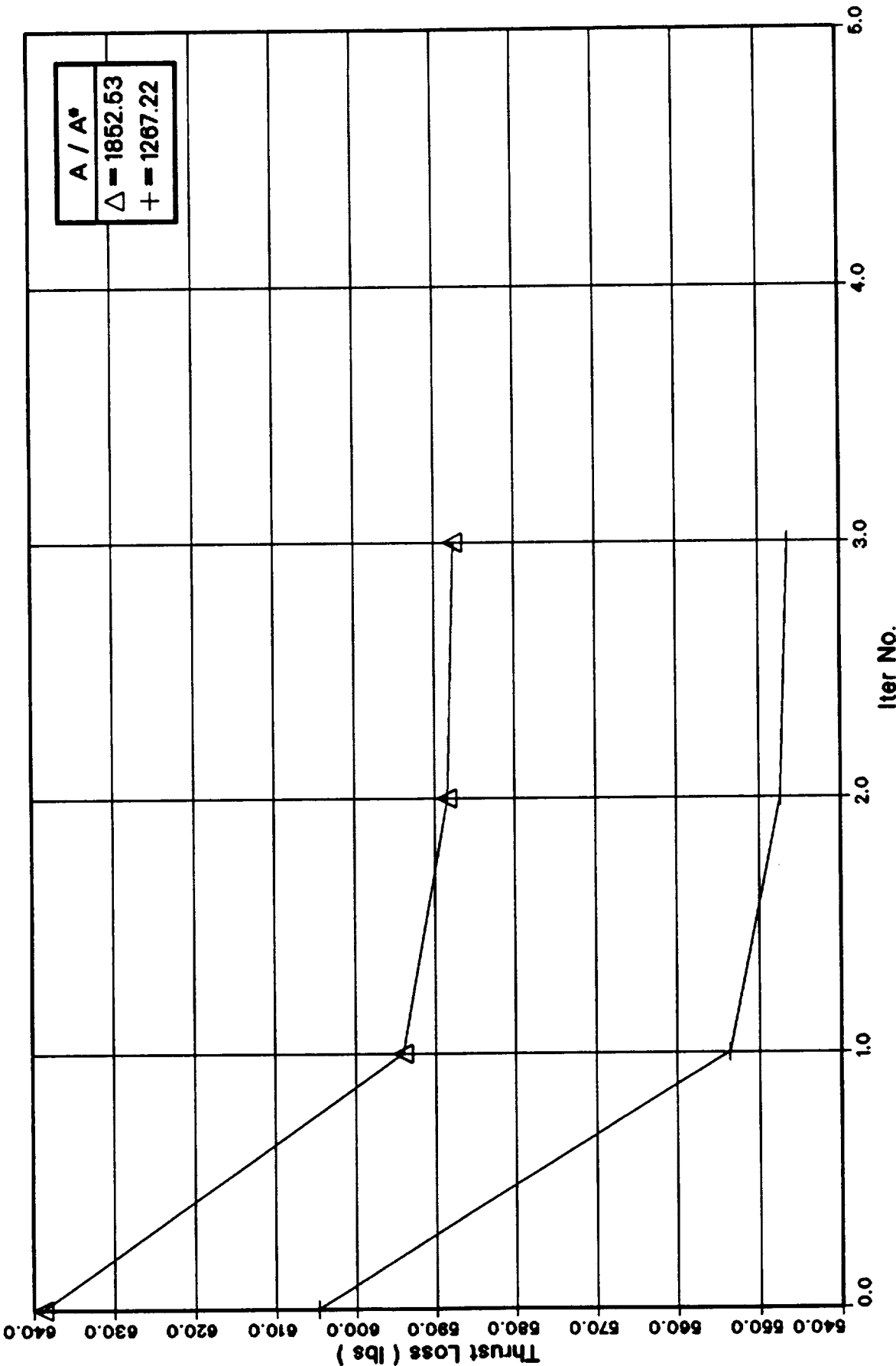
Figure 5.18: Thrust Loss Iterations at Specific Stations

Extended OTV Nozzle
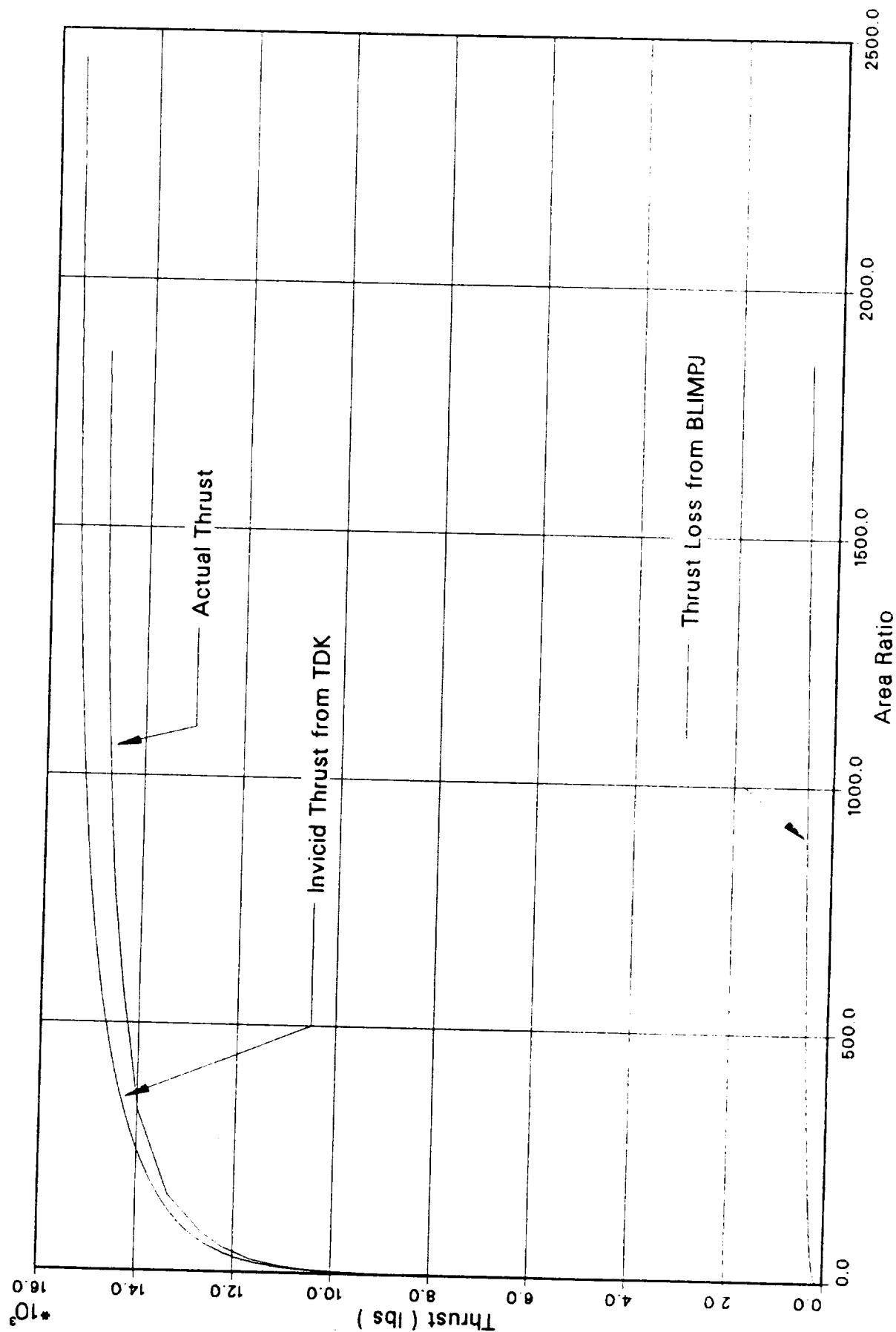
Figure 5.19: Thrust vs. Area Ratio for Extended OTV Nozzle

Extended OTV Nozzle
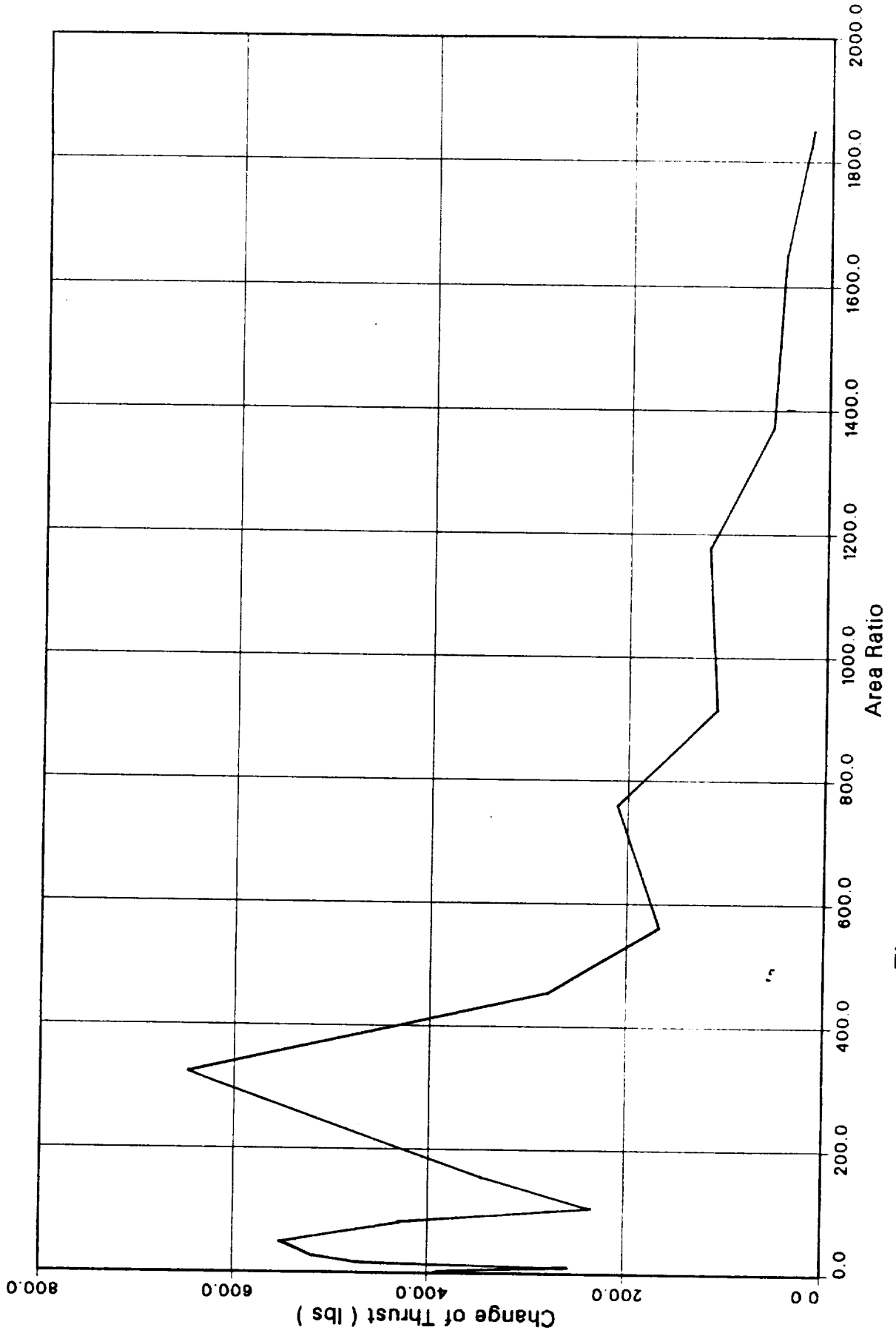
Figure 5.20: Change of Thrust from Station to Station

Section 6

EXPERIMENTAL FEASIBILITY STUDIES

6.1   Background

It is the opinion of the authors that the boundary layer flow in liquid rocket engines has not been adequately investigated experimentally to make available flow field data of good quality for guiding code development and for code evaluation for this class of flows. In the region close to the nozzle wall, viscous effects are significant. The losses due to the momentum decrement at the wall because of viscous effects are referred to as *boundary layer losses*. These can be calculated by using such codes as Boundary Layer Integral Matrix Procedure - JANNAF Version (BLIMPJ) and Boundary Layer Module (BLM). Systematic measurements to verify the calculated boundary layer losses hardly exist, and the ones that exist are associated with a high degree of uncertainty. Therefore, experimental data of high quality suitable for boundary layer code validation in such applications as the effects of wall surface roughness, relaminarization, solid particles in the boundary layer, and thick boundary layer effect in high area ratio nozzles such as those being considered for the future Orbit Transfer Vehicle (OTV), are currently needed. The objective of this effort is to provide basic considerations for measuring boundary layer losses and to guide the test engineer in selecting the appropriate type of test, the parameters to be measured, necessary test facility, and required instrumentation with associated operation complexity.

The first section of the experimental feasibility studies focuses on identifying the potential measurements which directly relate to parameters in the input or output of the relevant computer code, the relationship between the measurement and associated parameter, direct measurement, if possible, and measurement location in the thrust chamber. Measured parameters needed for data interpretation are vacuum thrust, flow rates, pressures, enthalpies, compositions, temperatures, velocities, and turbulent quantities. These parameters are usually combined into meaningful performance parameters such as specific impulse (I_{sp}), exhaust properties and boundary layer properties. The above information has been summarized in charts and tables to make it easily accessible. The recommendations given here are based on the ideas given in Ref. [26]. Considerations were given to cold flow, hot flow, reactive flow, scaled model, full size configuration, small or large area ratio nozzles, hot wall, controlled heat transfer, etc. The results from these tests

will provide the best data for verification of the analytical model.

6.2 Identification of Potential Boundary Layer Measurements

Both the data analyst and the test engineer must realize that the parameters of interest may not always be measured directly, but instead may be measured indirectly and related to the parameter through an analytical procedure. It should further be noted that the parameters of interest cannot always be measured directly at the location of interest. In the case of boundary layer losses, they could be measured directly by probing the boundary layer, thus providing an alternative to quantify the boundary layer losses.

The boundary layer losses in the thrust chamber are a result of losses in the available thrust caused by transfer of momentum and heat to the wall. In most rocket engines, these losses are more significant than the other losses described in Ref. [26]. Especially in engines, which utilize high area ratios to achieve a higher specific impulse, these losses might even be a higher percentage of the total losses.

In order to characterize the losses, it is necessary to gain insight into such aspects as the flow field, heat transfer, mixture ratio, gas composition etc. in the thrust chamber. The various parameters used in the boundary layer code, both in its input and output sections, could be measured. If direct measurements of these parameters are not possible, then certain related measurements should be made, and the parameters determined from the measurements via appropriate analytical procedures.

In order to understand the flow field and chemistry of the hot gas in the nozzle boundary layer, several auxiliary measurements are usually made. In addition to making direct thrust measurements, other quantities such as mixture ratio, combustion chamber pressure, total enthalpy, wall temperature, pressure distribution along the wall and geometry of the thrust chamber, which simulate the input parameters to BLIMPJ; and such quantities as heat transfer to the wall, velocity and temperature profiles in the boundary layer, turbulence in the boundary layer, and exhaust gas composition, which simulate the output of BLIMPJ, need to be measured.

Potential errors in measurement are indicated when:

- Wall temperature measurements are significantly different from predictions.

- Wall heat fluxes are significantly different from BLIMPJ predictions.

- Total heat load from the boundary layer is significantly different from BLIMPJ predictions.

- Boundary layer composition, temperature, pressure, and velocity profiles normal to the wall are significantly different from BLIMPJ predictions.

- The measured boundary layer thrust (or I_{sp}) loss is quite different from BLIMPJ math model predictions.

When these discrepancies are indicated in the measurements, the sources of error may lie in:

- Computation of wall temperature profile

- Starting point of the boundary layer

- Non boundary layer heat losses

- Mixture ratio and mass distribution

- Gas transport table look-up properties being incorrect

- Nonuniformity of pressure in the boundary layer, as evident in thick boundary layer situations.

- Presence of chemical kinetic effects in the boundary layer

- Friction and heat transfer correlations (turbulence model)

- Engineering assumptions made in computing boundary layer losses

The updated performance code (BLIMPJ) parameters to be measured, measurements necessary to relate to these parameters and measurement locations are summarized in Table 6.1.

Boundary layer losses are a regular feature of all nozzles. It is obvious from the literature that for a moderately large area ratio nozzle, the boundary layer losses will be significant. It is expected that as the area ratio increases, these losses will also grow.

Major concerns in setting up this test are:

- Using air only at moderately high temperatures ($T \simeq 300°F$) in the chamber to avoid reaction between N_2 and O_2.

- Using an inert gas such as argon, freon, etc. which does not react when heated to a high temperature

- Avoiding nozzle flow separation

- Test duration - In short duration testing it is hard to measure thrust by a load cell. Also, it is more difficult to probe the boundary layer. In long-duration testing, however,

  1. Scaling problems are alleviated.
  2. More than one measurement per run can be made.
  3. High altitude simulation requires a very large facility.
  4. Depending on the nozzle size and test duration, cost can be a factor.

Some of the key data that can be obtained from such tests are:

- Boundary layer loss measurement

- Heat transfer effects on the nozzle wall

- Boundary layer probe measurements in the nozzle - An example is the tests by Back and Cuffel [11].

6.3   Test Facilities

The validation of the turbulence models suggested in this report against measured data would make them very powerful for future rocket nozzle design. Table 6.2 gives a short list of test facilities available around the country which may be used for reactive full-scale or sub-scale nozzle flow testing.

The roughness model was validated in this report against data measured with the 60°-15° half angle conical nozzle and gave reasonable correlation. However, problems remain with the validation at the nozzle throat region. The full-scale or large-scale reactive firing engines as shown in Table 6.2 are not easily tested for wall roughness, whether uniformly or variably present in the nozzle. A laboratory experiment with hot gas (preferably air) as the flowing medium and with multiple nozzle geometries containing roughness must be designed to fully test the turbulence models. In addition, a variety of roughness elements with a variety of roughness densities, which provides a range of "equivalent sand roughness," should be implemented for a complete validation.

A similar argument is also put forward to test the relaminarization module. The relaminarization module developed by Nash-Webber [12] was very extensively tested at the MIT Gas Turbine Laboratory. He used variable nozzle geometries to create the required acceleration parameters. Unfortunately, he used only adiabatic wall conditions, thus giving only a partial answer to a very complex problem. The combined effects of roughness and relaminarization were tested by Reshotko et al. [6], whereas some relaminarization effects were observed by Back and Cuffel [11]. Again, laboratory-type experiments are suggested to thoroughly and systematically quantify the effects of high acceleration parameters on wall heat flux and skin friction. A set-up like that of Nash-Webber where a variety of acceleration parameters were imposed by using a flexible-wall nozzle contour is suggested.

The turbulence model to include the effects of particle presence in the boundary layer is far from complete since hardly any validating tests exist in the literature for rocket nozzle flows. Particle generators producing known-size particles need to be designed. The particulate concentration needs to be measured in the boundary layer using the available optical technology to enable the engineer to validate against measured data.

The thick boundary layers which affect the nozzle performance may best be measured in the altitude test facility at LeRC [27] and other facilities to quantify the thrust decrement for comparison with computations. The details of the boundary layer flows, however, must be measured in laboratory experiments using LDV, fiber-optics and other available non-intrusive systems, or using conventional probes.

Table 6.1: Boundary Layer Losses

Parameters in Boundary Layer Code	Potential Measurements Relating to the Parameters and Boundary Layer Loss	Relationship between Measurements and Parameters	Location
INPUT PARAMETER			
Mixture ratio – O/F	Cold flow tests (Conventional)	Same as parameter	Mixing region aft of injector
Combustion chamber pressure, P_C	Combustion chamber wall pressure	Simplified method for P_C, given in Ref. 1	Combustion chamber wall
Edge gas total enthalpy, H_o	Raman scattering techniques	Combustion temperature equal to edge gas temperature and temperature related to enthalpy	Combustion chamber
Wall enthalpy, H_W	Wall temperature and C_p from thermocouple tables	$H_W = C_C T_W$	Nozzle
Gas transport properties	Not measured – JANNAF tables	Used in BLIMPJ	—
Pressure distribution on the wall	Wall pressure	Same as parameter	Nozzle wall
Geometry of the thrust chamber – combustion chamber, converging/ diverging nozzle	Drawing; measured area for either short or long duration testing	Same as parameter	—
Wall roughness, if present – may also develop in the whole or parts of the chamber wall while in operation; equivalent sand roughness	Roughness density, roughness profile data	Same as parameter; equivalent sand roughness is related to roughness parameters by expressions given in Ref. 4	Nozzle wall
Particle or condensation (two-phase) effects – particle size	Particle density and particle size	Same as parameter	Particle generator and nozzle exit plane

Table 6.1: Boundary Layer Losses (Concluded)

Parameters in Boundary Layer Code	Potential Measurements Relating to the Parameters and Boundary Layer Loss	Relationship between Measurements and Parameters	Location
INPUT PARAMETER			
Mass flow rate through the nozzle throat	Feed system measurements	Calculated from the feed system measurements	Feed system
Heat transfer rate at the wall	1. Thermocouple measurements 2. Heat transfer gage 3. Phase change 4. Calorimetric measurements	1. Thin-skin or thick-skin relationship 2. Same as parameter 3. Time-dependent 4. Temperatures related to heat transfer rate	Nozzle wall
Velocity and temperature profiles in the boundary layer	Fiber optic based LDV	Same as parameter	Nozzle boundary layer profiles
Turbulent length scale and turbulent shear stress variation in the boundary layer	LDV	Turbulent fluctuation quantities related to Reynolds shear stress by standard methods. From this shear stress, by length scales can be derived and compared against BLIMPJ turbulence models	Nozzle boundary layer profiles
Exit plane velocity	Fiber optics	Same as parameter	Nozzle exit plane
Exhaust gas temperature composition	Nonintrusive studies such as radiometric	Calculated from radiometric measurements	Nozzle exit plane
Thrust loss	Load cell (strain gas measurement)	Thrust loss = ideal thrust - measured thrust	—
ISP loss	Thrust loss and mass flow rate	Δ ISP $= \Delta T / \dot{m}_T$	—

Table 6.2: Representative Existing Test Facilities

Facilities	Test Set-Up	Advantages and Limitations
NASA LeRC Rocket Nozzle Test Facility (RETF)	• Diffuser provides pressures from 0.03 to 0.05 psia	• Altitude simulation possible • 1030 Area Ratio Nozzle • Area Ratio Variable – Flanged Joint existing at 430 area ratio • Another nozzle with 1.4 area ratio also exists.
Engine Test Facility at MSFC	• SSME Nozzle • Subscale	• Fixed Nozzle Geometry – SSME • Altitude Simulation not possible
Engine Test Facility at AEDC		• Altitude simulation possible • Very expensive facility

Section 7

INSTRUMENTATION

7.1 Background

The previous section dealt with the measurements necessary for verification of the boundary layer code, BLIMPJ. These measurements will be useful only if the accuracy of the measuring instruments is within the required range. The document prepared by Praharaj and Palko [26] identified the various instruments, most of which were intrusive in nature, and gave typical manufacturer specification and their quoted accuracies. While selecting an instrument, the cost vs. accuracy tradeoff must always be considered. Either cost or accuracy may be compromised depending on the objective of the test. This section deals with both dynamic and static measurements. The dynamic measurements include velocity vector, turbulent quantities, pressure, temperature, and species concentration. These measurements are made with LDV systems, fiber optic sensors and laser Raman scattering technique. On the other hand, the static measurements, which are mostly intrusive in nature, have been described in detail in Ref. [26] and will be only summarized here.

7.2 Dynamic Measurements

7.2.1 Velocity Vector and Turbulent Quantities

7.2.1.1 2-D and 3-D Laser Doppler Velocimeter Systems

The most common scientific application of laser instrumentation is as a Doppler velocimeter in studies of fluid dynamics. The principle of this technique is based on the detection of the "Doppler" shift (named after the Austrian physicist who first considered the phenomenon in 1842) of laser light scattered from small particles moving with the medium (either natural or added) by a stationary photodetector. The technique has the potential of complete linearity between transducer response, which is directly related to Doppler frequency shift, and the particle velocity. In contrast, other transducers, such as the hot-sensor and the pitot-probe systems, are only approximately linear within limited ranges. The major advantages of the laser Doppler velocimeter are:

- It does not disturb the flow since no physical probe is inserted into the measuring medium.

- It is not subject to damage by fluid environment.

- No flow calibration required, no drift.

- It has high spatial and temporal resolution with fast response.

- Instantaneous multi-component, bi-directional measurements can be made.

- Operation is not affected by temperature, density and composition changes in the fluid.

For the measurement of fluid velocity dynamically, the hot-sensor (hot-wire or hot-film anemometers) performs less well in highly fluctuating flows, particularly at low mean velocity. The sensitivity of the sensor to more than one velocity component causes measurement errors that are not easily compensated. The measurement of reversing flow velocities, of course, cannot be detected with a single probe. These problems may in principle be eliminated by employing moving hot-sensors which is the equivalent of the frequency shift in laser Doppler velocimeter systems. However, the method still implies insertion of a probe into the flow, and the flow disturbances can introduce serious errors, especially in the measurement of thin boundary layers and fluctuating components of fluid velocity.

Although the laser Doppler velocimeter technique is a very powerful research tool, it is not a general replacement for other techniques, since optical access is not always possible or available, and the equipment for the system is expensive. The laser Doppler technique has, however, proven to be valuable in study of separated flows, variable property flows, flows within blade rows in rotating machinery, low velocity flows, liquid flows, combustion and flames, high turbulence intensity flows and flows with recirculations.

In considering the laser Doppler velocimeter technique for flow measurements, conditions under which the measurements are carried out need to be fully considered. Also, it is of vital importance to know whether the system will satisfy the measurement requirements, or what the optimum system needs to be in order to meet all the requirements. The prime concern should be focused on the flow measurement region and its accessibility for laser beams either through optical windows or through transparent sections.

To study the flow problem in a subscale rocket engine, a two-color, three-component, dual-beam, Bragg-diffracted (vectorized) laser Doppler velocimeter (LDV) system (Fig. 7.1) may be utilized. This system can be developed based on

the complexity of internal viscous flow and the fluctuating fields in the rocket's combustion chamber and nozzle. The system arrangement for the LDV consists of six major subsystems: the light source, the optical system, the traversing mechanism, the particle generator, the signal processor and data processor. For details of these and other items, references such as [28], [29] and [30] may be used. The associated measurement errors are discussed in the following paragraphs.

At the present stage, the value of the laser Doppler velocimeter as a useful measuring technique is well established. The applicability of the system to widely different flow problems shows the potential capabilities of the technique. However, as with any flow diagnostic tool, the laser Doppler velocimeter system can introduce some uncertainties and errors into the measurement. In general, the potential sources of measurement error may be categorized into five areas: (1) Optical system errors, (2) multi-measurement biasing, (3) signal processing measurement errors, (4) aerodynamic uncertainties, and (5) statistical uncertainties. For completion of the 3-D LDV system analysis all these error sources are discussed and ways that were taken to avoid or correct them are presented in this section.

The optical system errors consist of the cross beam angle measurement uncertainty and the uncertainty in the parallelism of the fringes in the measuring control volume. The uncertainty in the measurement of the intersection beam angle is dependent upon the precision with which the angle is measured. The fringe distortion occurs when two Gaussian beams do not intersect at the waist (the location of the narrowest part of the beam). If the beams intersect correctly in the waist region, the fringes are truly parallel, but when the intersection occurs before or after the waists, a set of diverging fringes is generated. In this case, particles passing through the control volume perpendicular to the optical axis, but at different positions will produce Doppler signals of different frequency even if their velocities are identical. Thus, the degree of parallelism of the fringes is dependent upon the distance between the focal point of each Gaussian laser beam and the probe volume location.

The multi-measurement biasing is due to the Bragg bias error, which is based on the fact that since the Bragg cell causes the fringe pattern to move in the probe volume, it is possible to obtain multimeasurements from the same seed particle as it passes through the volume. However, this bias can be eliminated by using a Bragg cell, the frequency of which is large compared to the signal frequency and also, by time averaging rather than particle averaging of the data. Another possible error due to the Bragg cell is the detection of directionality in the velocity measurements. At points in a flow where particles can occasionally cross the control volume in a negative direction, the stationary-fringe LDV measurements will be biased since the sign of the velocity cannot be distinguished in a stationary-fringe system. This

negative velocity biasing can be corrected by using a moving-fringe vector (Bragg diffraction) LDV system.

The measurement errors due to the burst counter processor include filter cut-off bias and incomplete signal bias. Filter cut-off bias is based on the realization that when the signals from some moving particles in the measuring volume are lost due to filters in the processing system, the set of measurements will be biased because all lost signals will be at one end of the velocity histogram. This error can be reduced if the counter type processor is built with wide frequency response. Incomplete signal bias is due to the particles which pass through the probe volume without crossing the required number of fringes. Since these particles have low velocity components and sometimes zero velocities in the measured direction (normal to the fringes) their rejection by the processor will result in a biased set of measurements. However, this bias can be easily eliminated by using a vector LDV system. There are other possible electronic error sources such as clock synchronization error which is due to the timing mismatch of the signal frequency and the reference clock, quantizing error and truncation error that should be considered in the flow measurements.

The aerodynamic uncertainties due to particle response to the flow field consist of uneven seeding bias, multiple particle bias, and particle acceleration bias. Uniform distribution of particles throughout the flow is essential for correct and successful measurement of the fluid velocity distribution at a point. Nonuniform particle size distribution in the flow can introduce some errors in the measured mean-velocity because the large particles normally do not follow the flow as well as small particles (particle lag). Furthermore, as the seeding density increases there is a possibility that more than one particle will tend to traverse the probe volume simultaneously. Thus, the signal from first particle is more likely to be rejected (while it is being processed) because a second one has entered the probe volume and therefore the set of measurements will be biased. These error sources can be nearly eliminated if a properly designed laser seeding generator is used and also by using a signal validation circuit in the counter type processor which is capable of rejecting signals from multiple particles and signals from highly accelerating or decelerating particles in the probe volume.

Statistical uncertainties need to be considered since the measured quantities (e.g., mean, standard deviation, etc.) are statistically determined from an average of velocity measurements. In nozzle flow investigation, all statistical errors can be removed by applying a time-averaging method where all the data are weighted by the amount of time elapsed between each particle arrival. This requires that time as well as velocity data be taken.

7.2.1.2   Fiber Optic Based Laser Doppler Velocimeter System

Currently, there is a strong demand for reliable experimental data to evaluate the important parameters used in describing and predicting the nozzle flow behavior. A better understanding of the mechanisms occurring in the viscous nozzle flows will allow practicing engineers to optimize and/or design more efficient thrusters. Detailed studies of the nozzle flow require suitable measuring techniques to provide practical information of interest. Measuring techniques which require sampling probes to be located at the measuring point are unacceptable in the nozzle because they may result in unwanted disturbance and possible sample errors. The employment of non-intrusive methods, such as the noncoherent light and sound waves directed across the flow field, can only provide integral information which is difficult to interpret since strong variations can occur along the light or sound paths. Due to these difficulties, optical methods based on laser and fiber techniques seem very appealing to determine the nozzle flow characteristics.

To satisfy the above requirements, an advanced two-component laser Doppler velocimeter system and fiber optic sensors are proposed to be designed and developed for simultaneous measurements of two-dimensional local velocity vector, pressure, and temperature in the nozzle flow fields. These measurements are expected to provide accurate and valuable information about the nozzle flow fields.

The application of the laser and fiber optics to measurements in a highly complex flow such as the combustion chamber or nozzle of a rocket engine, requires innovative approaches due to the constraints inherent in the measurement technique. The laser velocimeter concept allows for the measurement of gas dynamic velocity by the sensing of the Doppler shift in laser light that has been scattered by particles moving with the gas. The measurement is direct in that the particle velocity and Doppler frequency shift are proportional to each other. The proportionality constant consists of the laser wavelength, λ, and the geometrical orientation of the laser velocimeter optical system or the angular relation between the incident laser light and the scattered light. Fiber optic sensors offer several significant advantages over conventional sensors. Their high sensitivity and exceptional signal-to-noise ratios can deliver performance more traditional approaches cannot match. They offer geometric flexibility and immunity to electromagnetic interference and hostile environment conditions. Fiber optic sensors of many types can be developed. Generally, they are categorized as amplitude- or phase-modulated optical devices. While some fiber sensors are highly sophisticated, others are elegantly simple. Regardless of their complexity, they all employ similar components and utilize common operating principles. They typically exploit changes in the intensity (amplitude), polarization or phase of light propagating in the fiber. Subtle perturbations of the geometry, length or refractive index of a fiber or coupling

REMTECH

between fibers can provide innovative ways to measure physical phenomena such as velocity vector, temperature or pressure. Thus, the basic measurement requirements for the laser Doppler velocimeter and fiber optic sensors are: (1) a coherent light source such as a laser with sufficient power to shine light into the measuring field of interest, (2) the transmitting (focusing) optics to transmit and direct the laser beams into a small and well-defined measurement region or probe volume, (3) the receiving optics to collect the scattered light generated by the natural or artificial particles present in the flow and direct it to the signal detectors, (4) single-mode or multimode optical fibers, (5) photodetectors with sufficient signal gains to convert coherent light signal to electrical signal, (6) a signal processor to convert the electrical signal to a voltage proportional to velocity, temperature or pressure, and (7) a computer or other similar data reduction system to allow for computation and/or analysis of the data for the desired information.

The optical configuration of the recommended fiber optic based laser Doppler velocimeter system is illustrated schematically in Fig. 7.2 for the nozzle flow velocity measurements. For the practical application of the laser Doppler velocimeter system, a small and low-cost, commercially available, air-cooled He-Ne laser, which delivers 30 mW of stable power output, can be used as a light source. The laser emits a red light of 632.8 nm wavelength and operates in the uniphase TEM_{00} (Transverse Electromagnetic Mode) having a Gaussian radial beam profile. A beam collimator is used to control the beam divergence for the LDV optical system. In order to measure the two orthogonal components of local velocity in the same probe volume simultaneously, it is necessary to generate two superimposed sets of interference fringes. This is accomplished by applying the dual-beam optical frequency preshifting technique and employing a single two-dimensional ultrasonic Bragg cell modulator as shown in Fig. 7.2. The Bragg cell functions as both the beam splitter and the frequency shifter. The collimated laser beam is passed into the Bragg cell's optical quality window and four equally intense beams are produced. The two red pairs of beams operating at a single wavelength (632.8 nm) are frequency shifted by the Bragg cell driver with carrier frequencies of 25 and 15 MHz representing the x- and y-components of velocity vector, respectively. Thus, frequency differences in orthogonal beam pairs are 15 and 25 MHz. The four parallel red beams then are focused to a common measuring point by a set of achromatic transmitting lenses. The common measuring point of probe is composed of two superimposed sets of interference fringes as shown in Fig. 7.3. The interference fringes are produced by the intersection of the two pairs of vectorized laser beams where each region of intersection is used to measure one orthogonal component of velocity. Two photodetectors are employed to convert the collected scattered light into an electrical signal. A block diagram of the signal processing electronics is presented in Fig. 7.4.

The fiber optic LDV system, shown in Fig. 7.2, can be used for the nozzle flow measurements in small or restricted spaces. The system is immune to electrical noise and reduces the potential for damage to the laser from hostile measurement environments. The fiber optic probe can be positioned inside or outside the flow and maneuvered easily using a simple traversing arrangement. Because the probe is highly maneuverable, the measuring volume can be repositioned simply by moving the probe, rather than by moving the complete LDV system.

7.2.2 Pressure and Temperature

7.2.2.1 Fiber Optic Pressure Sensor

A simple and rugged fiber optic sensor based on a reflecting Fabry-Perot interferometer for the remote measurement of the nozzle or combustion chamber pressure is shown in Fig. 7.5. The system consists of one fixed mirror and a second mirror which moves under the action of the pressure being monitored. A single multimode fiber is used to connect the passive, remote sensor to the transmitter/receiver section. The potential advantages of fiber optic pressure sensors over conventional types are well known and include: immunity to electromagnetic interference, intrinsic safety in hazardous environments due to their electrically passive nature, and the convenience of remote sensing over low attenuation optical fiber.

7.2.2.2 Fiber Optic Temperature Sensor

Figure 7.6 shows the configuration of a radiometric temperature measurement using infrared optical fibers. A combination of an optical fiber and a radiometer permits remote temperature measurements in the rocket engine environments. Energy emitted from the measuring point is focused by a lens onto one end of an IR fiber, transmitted through the fiber, and detected by a remotely located IR detector. The function of the detector is to convert the detected radiation energy into an electrical signal.

7.2.3 Species Concentration and Temperature

7.2.3.1 Laser Raman Scattering Technique

The laser velocimeter inherently provides velocity vector and associated turbulent quantity information. The Raman technique provides measurements of local static density (species concentration) and temperature and is not flow direction

sensitive. Both techniques offer local "point" measurements. Combined, these techniques offer the potential of local nondisturbing simultaneous measurements of the three basic gas parameters, i.e., velocity, density, and temperature, necessary to define the thermodynamic state of the fluid.

When a beam of monochromatic light traverses a gas mixture, the resultant scattering phenomenon involves both the elastic and inelastic interactions of the photons with the gas molecules. The elastic interaction results in Rayleigh scattering, whereas that caused by the inelastic interaction results in Raman scattering. The Raman scattered radiation consists of radiation in which the energy, and therefore, the frequency, has been changed by an amount characteristic of the energy differences between the stationary energy states of molecules it encounters. The shift can result in an increase in energy, and subsequent increase in frequency (Anti-Stokes Line), or a decrease in energy and subsequent decrease in frequency (Stokes Line), of the scattered radiation. This frequency shift is a unique characteristic of the scattering molecules and is independent of the frequency of the incident radiation. Therefore, the individual species present in the gas mixture can be uniquely distinguished by monitoring the frequencies of the scattered radiation. Not only can one distinguish between the different species comprising a gas mixture, but, by measuring the intensity of each component of the scattered light one can determine the temperature and concentration of each diatomic or polyatomic species in the mixture.

Excitation at both the Pump frequency, W_L, and the Stokes frequency, W_S is required, necessitating the use of the laser sources. Since Raman spectra are obtained by scanning the difference, $W_L - W_S$, one of the two lasers must have frequency-tunable output. Since the CARS (Coherent Anti-Stokes Raman Spectroscopy) signal scales as $P_L^2 P_S$, high laser powers are desirable and pulsed lasers are almost always used in CARS. Fairly tight focusing, 50 to 200-μm-diameter spot size, of the laser beams also is generally used.

7.3   Static Measurements

7.3.1   Wall Pressure and Temperature

There are three sets of static measurements desired in the combustion chamber and nozzle of a rocket engine during a reactive test: (1) pressure distribution, (2) temperature distribution, and (3) heat transfer rate. Numerous details of various sensors are given in Ref. [26]. The most important of these sensors are discussed below.

The combustion chamber pressure can vary from 10 psia to 5000 psia depending on the type of rocket engine and fuel used, and the location of the pressure orifice can vary from behind the injector face to near the nozzle throat. For a hot gas simulation test, the pressure should be measured at several locations along the chamber wall starting just aft of the injector face and ending just forward of the start of contraction. The specifications for a series of high accuracy pressure transducers that cover the range of normal combustion chamber pressures are given in Fig. 7.7. The measurement of the combustion chamber temperature during the hot gas simulation testing can be made with a standard high temperature probe of similar design as those used in the stilling chamber of a hypersonic wind tunnel where temperature measurements of 1500°F may be required. Another option is a sapphire black body optical fiber thermometry system that has an accuracy of 0.2 percent at approximately 4000°R. The specifications for this probe are given in Fig. 7.8.

The nozzle design for the hot gas simulation model should be such that static pressure orifices and thermocouples can be located along the nozzle wall starting as near the throat as possible and continuing at moderate intervals to the exit. The specification for a pressure scanner that could be used to measure the nozzle static pressures is given in Fig. 7.9. This particular pressure transducer system quotes an accuracy of ±0.10 percent on full scale. Normally chromel-alumel thermocouples are used for the temperature measurements, although most of the basic thermocouple types could be used. The temperature measurements could also be measured using the optical fiber thermometry system as shown in Fig. 7.8. The accuracy of the temperature measurements is normally the accuracy of the curve fit used to convert the thermocouple millivolt output to degrees.

7.3.2 Heat Transfer Rate

The heat flux can be obtained from calorimetric measurements by measuring the chamber coolant temperature (cryogenic fuel when used as the coolant or water in the case of hot gas simulation) at various stations along the coolant passages and then using the ΔT of the coolant, mass flow of coolant, and C_p for coolant from a thermodynamic table to calculate the heat flux. Since the heat-transfer rate along the nozzle wall is one of the output parameters in the boundary layer code, it is very desirable to have an accurate measurement of this parameter. It would be difficult to measure the heat transfer rate using the thin skin technique and it is difficult to determine the accuracy of the calorimetric method, therefore, it would be better to design the hot gas simulation model so that heat flux transducers could be used to measure the heat transfer rate. The specification of a heat flux transducer is given in Fig. 7.10.

7.4   Recommendations

Although the static measurements are simpler to design, less expensive and more readily installed, a combination of static and dynamic measurements should be tried. These measurements should also be made on full-scale, sub-scale and laboratory scale rocket nozzles in order to validate the appropriate turbulence models. A tradeoff of cost vs. accuracy must be considered while designing the test model and the required instrumentation. If one were starting to conduct the experimental validation of the modules coded in this report, it will be recommended to start with (1) laboratory models with static measurements and work upward with (2) sub-scale and full-scale models with static measurements, and (3) sub-scale and full-scae models with dynamic measurements.
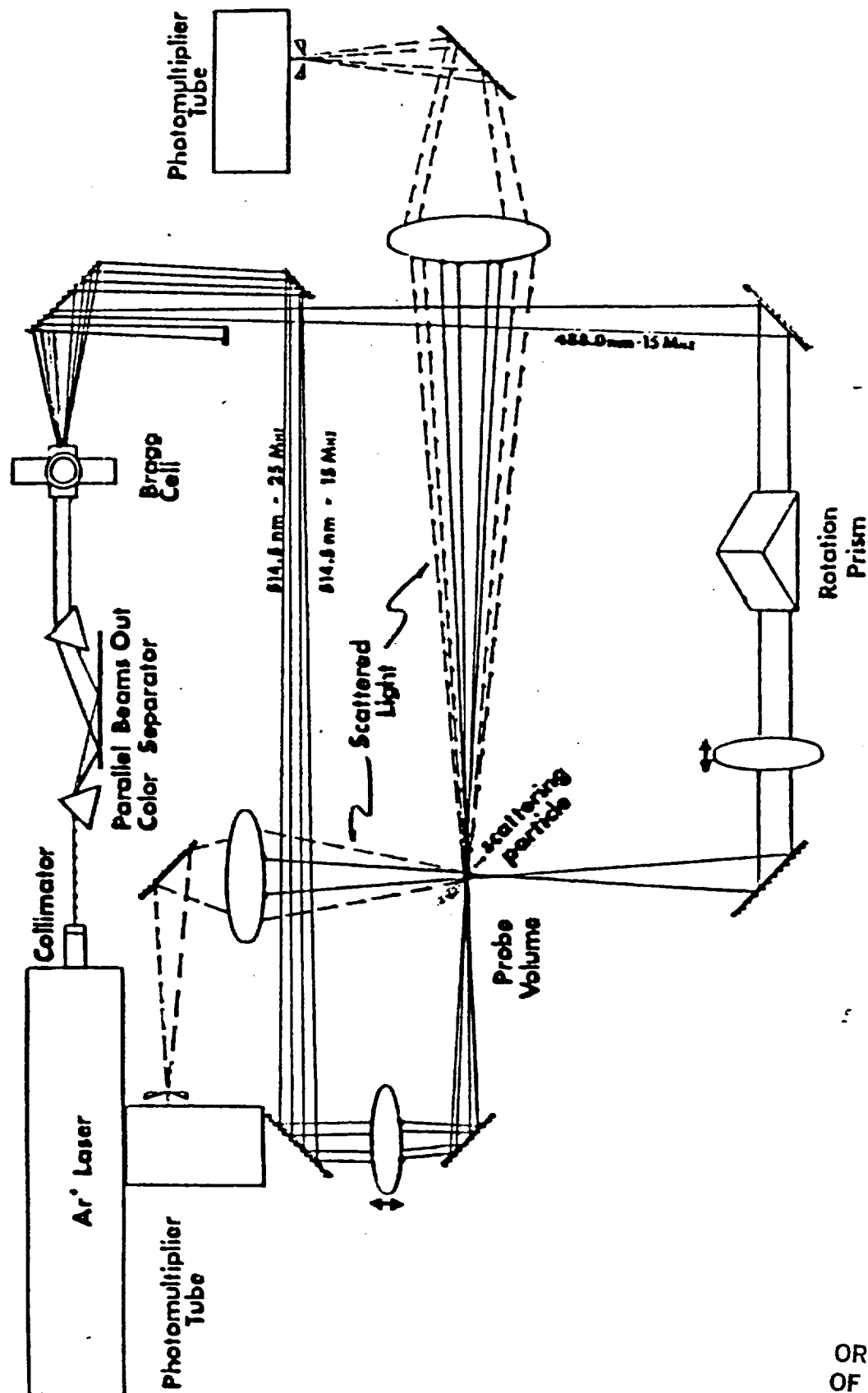
Figure 7.1: Laser Systems for Flow Field Analysis

Figure 7.2: Typical Fiber Optic LDV System for Velocity and Turbulent Intensity Measurements

Figure 7.3: Fringe Pattern in the Measuring Volume Produced by Crossing Laser
Beams in the Differential Doppler Technique and a Typical Doppler
Burst-Detector Signal

120
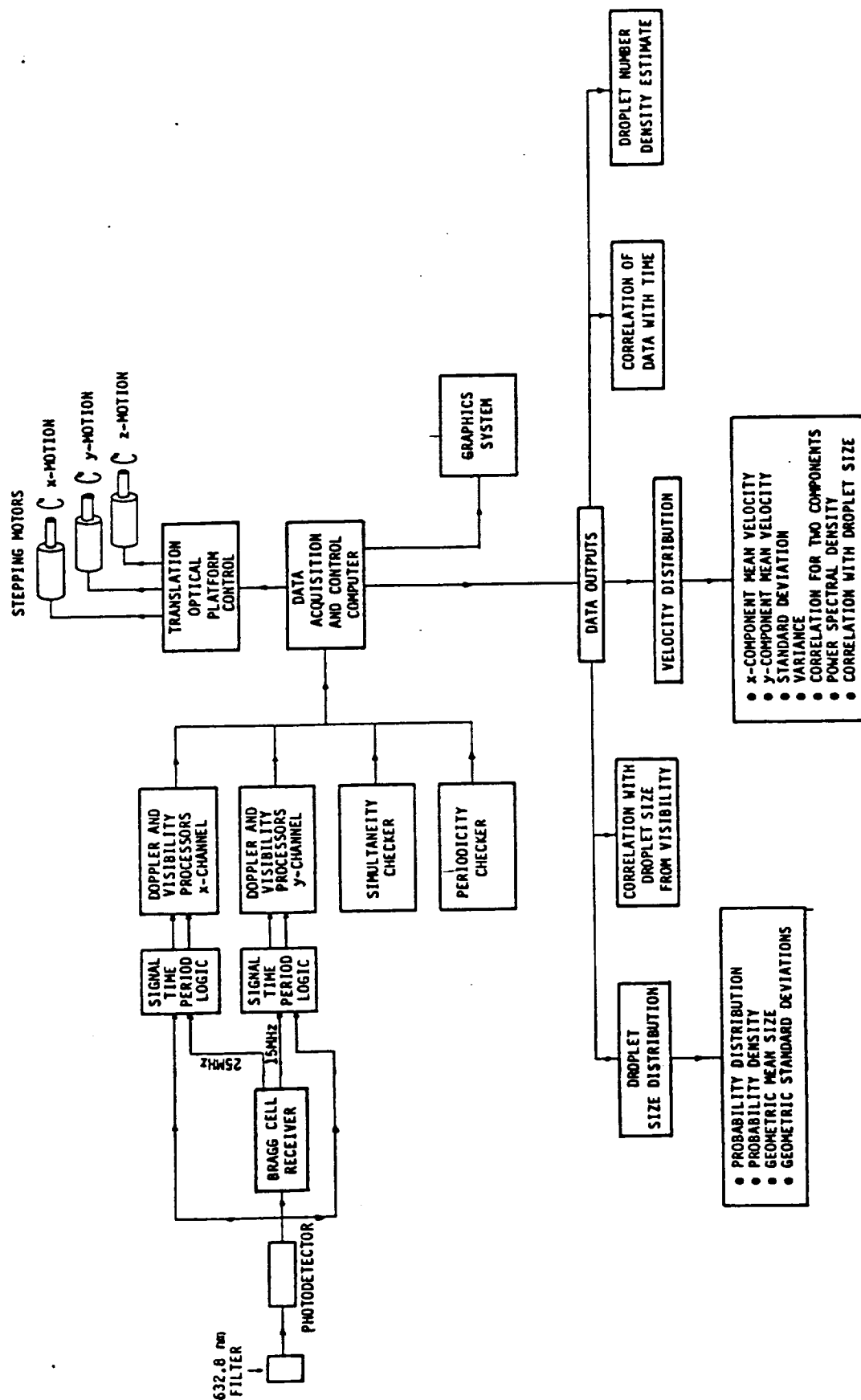
Figure 7.4: Schematic Diagram of 2-D LDI Signal Processing System for Two-Phase Flow Studies
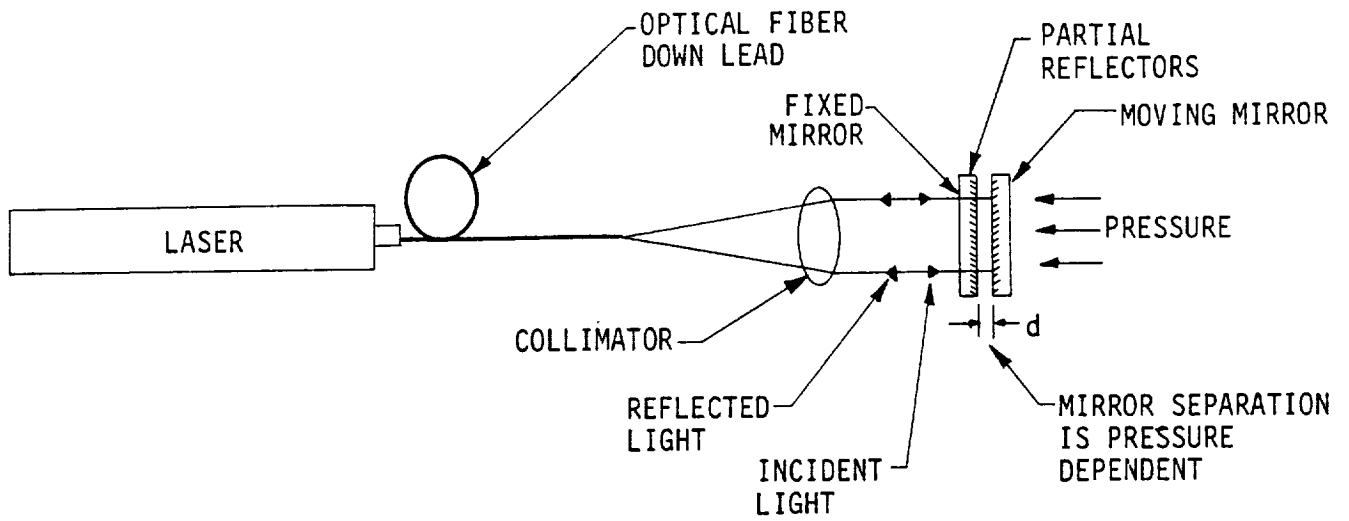
Figure 7.5: Typical Configuration of a Fiber Optic Remote Pressure Sensor
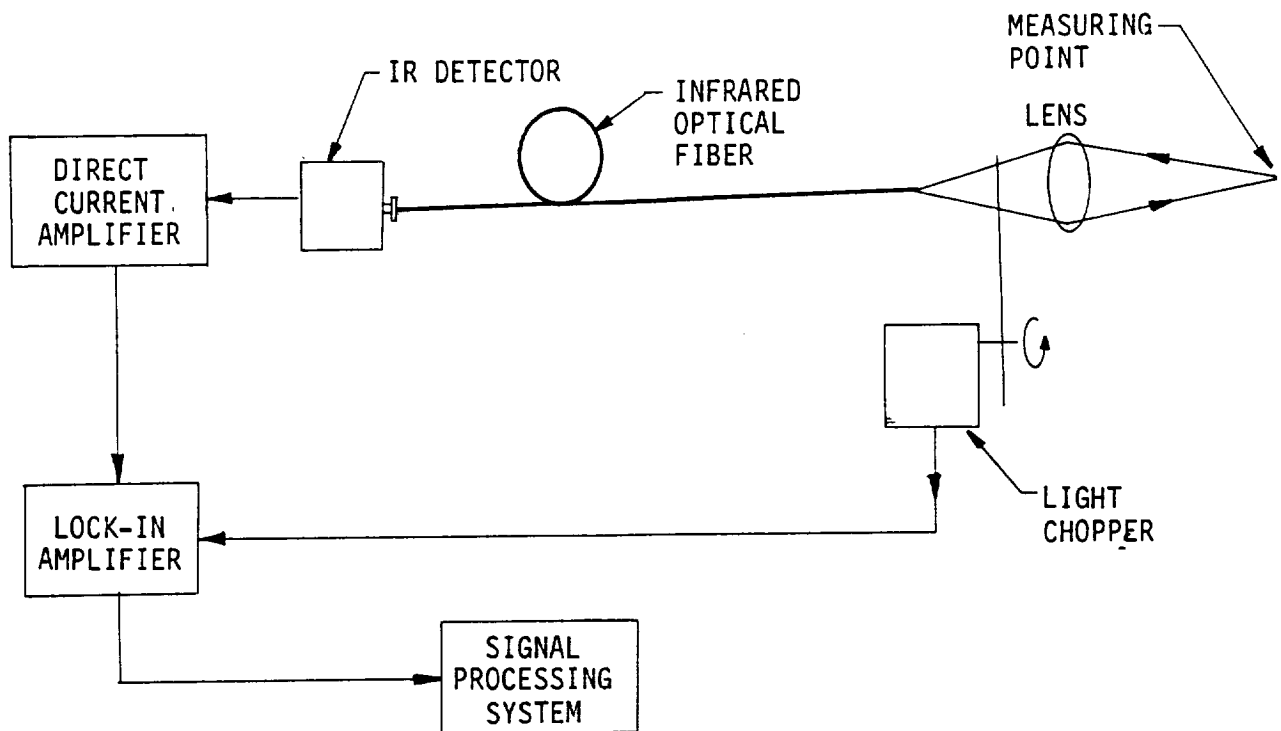
Figure 7.6: Fiber Optic Configuration for Infrared Temperature Sensing

ORIGINAL PAGE IS OF POOR QUALITY

High Output/High Accuracy Pressure and Vacuum Transducers and Transmitters
Summary of Specifications

Most Transducers and Transmitters available on GSA

Models 204, 204D, 239, 261, 280 and 280E are available as 4-20 ma output Pressure Transmitters for two-wire current loop systems.

Quality assurance: Setra's quality control system conforms to Mil I 45 208 A and Mil Std 45 662 A

Detailed Product Bulletins with complete performance and engineering specifications are available for all products described below.

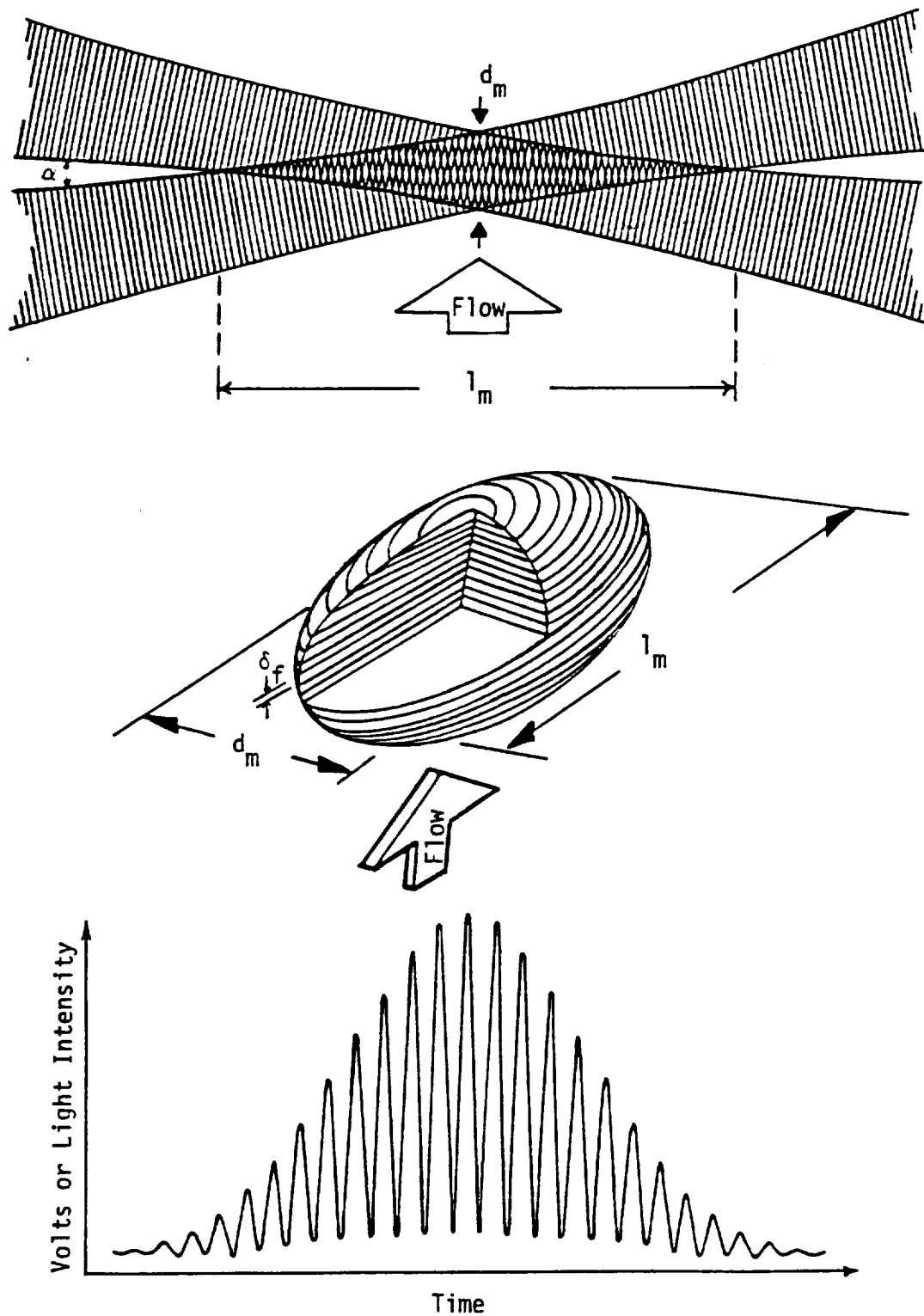| APPLICATION		204 series (204B, 204D)	205-2	280 series (280 & 280E)	239	261-1	SETRACERAM Sensor 270	SETRACERAM Sensor 271
		DIFFERENTIAL PRESSURE (204D) ABSOLUTE PRESSURE (204D) GAGE PRESSURE VACUUM (204)	ABSOLUTE PRESSURE GAGE PRESSURE	ABSOLUTE PRESSURE GAGE PRESSURE	LOW GAGE PRESSURE DIFFERENTIAL PRESSURE AND DIFFERENTIAL PRESSURE	LOW STATIC PRESSURE AND DIFFERENTIAL PRESSURE (HVAC)	ABSOLUTE PRESSURE GAGE PRESSURE	DIFFERENTIAL PRESSURE GAGE PRESSURE
Media Compatibility[2]	Pressure and Vacuum	Gas or liquid compatible with stainless steel	Gas or liquid compatible with stainless steel	Gas or liquid compatible with stainless steel	Gas compatible with stainless steel aluminum	Clean, dry, non-corrosive gas such as air	Gas or liquid compatible with aluminum, alumina ceramics, gold and fluorosilicon elastomer sealant	Gas or liquid compatible with aluminum, alumina ceramics, gold and fluorosilicon elastomer sealant
	Reference Pressure (for Differential Pressure)	Clean, dry, non-corrosive gas			Clean, dry, non-corrosive gas such as air	Clean, dry, non-corrosive gas such as air		Clean, dry, non-corrosive gas such as air
Absolute Pressure Ranges[8]	Lowest Pressure	0 to 25 psia FS	0 to 25 psia FS	0 to 25 psia FS			Barometric 800-1100 mB 0 to 5 psia FS	0 to 5 (or ±25) psia FS
	Highest Pressure	0 to 5,000 psia FS	0 to 5,000 psia FS	0 to 5,000 psia FS			1 to 100 psia FS	0 to 100 (or ±20) psia FS
Gage Pressure Ranges[8]	Lowest Pressure	0 to 25 psig FS	0 to 25 psig FS	0 to 15 psig FS 3 to 15 Pji	0 to 0.5 inch WC FS	0 to 0.1 inch WC FS	0 to 5 psig FS	
	Highest Pressure	0 to 10,000 psig FS	0 to 5,000 psig FS	0 to 10,000 psig FS	0 to 10 psig FS	0 to 25 inch WC FS	0 to 100 psig FS	
Differential Pressure Ranges[8]	Lowest Pressure	0 to 25 (or ±10) psid FS			0 to 0.5 (or ±0.25) inch WC FS	0 to 0.01 (or ±0.1 inch WC FS		
	Highest Pressure	0 to 10,000 (or ±1,500) psid FS			0 to 10 (or ±5) psid FS	0 to 25 (or ±15) inch WC FS		
Vacuum Range[8]	Highest Vacuum	0 to 14.7 psiv			0 to 10 psiv			
Maximum Line Pressure (For Differential Pressure)		1000 psig Max on reference port			250 psig	14 inch WC on reference port		200 psig
Pressure Port		¼" 18 NPT internal	¼" 18 NPT internal	¼" 18 NPT internal	¼" 27 NPT internal	¼" OD tube	¼" 27 NPT internal	¼" 27 NPT internal
Response to Pressure Changes[3] (milliseconds)		1 to 5 ms	1 to 5 ms	1 to 5 ms	2 to 5 ms	50 ms	50 ms	50 ms
Accuracy % FS[4]		0.11%	0.11%	0.11%	0.14%	1%	0.05%	0.04%
Temperature Effects[6] Zero Shift ± % FS 100°F Sensitivity Shift ± % FS 100°F 30°F to 150°F		0.4 Max 0.3 Max	2 Max 1.5 Max	280: 0.6 Max / 0.5 Max; 280E: 1 Max / 1.5 Max	1 Max 1 Max	2 Max 2 Max	0.1-1.2a (0.2 at Barom) 0.1 Max	0.2 Max 0.2 Max
Transducer Output[9]		0 to 5 VDC (0 to ±2.5 VDC)	0 to 5 VDC 0 to ±2.5 VDC	0 to 5 VDC	0 to 5 VDC 0 to ±2.5 VDC	0 to 5 VDC	0 to 5 VDC	0 to 5 VDC 0 to ±2.5 VDC
Transducer Excitation		22 to 30 VDC	18 to 30 VDC	15 to 32 VDC	22 to 30 VDC	12 to 24 VDC	22 to 30 VDC	22 to 30 VDC
Transducer Circuit[10]		4 wire	4 wire	3 wire	4 wire	3 wire	4 wire	4 wire

Notes:
1. Stainless Steel housing (optional)
2. See catalog sheet for detail
3. For typical application, incompressible fluid (except models 239, 261, 270, 271). Exact response time depends on pressure range and system characteristics.
4. Accuracy as RSS of non-linearity, hysteresis, repeatability (at constant temperature)
5. Thermal zero shift 50% higher for vacuum range units
6. Thermal effects listed for 24 V circuit (slightly higher for some options)
7. Over 40°F to 100°F ranges calibrated at 70°F
8. Special ranges are available at extra cost
9. Transmitters have 4 to 20 ma
10. Transmitters have a 2-wire circuit

Definitions:
FS = Full Scale
WC = Water Column

Gage Pressure: Pressure measured relative to ambient atmospheric pressure. Referred to as pounds per square inch (gauge) or psig.

Absolute Pressure: Pressure measured relative to high vacuum. Referred to as pounds per square inch (absolute) or psia.

Vacuum Pressure: Pressure measured relative to ambient atmospheric pressure. Referred to as pounds per square inch (vacuum) or psiv.

Specifications subject to change without notice.

Price Range: $250 to $700 (Basic Transducer)

Figure 7.7: Example Specifications for High Accuracy Pressure and Vacuum Transducers
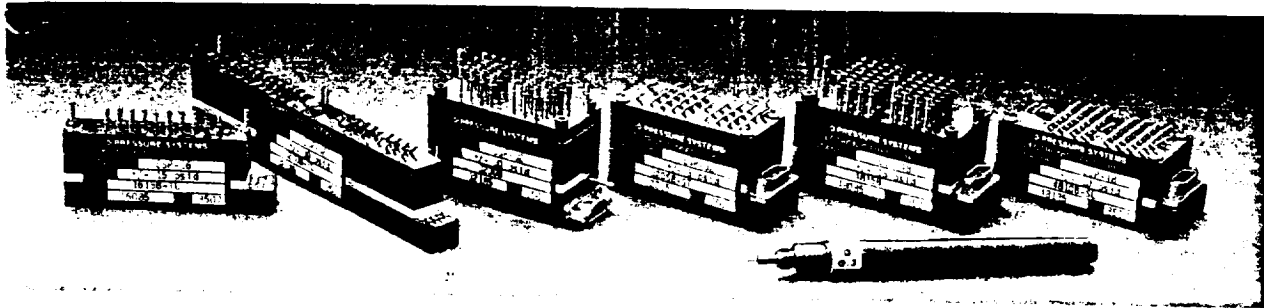
Miniature ESP Scanners

PRESSURE SCANNERS

Pressure System's line of pressure scanners are transducer per port electronically scanned instruments designed for multiple pressure measurement applications where high data rates and accuracy are paramount. These pressure scanners incorporate silicon pressure transducers, internal multiplexing and amplification with an integral calibration valve. They are designed to accurately measure pressures of dry, non-corrosive gaseous media. Several configurations are available, all fully compatible with the 780B Pressure Measurement System.

MINIATURE

The ESP Pressure Scanner line is designed to offer miniature high transducer density modules which satisfy applications where space is critical as in wind tunnel model testing. All ESP scanners interface to the 780B Data Acquisition and Control Unit using the Scanner Interface Modules.

RACKMOUNT

The S1600, S1600D and S3200 Pressure Scanners are rack mounted instruments for use in test stand applications where pneumatics can be brought to a central location. These scanners feature complete field repairability down to the transducer level and include front panel quick disconnects of all input pressures. Electrical interface to the DACU is provided by the Scanner Interface Racks where all pneumatic and electrical connections to the pressure scanners are automatically made once secured in the rack.
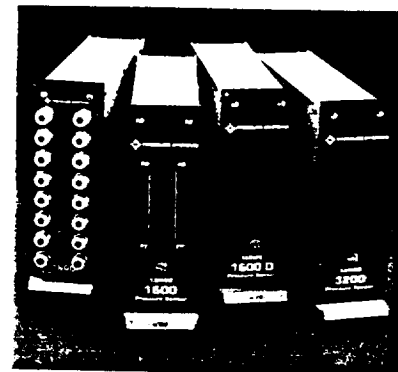
Rackmount Scanners

ESP Scanners	ESP-16TL	ESP-32TL	ESP-32	ESP-32SL	ESP-48	ESP-48SL	
INPUTS	16	32	32	32	48	48	CHANNELS
RANGE	±1-100	±1-100	±1-100	±1-100	±1-100	±1-100	PSID
STATIC ERROR	±0.10	±0.10	±0.10	±0.10	±0.10	±0.10	%F.S.
SCAN RATE	20,000	20,000	20,000	20,000	20,000	20,000	READINGS/SEC
TRANSDUCER DENSITY	7.6	7.6	7.1	8.9	10.7	13.4	TRANSDUCER/IN³

Rack Scanners	S1600	S1600-D	S3200	
INPUTS	16	16*	32	CHANNELS
RANGE	±10"	±10"	±10"	WC
	500	100	250	PSID
STATIC ERROR	±0.10	±0.10	±0.10	%F.S.
SCAN RATE	20,000	20,000	20,000	READING/SEC
FIELD REPAIRABLE	YES	YES	YES	
DENSITY PER 19" RACK	96	96	192	CHANNELS

*S1600-D are True Differential

Price Range: $150 to $200 per channel (Basic Transducer)

Figure 7.9: Example Specifications for High Accuracy Miniature Pressure Scanners

64 Series HEAT FLUX TRANSDUCERS

DESCRIPTION

MEDTHERM 64 Series Heat Flux Transducers offer dependable direct measurement of heat transfer rates in a variety of applications due to careful design, rugged quality construction and versatile mounting configuration. Each transducer will provide a self-generated 10 millivolt output at the design heat flux level. Continuous readings from zero to 150% design heat flux are made with infinite resolution. The transducer output is directly proportional to the net heat transfer rate absorbed by the sensor. Each transducer is provided with a certified calibration traceable through temperature standards to the National Bureau of Standards. These transducers have been proven in thousands of applications in aerospace applications, heat transfer research, and boiler design.

FEATURES

* LINEAR OUTPUT
* OUTPUT PROPORTIONAL TO HEAT TRANSFER RATE
* ACCURATE, RUGGED, RELIABLE
* CONVENIENT MOUNTING
* UNCOOLED, WATER COOLED, GAS PURGED MODELS
* RADIOMETER AND LIMITED VIEW ACCESSORIES
* MEASURE TOTAL HEAT FLUX
* MEASURE RADIANT HEAT FLUX
* REMOTE MEASUREMENT OF SURFACE TEMPERATURE

CONSTRUCTION FEATURES

ACCURACY, RUGGEDNESS AND RELIABILITY are provided by the thoroughly proven Gardon and Schmidt-Boelter sensors.

LONG TRANSDUCER LIFE AND SIGNAL STABILITY are enhanced by the massive body of pure copper, gold plated to protect against corrosion, contamination, and excess radiant heat absorption by the heat sink.

PROTECTION AGAINST ROUGH HANDLING in mounting is provided by a stainless steel flange when specified.

SIGNAL INTEGRITY is protected by the use of welded connections, stranded lead wire with braided copper shielding and teflon insulation firmly secured in the transducer body with strain relief to ensure resistance to rough handling and stray signals.

ACCESSORIES

REMOVABLE SAPPHIRE WINDOW ATTACHMENTS are available to limit the basic transducer to measurement of radiation heat flux only.

VIEW RESTRICTOR ATTACHMENTS are available to limit the angle of view for the basic transducer to 60°, 30°, 15°, or 7° for narrow view angle measurements.

DIRECT READING HEAT FLUX METER Model H-200 is available for direct meter readout in any heat flux units from any linear heat flux transducer input. A 0-1 volt recorder output is also provided. Ask for Bulletin 700.

BODY TEMPERATURE THERMOCOUPLE measurement is provided by an optional copper constantan 30 AWG solid conductor thermocouple, TIG welded junction, with fiberglass insulation and metallic overbraid.

OPERATING PRINCIPLES

The 64 Series transducers are of two basic sensor types, the Gardon type (5 to 4000 BTU/ft^2-sec) and the Schmidt-Boelter thermopile type (0.2 to 5 BTU/ft^{2}sec). In both type sensors heat flux is absorbed at the sensor surface and is transferred to an integral heat sink which remains at a temperature below that of the sensor surface. The difference in temperature between two points along the path of the heat flow from the sensor to the sink is proportional to the heat being transferred, and, therefore proportional to the heat flux being absorbed. At two such points, MEDTHERM transducers have thermocouple junctions which form a differential thermoelectric circuit providing a self-generated emf between the two output leads directly proportional to the heat transfer rate. No reference junction is needed.

Gardon Gauges absorb heat in a thin metallic circular foil and transfer the heat radially (parallel to the absorbing surface) to the heat sink attached at the periphery of the foil; the difference in temperature is taken between the center and edge of the foil.

Schmidt-Boelter gauges absorb the heat at one surface and transfer the heat in a direction normal to the absorbing surface; the difference in temperature is taken between the surface and a plane beneath the surface.

OPTIONAL FEATURES include four mounting configurations, water cooling provisions, gas purge provisions, or thermocouples for body temperature measurement. Water cooling should be specified if the uncooled transducer is expected to reach above 400°F.

The gas purging provision should be included on radiation transducers to be used in a sooty environment. The MEDTHERM purge is designed to pass rigid NASA performance tests with fuel-rich oxy-acetylene flames directed toward the window at close range.

STANDARD CONFIGURATIONS

The basic transducer may be selected with either of four mounting configurations and with or without provisions for water cooling of transducer body. It may also be provided with gaseous purging to keep the radiation-transmitting window clean, but when the purging provision is included, the window is installed and is not an accessory.
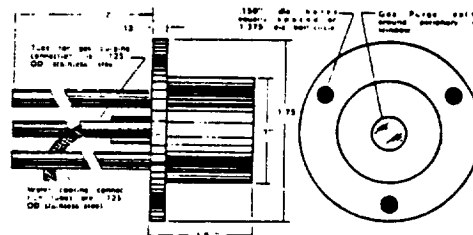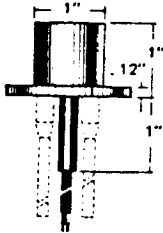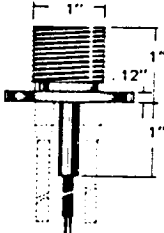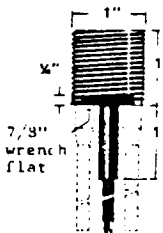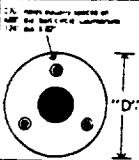
RADIOMETER WITH GAS PURGING PROVISIONS

Figure 7.10: Example Specifications for Rapid Response Heat Flux Transducers
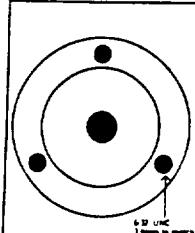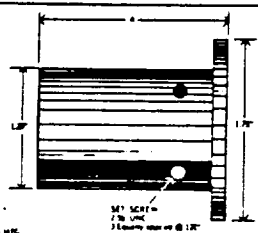
The four available mounting configurations are illustrated below. There is the smooth body with flange, the threaded body with flange, the smooth body without flange, and the threaded body without flange. All mounting flanges are 1.75" dia. with .150" dia. mounting holes equally spaced on a 1.38" dia. bolt circle. Water cooling tubes (when specified) are .1/8" dia. stainless steel and gas purge tubes are 1/8" dia. stainless steel. All tubes are 2" long. The threaded transducer bodies are 1-12 UNF-2A threads.

SMOOTH BODY WITH FLANGE		THREADED BODY WITH FLANGE		SMOOTH BODY, NO FLANGE		THREADED BODY, NO FLANGE	
VERSION	MODEL NO.	VERSION	MODEL NO.	VERSION	MODEL NO.	VERSION	MODEL NO.
BASIC, NO COOLING	64-xx-16	BASIC, NO COOLING	64-xx-17	BASIC, NO COOLING	64-xx-14	BASIC, NO COOLING	64-xx-15
WATER COOLED	64-xx-20	WATER COOLED	64-xx-21	WATER COOLED	64-xx-18	WATER COOLED	64-xx-19
RADIATION, PURGED COOLED	64P-xx-24	RADIATION, PURGED COOLED	64TP-xx-25	RADIATION, PURGED COOLED	64P-xx-22	RADIATION, PURGED COOLED	64TP-xx-23

SAPPHIRE WINDOW ATTACHMENT may be added for elimination of convective heat transfer, thus making the transducer a radiometer or radiation heat flux transducer. Three view angles are available: 90°, 120°, and 150°. Windows are removable and replaceable by user. When the window is used the sensitivity of the basic transducer is reduced to a nominal fraction of the original as follows: 90°, 43%; 120°, 64%. 150°, 79%. Thickness of the attachment varies with view angle and sensor type from 1/16" to 3/8".

BODY STYLE "D"		CALIB?	MODEL
SMOOTH	1.0	NO	SW-1-YY
THREADED	.84	NO	SW-2-YY
SMOOTH	1.0	YES	SW-1C-YY
THREADED	.84	YES	SW-2C-YY

VIEW RESTRICTOR ATTACHMENTS for limiting the area view or seen by the sensor are sometimes desired for making radiation or remote temperature measurements.

VIEW ANGLE	"A"	NOMINAL % BASIC SENSITIVITY	MODEL NO.
7°	3.9"	.4%	VR-7
15	2.3	1.7	VR-15
30	1.6	6.6	VR-30
60	1.2	25.0	VR-60

SPECIFICATIONS

RANGES AVAILABLE: 4000, 3000, 2000, 1000, 500, 200, 100, 50, 20, 10, 5, 2, 1, 0.2 BTU/ft^2-sec. design heat flux level.

OUTPUT SIGNAL: 10 millivolts $\pm$ 1.5 millivolts at full range.

MAXIMUM ALLOWABLE OPERATING BODY TEMPERATURE: 400°F.

OVERRANGE CAPABILITY: 150% for 5-2000 BTU/ft^2-sec. ranges; 500% for 0.2-2 BTU/ft^2 sec ranges.

MAXIMUM NON-LINEARITY: $\pm$2% of full range

REPEATABILITY: $\pm$1/2%

ACCURACY: $\pm$3% for most ranges

CALIBRATION: Certified calibration provided with each transducer.

SENSOR ABSORPTANCE: 92%, nominal, from 0.6 to 15.0 microns.

SPECTRUM TRANSMITTED BY SAPPHIRE WINDOW (When used): 85% nominal from 0.15 to 5.0 microns.

LEAD WIRE: 24 AWG stranded copper, two conductor, teflon insulation over each, metallic overbraid, teflon overall, 36" long, stripped ends.

RESPONSE TIME (63.2%):
500 to 4000 BTU/ft^{2}sec: less than 50 msec.
50 to 200 BTU/ft^{2}sec: less than 100 msec.
5 to 20 BTU/ft^{2}sec: less than 290 msec.
0.2 to 2 BTU/ft^{2}sec: less than 1500 msec.

SENSOR TYPE
5 to 4000 BTU/ft^{2}sec: Gardon Gauge
0.2 to 4 BTU/ft^{2}sec: Schmidt-Boelter

NOMINAL IMPEDANCE
Less than 10 ohms on Gardon Gauges
Less than 100 ohms on Schmidt-Boelter Gauges.

Amount of heat which can be absorbed by transducer in an adiabatic (perfectly insulated thermally) installation before exceeding the 400°F limitation
Models without water cooling provisions: 6.2 BTU
Models with water cooling provision but without water in passages: 4.2 BTU.
Maximum gas pressure for gas purged models: 150 psig.

Figure 7.10: **Example Specifications for Rapid Response Heat Flux Transducers (Concluded)**

References

[1] Evans, R., "Boundary Layer Integral Matrix Procedure, BLIMP-J User's Manual," Aerotherm Division/Acurex Corporation, under Contract NAS8-30930, July 1975.

[2] Nickerson, G. R., Dang, L. D., and Coats, D. E., "Two-Dimensional Kinetic Reference Computer Program - TDK," Engineering and Programming Manual, Software and Engineering Associates, Inc., Carson City, Nevada, under Contract NAS8-35931, April 1985.

[3] Praharaj, S. C. et al., "Boundary Layer Simulator Improvement," REMTECH Report RTR 115-1, Huntsville, AL, Dec. 1984.

[4] Praharaj, S. C., "Boundary Layer Simulator (BLIMPJ) Improvement," Paper presented at 22nd JANNAF Combustion Meeting, JPL, California, Oct. 7-10, 1985.

[5] Dirling, Jr., R. B., "A Method for Computing Roughwall Heat Transfer Rates in Reentry Nosetips," AIAA Paper No. 73-763, July 1973.

[6] Reshotko, Meyer et al., "Heat Transfer in a 60° Half-angle of Convergence Nozzle with Various Degrees of Roughness," NASA-TN-D-5887, July 1970.

[7] Cebeci, T. and Chang, K. C., "Calculation of Incompressible Rough-Wall Boundary Layer Flows," *AIAA Journal*, Vol. 16, No. 7, July 1978, pp. 730-735.

[8] Eberle, E. E., "Thermal Analysis of the Data from the 40K Subscale Regeneratively Cooled Thrust Chamber Cyclic Life Tests," Rockwell International Internal Letter ASR 76-206 (SSME 76-2523), Sept. 1976.

[9] Launder, B. E., "Laminarization of the Turbulent Boundary Layer by Acceleration," MIT Gas Turbine Lab., Report No. 71, 1963.

[10] Patel, V. C. and Head, M. R., "Reversion of Turbulent to Laminar Flow," *J. of Fluid Mechanics*, Vol. 34, Part 2, 1968, pp. 371-392.

[11] Back, L. H, Cuffel, R. F. and Massier, P. F., "Laminarization of Turbulent Boundary Layer in Nozzle Flow – Boundary Layer and Heat Transfer Measurements with Wall Cooling," ASME Paper 69-HT-56, Aug. 1969.

[12] Nash-Webber, J. L., "Wall Shear-Stress and Laminarization in Accelerated Turbulent Compressible Boundary Layers," MIT Gas Turbine Lab. Report No. 94, Apr. 1968.

[13] Hodge, B. K. and Adams, J. C., "The Calculation of Compressible Transitional, Turbulent, and Relaminarizational Boundary Layers Over Smooth and Rough Surfaces Using an Extended Mixing-Length Hypothesis," AEDC-TR-77-96, Feb. 1978.

[14] Coleman, H. W., Moffat, R. J. and Kays, W. M., "The Accelerated Fully Rough Turbulent Boundary Layer," *J. of Fluid Mechanics*, Vol. 82, Part 3, 1977, pp. 507-528.

[15] Huffman, G. D., Zimmerman, D. R., and Bennet, W. A., "The Effect of Freestream Turbulence Level on Turbulent Boundary Layer Behavior," AGARD AG164, Apr. 1972, pp. 91-115.

[16] Charnay, G., Compte-Bellot, G. and Mathieu, J., "Development of a Turbulent Boundary Layer on a Flat Plate in an External Turbulent Flow," AGARD CP93, Paper No. 27, 1971.

[17] McDonald, H. and Kreskovsky, J. P., "Effect of Free-Stream Turbulence on the Turbulent Boundary Layer," *International J. of Heat and Mass Transfer*, Vol. 17, 1974, pp. 705-716.

[18] Rued, K. and Wittig, S., "Free-Stream Turbulence and Pressure Gradient Effects on Heat Transfer and Boundary Layer Development on Highly Cooled Surfaces," *J. of Engineering for Gas Turbines and Power Transactions of the ASME*, Vol. 107, Jan. 1985, pp. 54-59.

[19] Tien, C. L., "Heat Transfer by a Turbulently Flowing Fluids - Solids Mixture in a Pipe," Transactions of the ASME, *J. of Heat Transfer*, May 1961, pp. 183-188.

[20] Soo, S. L. and Tien, C. L., "Effect of the Wall on Two-Phase Turbulent Motion," *J. of Applied Mechanics*, Transactions of the ASME, March 1960, pp. 5-15.

[21] Farbar, L. and Morley, J. J., "Heat Transfer to Flowing Gas - Solids Mixtures in a Circular Tube," *Industrial and Engineering Chemistry*, Vol. 49, No. 7, July 1957, pp. 1143-1150.

[22] Soo, S. L., *Fluid Dynamics of Multiphase Systems*, Blaisdell Publishing Co., 1967, pp. 10-85.

[23] Smith, Sheldon D., "High Altitude Chemically Reacting Gas-Particle Mixture, Vol. 1 – A Theoretical Analysis and Development of Numerical Solution," LMSC-HREC TRD867400-1, Aug. 1984.

[24] NWP Code – Written for the VAX and available at REMTECH, Inc., Huntsville, AL.

[25] Rao, G. V. R., "Exhaust Nozzle Contours for Optimum Thrust," *Jet Propulsion*, Vol. 28, No. 6, June 1958, pp. 377-382.

[26] Praharaj, S. C. and Palko, R. L., "Measurements for Liquid Rocket Engine Performance Code Verification," REMTECH Technical Report RTR 157-01, Huntsville, AL, Oct. 1986.

[27] Pavli, A. J., et al., "Experimental Thrust Performance of a High-Area-Ratio Rocket Nozzle," NASA Technical Paper 2720, April 1987.

[28] Nouri, J. A., "Two-Dimensional Laser Doppler Velocimeter Studies of Subsonic Jet Impinging on a Flat Plate," M.S. Thesis, Department of Aerospace and Mechanical Engineering, University of Tennessee Space Institute, Tullahoma, TN, 1982.

[29] Nouri, J. A., "Three-Dimensional Laser Doppler Velocimeter Studies of Flow in a 90° Curved Duct with Square Cross Section," Ph.D. Dissertation, Department of Aerospace and Mechanical Engineering, University of Tennessee Space Institute, Tullahoma, TN, 1987.

[30] Durst, F., Melling, A., and Whitelaw, J. H., *Principles and Practices of Laser Doppler Anemometry*, Academic Press, 1976.

APPENDIX

SUMMARY OF MODIFICATIONS TO THE TURBULENCE MODELS AND ADDITIONS OF ENGINEERING MODELS IN BLIMPJ

WALL SURFACE ROUGHNESS EFFECTS

The Cebeci-Smith turbulence model given in Ref. [1] was modified in Ref. [3] using the formulation of Cebeci and Chang in Ref. [7] to include the effects of wall surface roughness. The expression for mixing length given by

$$\ell = 0.4 \, y \left\{ 1 - \exp\left(-y/A\right) \right\}$$

is modified and rewritten as

$$\ell = 0.4 \, (y + \Delta y) \left[1 - \exp\left\{ -\left(y + \Delta y \right)/A \right\} \right]$$

where the coordinates are displaced by an amount Δy. Δy is expressed as a function of an equivalent sand-grain roughness parameter $K_s^+ \, (\equiv K_s \, U_\tau / \nu)$, i.e.,

$$\Delta y = 0.9 \, (\nu / U_\tau) \left\{ \sqrt{K_s^+} - K_s^+ \exp\left(-K_s^+ / 6 \right) \right\}$$

This expression is valid for $4.533 < K_s^+ < 2000$, with the lower limit corresponding to the upper bound for a hydraulically smooth surface.

This report considered multiple smooth/rough surfaces, where, for smooth surfaces, K_s was set to zero and, for rough surfaces, K_s was set equal to the appropriate values.

Reference [3] also included the following engineering options to calculate skin friction and Stanton Number for rough surfaces.

Skin friction compressibility (Young)

$$\frac{C_f}{C_{fi}} = 0.365 \left(\frac{H_e}{H_{aw}} \right) + 0.635 \left(\frac{H_e}{H_w} \right)$$

Incompressible rough wall skin friction

<u>Option (1) Prandtl-Schlichting</u>

$$C_{fi} = [\, 2.87 + 1.58 \log_{10} (x/k) \,]^{-2.5}$$

<u>Option (2) Droblenkov</u>

$$C_{fi} = 0.0139 \, (x/k)^{-1/7}$$

<u>Rough surface turbulent Stanton Number (Seidman)</u>

$$St = \frac{C_f}{2} \left[1 + A \left(\frac{C_f}{2} \right)^{0.725} (Re_k)^{0.45} (Pr)^{0.8} \right]^{-1}$$

where A = 0.52 nominal and range from 0.45 to 0.7 (Owen & Thompson), and C_f is obtained from the first equation given.

<u>Transition Criterion (Fenter)</u>

$$\eta_k \;=\; \frac{\rho_w U_\tau k}{\mu_w} \text{ where } U_\tau = U_e \sqrt{\frac{C_f}{2} \frac{\rho_e}{\rho_w}}$$

$$\eta_k \;\leq\; 5, \text{ Smooth}$$

$$5 \;\leq\; \eta_k \leq 100, \text{ Transitionally rough}$$

$$100 \;\leq\; \eta_k, \text{ Rough}$$

RELAMINARIZATION EFFECTS

Eddy viscosity, ϵ_m, in any of the three algebraic eddy viscosity models in Ref. [1] and this report is varied with acceleration parameter, K, from a turbulent ϵ_m (ref) value to a value of zero for completely laminar flow according to

$$\epsilon_m = \left\{ 1 - \left(\frac{K - K_1}{K_2 - K_1} \right) \right\} \cdot \epsilon_m \,(\text{ref})$$

where K is given by

$$K = \frac{\overline{\mu}_w}{\overline{\rho}_w U_e^2} \cdot \frac{dU_e}{dx} \, ,$$

the lower limit, K_1, is given by

$$K_1 = aR^2 + bR + c$$

where
$$\begin{aligned} a &= 8.935 \times 10^{-14} \\ b &= 2.239 \times 10^{-10} \end{aligned}$$

with c given by

$$
\begin{aligned}
c \quad &= \quad 0.27 \times 10^{-6}, \, K_r \le 0.8 \times 10^{-4} \\
&= \quad -0.27 \times 10^{-6} + 0.676 \times 10^{-2} \, K_r, \\
& \qquad\qquad 0.8 \times 10^{-4} < K_r < 4.1 \times 10^{-4} \\
&= \quad 2.5 \times 10^{-6}, \, K_r \ge 4.1 \times 10^{-4}
\end{aligned}
$$

where
$$K_r = \frac{K_a}{U_e} \cdot \frac{dU_e}{dx}$$

and the upper limit, K_2, is given by

$$
\begin{aligned}
K_2 \quad &= \quad 0.7 \times 10^{-6}, \, K_r \le 0.8 \times 10^{-4} \\
&= \quad -0.245 \times 10^{-6} + 1.182 \times 10^{-2} \, K_r, \\
& \qquad\qquad 0.8 \times 10^{-4} < K_r < 4.1 \times 10^{-4} \\
&= \quad 4.6 \times 10^{-6}, \, K_r \ge 4.1 \times 10^{-4}
\end{aligned}
$$

EFFECTS OF CONDENSED PHASE

The ratio of particle diffusivity to eddy diffusivity is given by

$$\frac{D_p}{D_f} = 1 - \frac{\lambda_L^2}{\lambda_E^2} \left(\frac{3I^2}{I+2} \right) + O\left(\frac{1}{\lambda_E^4} \right)$$

where $\qquad I \;=\; (\sqrt{\pi}\,/\,18) < N_{Re} > \left(\rho_p\,/\,\rho_f\right)\left(2r_p\,/\,\lambda_L\right)$

with $\quad < N_{Re} > \;=\; \left(2r_p\,/\,\nu\right) < u'^2 >^{1/2}\;,$

$$\lambda_L \;=\; \frac{D_f}{<u'^2>^{1/2}}$$

and $\qquad \lambda_E \;=\; \delta\;(\equiv \text{ local boundary layer thickness})$

The eddy diffusivity, $D_f\;(\equiv\; \epsilon_D)$, is calculated in BLIMPJ.

Assuming the turbulent Schmidt Number to be constant between clean flow and flow with particles,

$$Sc = \left(\frac{\epsilon}{\epsilon_D}\right)_p = \frac{\epsilon}{\epsilon_D}$$

from which the eddy viscosity, ϵ_p, for the particulate flow is obtained as

$$\frac{\epsilon_p}{\epsilon} \;=\; \frac{\epsilon_{D_p}}{\epsilon_D}$$

Reference [3] also included the following engineering options to calculate skin friction and wall heat transfer rate for particulate flow.

Laminar Boundary Layer (Marble)

$$C_f \;=\; C_{fo}\sqrt{1+K}\,\left(1 + 0.49\,\frac{K\,\lambda_v\,/\,x}{1+K}\right)\,,\quad \frac{\lambda_v}{x} \ll 1$$

and $\quad \dot{q} \;=\; \dot{q}_o\,\sqrt{1+K}\,\left(1 + 0.49\,\frac{K\,\lambda_v\,/\,x}{1+K}\right)\,,\quad \frac{\lambda_v}{x} \ll 1$

where $\quad K \;=\; \rho_p/\rho_e$

$$\lambda_v \;=\; \frac{mU_e}{6\,\pi\,a\,\mu_e}$$

Turbulent Boundary Layer

For $\quad \dfrac{W_p}{W_f} \;<\; 1$ (Tien)

$$C_f \;=\; C_{fo}\,(1 + \beta_5)$$

and $\quad \dot{q} \;=\; \dot{q}_o\,(1 + \beta_5)$

where $\quad \beta_5 \;=\; \dfrac{C_p\,W_p}{C_f\,W_f}$

For $\quad \dfrac{W_p}{W_f} \;>\; 1$ (Farbar and Morley)

$$Nu \;=\; 0.14\,Re_D{}^{0.6} \;\cdot\; \left(W_p / W_f\right)^{0.45}$$

But, $\quad Nu_o \;=\; 0.023\,(Re_D)^{0.8} \;\cdot\; Pr^{0.4}$

$$\dot{q} \;=\; \left(\dfrac{Nu}{Nu_o}\right) \;\cdot\; \dot{q}_o$$

Particle Factor $\;=\; Nu/Nu_o$

$$C_f \;=\; \dfrac{Nu}{Nu_o} \;\cdot\; C_{fo}$$